POLITECNICO DI TORINO

Master degree course in Mechanical Engineering

Master Degree Thesis

The comparison of numerical methods for the calculation of thermo-elastic deformations of satellite structures

The comparison of temperature transfer methods from thermal to structural models and the evaluation of automated procedures to compute thermo-elastic deformations

Supervisors:
Prof. Erasmo Carrera
Dr. Matteo Filippi

Candidate:
Michele Delicata

Internship Tutor:
Thales Alenia Space France
Jurij D'Amico

Academic Year 2018 – 2019

Summary

In the last three decades, space missions have required increasing needs in terms of strength, stability and performances of satellite structures. This context has led the national space agencies, and in general the whole industrial sector, to invest more resources also in the thermo-elastic verification of spacecrafts. This field is characterised by multiple critical issues in the numerical prediction phase of stresses and deformations due to thermal loads, both on-ground and in-obit. These problems reside in the diversity presented by the mathematical models used for thermal and structural analysis; the discrepancy is due to the different simulation environments, to the different type of continuum mechanics problem discretization, to the hypotheses of the numerical simulation method. For example, in thermal analysis a physical representation prevails with concentrated parameters while in the structural validation finite element methods are used; this causes a considerable difference in the level of mesh detail, between the two simulation environments.

This thesis analyses issues such as: temperature transfer from the thermal model to the structural model, the influence on the results of the variation of some interpolation parameters of the algorithm based on the inverse weighting of the distance, the computational time of the procedures to obtain deformations and stresses , the evaluation of multidisciplinary codes able to support every phase of the design. To this end, in addition to the canonical simulation and modelling software such as MSC Nastran, MSC Patran, ESATAN-TMS, the MaREA code, developed by Thales Alenia Space Italy, has been widely used.

The first study adopts the version of the IDW algorithm implemented in MaREA, for the transfer of temperatures; therefore, for some load cases, deformations are calculated by varying: the IDW numerical parameters, the set of recovery structural nodes, the thermal nodal breakdown and the type of thermal loads. The aim is to assess the influence of the latter input on the temperature mapping process. In general, although there is a sensitivity of temperature mapping w.r.t. the k and N variation, the overall influence on deformations is negligible. This observation may support the idea that further improvements of a pure spatial interpolation approach, like the IDW, could help to have a slightly better mapping on the structural model, remaining however ineffective in producing very different thermo-elastic results. On

the contrary, the results show an important variation in terms of deformations when a coarse thermal model is adopted; the alteration can reach 70 µm or exceed 100 µrad, for some nodes, and in most cases this discrepancy is greater than 20 units. This study was applied to the service module of the Euclid program, so this choice could be a limit to the generality of the results obtained, being a very stable and rigid structure; however, the latter is representative of a real case and it is where some extremely important devices are mounted, such as the star tracker.

The second study focuses on a typical procedure for the pointing stability analysis of satellite structures. This approach returns a matrix containing local mechanical deformations and performance contributions on the structural model, applying unitary thermal loads. The translations and rotations are obtained multiplying this local information by a matrix containing all the temperature vectors belonging to the transient thermal analysis. This method allows to easily analyse many cases but requires considerable effort for the construction of the influence matrix. Therefore, the main objectives are: to apply the TEMASE-MaREA algorithm to build the influence matrix, to test the overall potential of MaREA in terms of time saving and level of iterations automation. The results are compared with an approach that adopts a low level of automation. Considering all the difficulties encountered, the TEMASE approach is capable of reducing more than half of the working time, bringing it, in the current case, to a week.

Acknowledgements

I would like to thank Professor Erasmo Carrera for entrusting me with this thesis work.

I would like to express my very great appreciation to Vincenzo Mareschi for his valuable support and guidance, during each phase of the present study.

I would like to thank Tiziano Malosti, Pietro Nali, Savino De Palo and Mathieu De Cillia for their important advices and inputs. Thanks also to Antoine Carlino and to my friend and colleague Ismaïl for helping me to use some numerical simulation software.

Special thanks are also addressed to Jean François and his family, for their precious friendship.

I express my appreciation to my friends Malte, Constance and Valentina for their advice and encouragement; thanks also to Gianni Blasi for his review of my final draft.

Many thanks to all my mates who, in these years of university, have demonstrated me a genuine friendship and brotherhood; in particular Giuseppe, Euter, Sushil and my godfather Simone.

I want to thank my family, especially my parents, Mauro and Rosalia, and my sisters, Alessia and Mariachiara, for their invaluable support and love.

Finally, I thank all those who spiritually and morally guided me and those who have prayed for me. All praise, honour and glory to my Lord Jesus Christ for His richest grace, blessing, wisdom, strength, guidance and willpower, for the accomplishment of these years of study.

Acronyms

ADPM Antenna Deployment & Positioning Mechanism

CDMU Central Data Management Unit

CTE Coefficient of Thermal Expansion

FEM Finite Element Model

GMM Geometric Math Model

ID Identification number

IDW Inverse Distance Weighting

IM Influence Matrix

LOS Line-Of-Sight

MaREA Multidisciplinary ReEntry Analysis

MLI Multi-Layer Insulation

MPC Multiple-Point Constraints

NRMSE Normalised Root-Mean-Square Error

PCDU Power Control Data Unit

STR Star Tracker

TEMASE Temperature Mapping Sensitivity

TLP Thermal Lumped Parameter

TM Thermal load Matrix

TMM Thermal Mathematical Model

TN Thermal Node

Contents

List of Tables

List of Figures

Introduction

The present study started during an extra curricular internship, held at Thales Alenia Space France, and it was further developed in collaboration with the department of mechanical and aerospace engineering at the *Politecnico of Torino*, under the guide of Dr. Carrera.

This thesis regards the study of some critical issues that are faced during the designing of satellite structures, regarding the thermo-elastic behaviour of the vehicle and its equipment. The knowledge of temperature distribution acting on a structure allows to evaluate the thermal expansion or contraction effects to which it is subjected and to determine the consequent stresses and deformations that are generated. An appropriate evaluation of these internal loads is essential to ensure the functionality and the safety of the structure, without endangering the objectives of the mission and degrading the spacecraft performances. Thus, the structures must ensure strength, rigidity and stability during on-ground and in-obit phases, in order to preserve their characteristics under the combined action of mechanical loads, temperature variation, humidity, vacuum, irradiation and chemical environment. To this end, the satellites design includes also thermo-elastic analysis. In this regard, some operational problems concern the need to: consider the adequacy of structural and thermal mathematical models for thermo-elastic purpose, obtain a suitable characterisation of temperatures on the structural model, consistently with the data coming from the thermal analysis, and transfer information between different numerical modelling environments.

In fact, the two mathematical models, used to perform the thermal and structural verification, diverge because of the different detail level of the discretization of the continuum mechanics problem and for the discrepancy in the simulation method assumptions. For example, the thermal analysis is usually dominated by lumped parameters methods and the mechanical analysis is characterised by the finite element method. Therefore, the main objectives can be summarised as follows:

1. to analyse the temperature data exchange between thermal mathematical models and structural finite element models, in order to investigate the critical issues related to thermal-elastic analysis;

2. to evaluate a common used spatial interpolation approach w.r.t. the influence on thermo-elastic distortions of some input parameters variation;
3. to test the potential of the multidisciplinary software MaREA in terms of time saving and level of procedures automation;
4. to apply an automated procedure to build a sensitivity matrix of a representative satellite structure.

The aforementioned investigations were assayed using some case studies inherited by the Euclid program and the Iridium Next program.

Chapter 1 describes several critical issues about the thermo-elastic analysis and the transferring of temperatures between mathematical models. Furthermore, the main procedures to perform temperature mapping are presented and the inverse distance weighting (IDW) algorithm, used in the present study, is well exposed. Therefore, point 1 of the previous list is covered.

In chapter 2 a case-study approach is adopted to evaluate the MaREA code and to study the thermo-elastic displacements using the chosen interpolation function and varying: the IDW numerical parameters, the set of recovery structural nodes, the thermal nodal breakdown and the type of thermal loads. The aim is to assess the influence of the latter input on the temperature mapping process, in order to achieve some useful hints for the thermo-elastic design process. Thus, points 2 and 3 of the above list are analysed.

Lastly, chapter 3 shows a widespread procedure for pointing stability analysis of satellite structures. This method consists in the construction of an influence or sensitivity matrix that contains local mechanical deformations and performance contributions on the FEM, applying unitary thermal loads of 1 °C. The latter information is multiplied by a matrix containing all the temperature vectors belonging to the transient thermal analysis of the spacecraft; so, according to the linearity hypothesis, a matrix with the actual structural deformations is obtained. Chapter 4 includes the conclusions concerning these studies conducted on the Euclid and Iridium Next program.

Chapter 1

Methodology of the analysis of the thermo-elastic effects during a satellite mission

In the last three decades, the stability needs, both for science and Earth observation missions, have increased considerably, for example to reach high spatial resolution [1, 2], which regards the pointing stability and accuracy. Dimensional stability may be defined as the tendency of highly accurate structures to preserve their dimensions under the action of adverse conditions like mechanical loads, temperature, humidity, vacuum, irradiation and chemical environment [1]. This requirements framework set extremely limited structural dimensional changes, in order to reach accuracy of some micrometres and absolute pointing errors of micro-radians; different space missions could be mentioned in this regard, as for example PLATO, LISA, Herschel, GRACE, GOCE [2, 3]. The main issues affecting the dimensional stability of satellite structures may be summarised as follows [1]:

- thermo-elastic effects;
- moisture release;
- 1g-0g environment transition;
- in-orbit loads;
- material ageing;
- material dimensional instability.

Therefore, both for telecommunication and observation satellites, the deformations and the stresses induced by thermal loads have to be well studied in order to reach the structural stability and strength requirements. So the design of the structure is oriented towards the reduction of distortions that could degrade mission performance, like in case of inadequate instrument pointing. The thermal controlling devices are geared towards the mentioned purposes. For example some payloads are arranged on heating or cooling ducts system, in order to exchange thermal power and to satisfy stringent temperature stability requirements.

A typical problem, to deal with during the numerical design, is the thermal load definition, given by the translation of thermal model temperature results to structural model temperature load input. This data exchange is often called temperature mapping. The main difficulty of this process rely on the discrepancy regarding the numerical methods adopted, during the design process [4, 5]:

- usually, spacecraft thermal analysis is dominated by the thermal lumped parameter (TLP) methods; as a result, the physical system is represented by a network of conductors and capacitance. The thermal mathematical model (TMM) and a set of temperature vectors and information are generated, in order to be used by the structural analysts.

- The spacecraft structural analysis is performed using the finite element method. Therefore, a finite element model (FEM) is created, to assess strength and dynamic behaviour of the structure.

In this chapter the principal aspects regarding the thermo-mechanical analysis and the main temperature mapping methods are introduced.

Remark 1 In the present study, the field of investigation concerns a conventional temperature range included between 120 and 420 K.

1.1 Thermal-elastic analysis and requirements

The satellite structural elements tend to contract or expand when they are subjected to a given temperature field different from the one where the same sample is considered stress free; the latter is the case of the typical production room temperature at 20 °C. As a result, an initial strain vector ϵ_0 occurs. These thermal effects, usually, cannot proceed freely, and the structure becomes stressed; so these internal loads are called thermal loads [6, 7]. For example, considering an isotropic material, the initial strain may be defined as:

$$\epsilon_0 = \alpha \Delta T, \tag{1.1}$$

where α is a linear coefficient of thermal expansion (CTE) and $\Delta T = T - T_0$ a temperature change with T_0 considered as thermal stress free condition. The consequent stresses may be an important issue for static strength validation of the structure w.r.t. the applicable thermal load cases. Nevertheless, the main focus of thermo-elastic distortion analyses is the study of deformations induced by thermal loads rather than the assessment of static strength [1].

The CTE is key parameter in the aforementioned analysis, setting the amount of deformations. In the present study, the FEM and the linear thermo-elastic analyses are performed using MSC Nastran; so, it is underlined that the CTE, as characteristic material property, is defined on Nastran MAT bulk data cards [8]. Once the properties and the loads are defined, a thermo-elastic model verification has to be done, as explained in section 11.2.1.2 of [1].

Lastly, the thermal-elastic validation may follow two main purposes, as briefly explained below [2].

- A sizing analyses is intended to verify the structure strength against thermal loads without failure or structural degradation. As a matter of fact, during the last phases of the launcher flight and while on orbit, space modules are stressed by huge temperature gradients on materials, often with different CTEs; for example in case of composite and metallic honeycomb panels and internal links.

- A pointing analyses is crucial in case of several space missions, as mentioned above. For example, the spacecraft absolute orientation is given by the star trackers (STR) that affects the line-of-sight (LOS) stability; therefore, thermo-elastic distortions cause payload-star tracker misalignment and LOS disturbances. In addition, telescopes, antennas and other units must guarantee a very precise orientation. These pointing errors can be reduced controlling the temperature of the satellite, using materials with low CTE and by avoiding to merge materials with CTEs highly different.

1.2 Temperature mapping methods on the structural model

The temperature field resulting by a thermal analysis, performed for example by ESATAN-TMS, is used as input for the thermo-elastic verification. Commonly, the TMM nodes and the FEM nodes differ for their space location in the geometric model, for the different detail level of the continuum mechanics problem discretization, which causes huge variation in the number of nodes between the two environments, and lastly for the discrepancy in the simulation method assumptions. Therefore, one problem to be solved is the temperature data transfer from a coarse thermal model to a finer structural model developed for strength or dynamic analyses [1, 4]. Figure 1.1 shows an example of this transferring. This kind of temperature

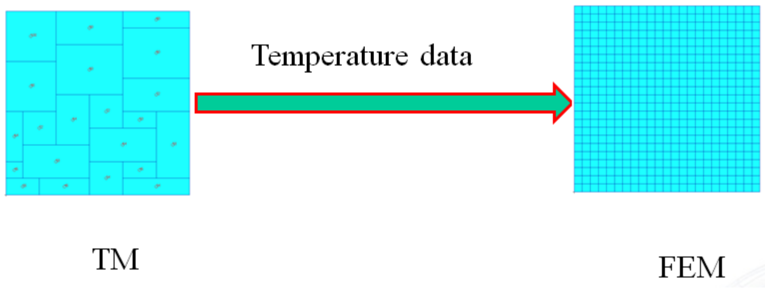

Figure 1.1. Example of temperature field transfer from TMM to FEM.

mapping is achieved by the help of dedicated software tools which are exposed or used in the present thesis activity. The data transfer process involves an interpolation of the thermal nodes known temperatures w.r.t. the entities of the structural finite element model; therefore, such procedure between different numerical modelling environments is not straightforward and unfettered, with high risk of human errors when some manual methods are adopted. The reliability of thermoelastic prediction is strongly affected by an appropriate characterisation of temperatures on the structural model, consistently w.r.t. the data coming from the thermal analysis. Consequently, the causal role of data exchange between the TMM and the FEM in the assessment of structural distortions and stresses, induced by the temperature loads, is a key aspect of the present study.

As introduced above, some thermo-elastic modelling aspects w.r.t. the structural and thermal one are summarised as follows [1]:

- The different mesh size between thermal and structural models is mainly attributed to the study of different phenomena which require different modelling goals. For example, the assessment of radiation, conductivity and dissipation are thermal analysts goals, while strength and dynamic behaviour are mechanical analysts objectives. As a consequence, these models are often not well suited for thermo-elastic analyses purpose, where high confidence in the results is required. To overcome these critical issues a conservative margin policy is nearly always necessary, to achieve thermo-elastic performances according to the requirements of the mission.

- The honeycomb panels are usually modelled with 2D plate elements, arranged in the middle of the thickness, instead of 3D elements. In this way, for example, a reduced mathematical representation heaviness is obtained, with a consequent easier handling of the model. This choice could be appropriate in several static and dynamic cases but, on the contrary, it could introduce important errors into the thermo-elastic predictions; suffice it to consider the case in which the internal matrix of the panel is composed of a different material than the surface.

- Considering equipment and payload units with the lowest eigenfrequency above 100 Hz, they are typically modelled by lumped mass models. In particular they are mass point connected by rigid elements to the unit mounting interfaces; this is the case of the electronic units explained in section 2.1.1. Therefore, it is crucial to overcome any fictitious and non-physical constraints resulting by an use of these elements, in case of thermo-elastic analysis purpose. For years, such constraints were commonly generated by the multiple-point constraints (MPC) [8], as in case of Nastran RBE2 elements, used, as said before, to model secondary structures. According to the last years enhancements, for these finite elements it is possible to define a CTE, avoiding the mentioned drawbacks when a non-zero length is applied to them. In any case, an effort to substitute the MPCs by alternative constituents or to set the thermo-elastic properties of the enhanced rigid elements is requested. Some literature studies propose alternatives to equipment modelling w.r.t. the case with lumped mass [9].

- An additional issue to take into account is the modelling of links between equipment and payload units. As a matter of fact, the junction area usually includes items with different mechanical and thermal properties (bolted connections, inserts, washers, glue). This leads to an increase of complexity and uncertainty sources for themo-elastic purpose, mainly when it is dealing with composite materials.

In the current practice, several mapping methods on the structural model are used and they differ for the type of code, for the mapping assumptions and for the level of automation; figure 1.2 provides a summary of these approaches. The latter are described in the present chapter and the description is mainly focused on the inverse distance weighting algorithm. Once the described data exchange is achieved, the temperature distribution appears on the FEM as a load whose density may be considered a piece-wise continuous map on the spatial domain; otherwise, these loads could be thought as concentrated loads applied to each FEM nodes. These mapped data are used on a structure to perform stress analysis or to determine thermal expansion.

Considering MSC Nastran, it is possible to define a temperature distribution using the TEMP-type bulk data entries [10, 8]. For example, the temperature could be specified for elements by the following entries:

- TEMPRB card for the elements CROD, CBAR, CBEAM, CBEND, CONROD, TUBE; this entry specifies the average value on both ends and in case of CBAR, CBEAM and CBEND it is possible to define a temperature gradient over the cross section.

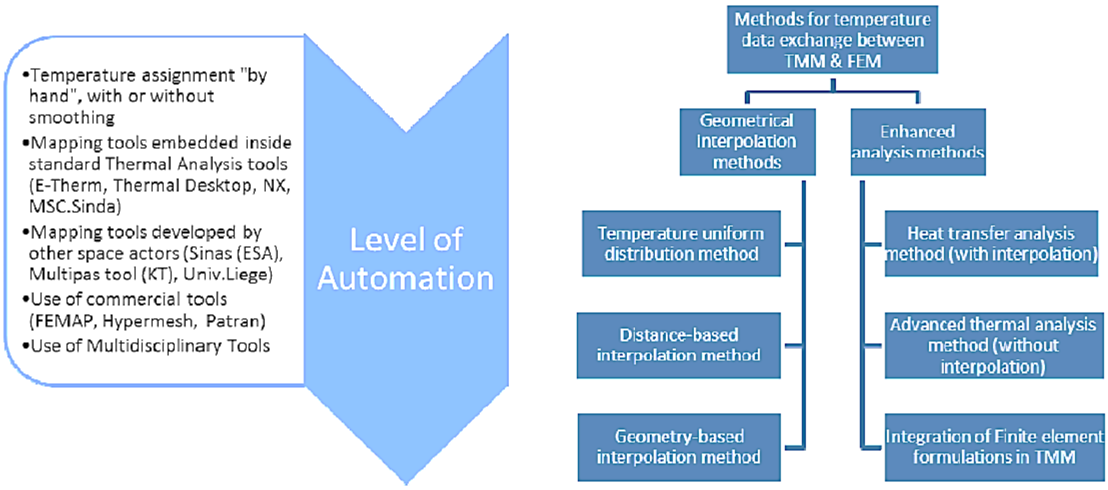

Figure 1.2. Temperature mapping methods chart, according to the automation level and physical assumptions.

- TEMPP1 card for two-dimensional plate and membrane elements. The defined average temperature over the volume is exploited to obtain in-plane loads and stresses. Furthermore, the thermal gradients over the profoundness of the bending elements might be used to induce bending loads and stresses.

Otherwise, the temperatures may be specified at grid points, using the TEMP and TEMPD cards [11]. The latter entries are used in the present work. Moreover, the thermal expansion coefficients are set on the material bulk data entries [8].

1.2.1 Hand-operated assignment procedure

During this procedure, the thermal node temperature is applied on a group of finite elements, or on their nodes, that belongs geometrically to the thermal node. In broader terms, this approach is also called patch-wise temperature application method since it recalls a patch-work [4]. This procedure might be simple but it implies to establish the correspondence between thermal and mechanical nodes. The latter could be done by hand, with the help of spreadsheet programs, during which the analyst has to make a non-negligible effort to establish the right geometric correspondence. In alternative, it is possible to automate the assignment by coding specific tools, in the available programming languages; this approach is often tied to the use of the author, or of a small group of users, and it lacks of generality when adapted ad hoc on a case-by-case basis. In addition, a high risk of errors is possible, due to the high quantity of data to be checked. Basically, this type of mapping does not introduce physical aspects that could reproduce a continuous-like temperature field on the FEM; however, it can be integrated with heat transfer conductive analysis, in order to smooth physically the discontinuities.

1.2.2 Interpolation approach based on conduction

The basic idea of this method is to apply on the FEM a set of known temperatures, given as Dirichlet boundary conditions, and to run a steady state conduction heat transfer analysis. For example, in Nastran the temperatures can be assigned with SPCD entries [8] and *SOL 153* can be used.

Therefore, it is used a physical ingredient as the conduction matrix and the generated temperature field takes into account changes in conduction due to geometry, material and interfaces. Examples may be the Centre-Point Prescribed Temperature (CPPT) method [4], using Nastran, and the Prescribed Average Temperature method (PAT), implemented in ESA tool SINAS.

1.2.3 Geometrical interpolation algorithms

Some commercial software and some pre-processors like Tecplot, FEMAP, PATRAN, HYPERMESH offer the possibility to interpolate temperature values on the FEM grid, considering the spatial position of a set of known values assigned to the thermal nodes. The coordinates of the geometric centre of the thermal nodes and the temperatures associated with them are used. Some methods are: inverse distance weighting, Delaunay triangulation, Kriging. The main drawback of these methods is that no physical information is considered.

In the present study, the inverse distance weighting based interpolation is extensively analysed.

1.2.4 The inverse distance weighting based interpolation

The inverse distance weighting, denoted as IDW, is a deterministic interpolation approach widespread in geosciences and, for example, it is used in Geographic Information System (GIS). It acts as spatial interpolation and it is able to estimate unknown values at specific locations, based on sampled values of surrounding points in space [12]. Potentially, it is possible to obtain a continuous layer of values starting from a set of data taken at sample positions [13]. In the case of temperature mapping on the structural model, the described interpolation could tend to reproduce a continuous temperature distribution, assigning values to all the nodes of a detailed FEM; in such way the approach may replicate the physical behaviour of a spatially-based continuously changing phenomena as the temperature. Undoubtedly, to reach a physically meaningful temperature distribution, on the FEM, is not so straightforward. In fact, several drawbacks are related to this type of interpolation likewise many possible methods to overcome limitations, based on the scope of the application, as explained in the available copious literature (e.g. [12, 14, 13, 15, 16, 17]). Below, the IDW working principle is explained and the main disadvantages are underlined.

Let's consider the temperature mapping context, calling:

- $\hat{T}(P_0)$ the temperature assigned value at the estimated point P_0;
- $T(P_i)$ the temperature associated value at the i-th sampled point P_i;
- $d_{0,i}$ the Euclidean distance between points P_0 and P_i;
- W_i the weight assigned to the i-th measured value T at P_i;
- N the number of nearest points with measured values surrounding P_0.

Therefore, the stated estimation of the unknown temperature value at the generic non-measured point P_0 is given by the following expression:

$$\hat{T}(P_0) = \sum_{i=1}^{N} W_i \cdot T(P_i), \tag{1.2}$$

where the i-th weight is given by

$$W_i = \frac{\frac{1}{d_{0,i}^k}}{\sum_i^N \frac{1}{d_{0,i}^k}}, \tag{1.3}$$

with

$$\sum_i^N W_i = 1. \tag{1.4}$$

The numerator of equation 1.3 is the inverse of distance between P_0 and P_i with a power parameter $k \geq 0$; moreover, the denominator is the sum of the inverse distance weights for all the nearest points i [12, 15]. Lastly, the sum of the W_i's for the generic estimated point P_0 is equal to one, as shown in 1.4. The exponent k implies that:

- if $k > 1$ the distance decay effect is higher than simple proportionality, increasing $d_{0,i}$;
- a low k tends to estimate $\hat{T}(P_0)$ as the arithmetic mean of the nearest sampled P_i's points values, in the neighbourhood of P_0; so if $k = 0$ it is assigned the same weight for all the nearest points;

- a high k gives a strong weight to the nearest points and a very low weight to the farthest points; for example considering a sampled point P_1 concerning a distance $d_{0,1}$ and a second known location P_2 relative to a distance $d_{0,2} = 2 \cdot d_{0,1}$, for $k = 3$ it is possible to notice that doubling the distance, the weight given to P_2 is about 87% lower than the nearest P_1.

Remark 2 In summary, the two extreme cases are showed in the following.

a) $k \to 0 \Rightarrow W_i = \frac{1}{N}, \quad \hat{T}(P_0) = \sum_{i=1}^{N} \frac{1}{N} \cdot T(P_i)$.

b) Let call P_q the i-th nearest point to P_0; this implies that $d_{0,q} = min\{d_{0,i}\}$.

If $k \to \infty \Rightarrow W_i = \begin{cases} 1 & i = q \\ 0 & i \neq q \end{cases}, \quad \hat{T}(P_0) = T(P_q)$.

The main advantages of this method are:

- the interpolation is simple and intuitive, w.r.t. other more complex spatial interpolation approaches;
- the Tobler's first law of geography [18] assumption validity implies that it is not necessary to identify a theoretical distribution for the sampled data;
- the algorithm is fast to compute the interpolated values.

Among the several disadvantages, it is possible to mention that:

- the explained parameters k and N are chosen a priori and it means that they are exogenous w.r.t. the sampled data [15, 16];
- the variances of the predicted values are not estimated;
- a sensitivity to outliers and sampling configuration is present.

The latter point of the list above implies that the parameter k is homogeneously applied to all the studied component. The implication of this drawback is that the distribution of the sampled data is not taken into account and so a uniform distance decay relationship over space is considered. Therefore the density of the closest sampled points number could be different for several non-sampled locations but the changes in the known data clustering are not taken into account by k and N defined a priori.

For example, let consider a honeycomb panel of the Euclid primary structure explained in paragraph 2.1.1; on the FEM of this panel are overlapped the data coming from the TMM as red spheres representing the thermal nodes geometric centre. Therefore, in figure 1.3 it is clear that in the neighbourhood of point A there is a higher number of TNs w.r.t. to point B; so, for the reasons mentioned above, it may be desirable to use a lower k for point A, to give uniform weights to the neighbour thermal nodes and to avoid excessive influence by the nearest TN. On the contrary, for point B is better to use a higher k to associate more weight to the nearest TN, giving less influence to the more distant sampled locations.

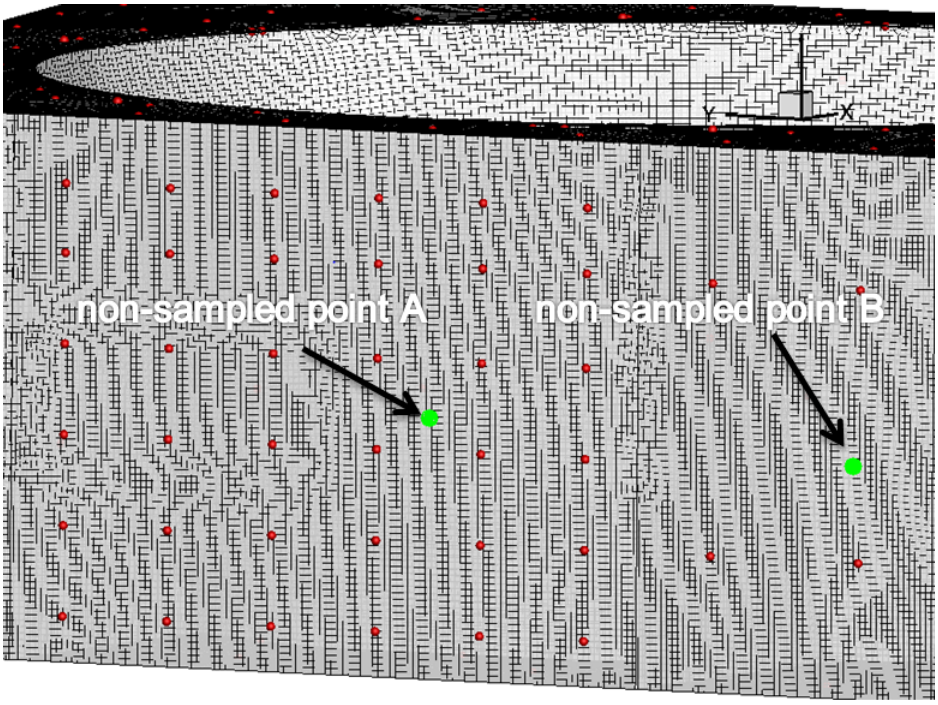

Figure 1.3. Example of different sampled points clustering.

An interesting study by Lu and Wong [15] proposed a solution to overcome these limitations combining IDW and the Kriging [19, 20] method and obtaining, by statistical functions, an adaptive IDW; so, in the latter solution, the exponent of the distance changes based on the sampled data clustering. On the other hand however, other authors (e.g. [12, 21]) suggest precise values of the exponent based on satisfactory empirical results or experience; some of these proposals concern $k = 1, 2, 3$.

Furthermore, an other important issue to observe is the choice of the N, defined above. Even in this case, several works propose some solutions as in the case of the initial IDW study by Shepard [12]. Basically, to select N two criteria are used:

- an arbitrary distance approach, using a sort of search radius with the origin in the non-sampled point (fig. 1.5);
- an arbitrary number N approach used in the present study, as showed in paragraph 2.1.

Remark 3 Regarding the present work area of interest, two additional drawbacks are underlined:

- the interpolation is based on a geometric approach and no physical properties (e.g. thermal expansion coefficient, thermal conductivity) are considered;
- if the main satellite structure is not split into more suitable substructures, a wrong temperature association could occur, due to the proximity of thermal and structural nodes belonging to different panels; figure 1.4 schematises this problem.

In this thesis, a deterministic IDW parameters tuning is used in chapter 2 to evaluate the displacements sensitivity of some relevant zones of structural model and the variation of the temperature mapping on FEM, changing the aforementioned k and N.

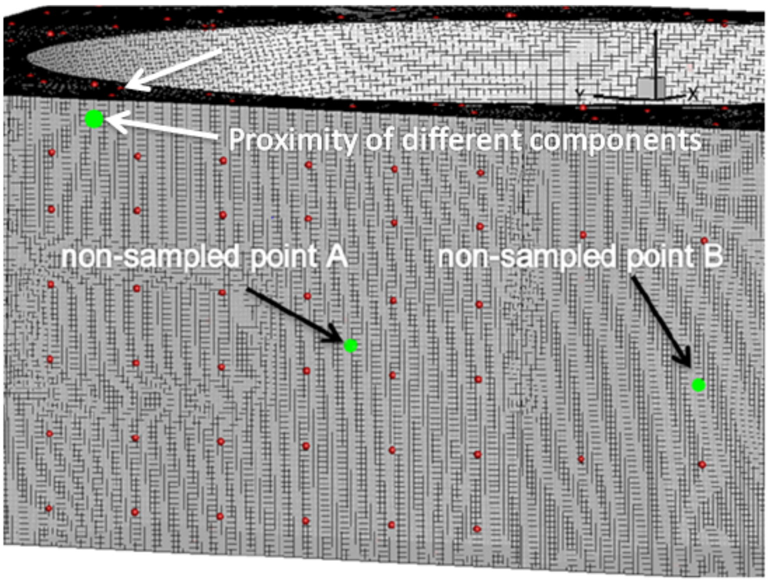

Figure 1.4. Proximity example of different panels and consequent wrong temperature assignment.

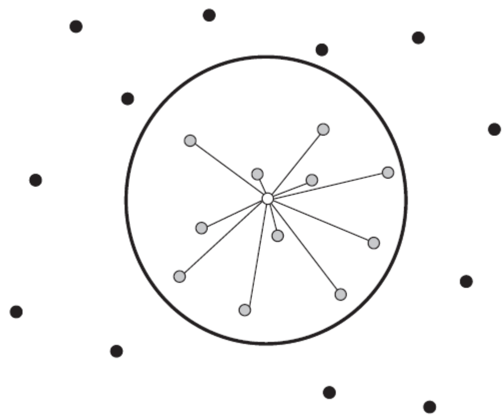

Figure 1.5. Example of search radius used in a two-dimensional problem.

1.3 The *MaREA* code

MaREA is an integrated system tool developed by Thales Alenia Space Italy, in *Torino*. This software, based on MATLAB language, is able to assist, in a time saving way, the spacecraft design and the mission sizing; so the advantage is the simplification, automation and standardisation of the data transfer phase between system disciplines, especially in the early stages of a program. One possible implication is that a concurrent engineering of the system architecture occurs. Initially, the development of MaREA tool took form by the case-study related to the IXV (Intermediate eXperimental Vehicle) program but, without a lack of generality, the tool structure was designed to be suitable for using on different space programs and not only limited to the atmospheric re-entry.

The MaREA structure is arranged by modules (figure 1.6), in order to establish an optimised dialog between the MATLAB environment and the spacecraft design disciplines. For each field of study, the software provides at least two modules to import or export a set of data, and possibly their associated geometry, into or from MATLAB environment [22]. In addition, the presence of additional tools to aid the pre-processing, the post-processing and the data exchange phase is the strong point of MaREA platform. For example, during the development of the present work, the additional function *Allinea* was also used to merge the TMM and FEM of IRIDIUM structure, thanks to a rotation and translation of the global reference frames systems of the two models. Table 1.1 provides a list of disciplines and their relative tools that can be exploited by MaREA thanks to the mentioned import and export functions.

As explained in the user manual [22], a typical workflow used by the software to transfer data (e.g. pressures, temperatures, displacements) among models is the following:

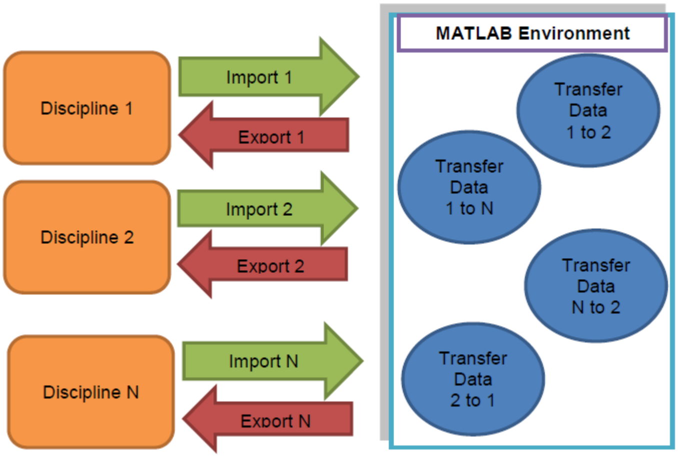

Figure 1.6. MaREA modular approach. Adapted from reference [22].

- import of the models M_1 and M_2 into MaREA;
- generation of the transfer function $F(geometry)$;
- import of the data-set $\{D_1\}$ into MaREA;
- data interpolation from M_1 to M_2, by the product $F \times \{D_1\}$: a new data-set $\{D_2\}$ associated to M_2 is generated;
- export of $\{D_2\}$ in the chosen or native format of M_2.

Furthermore, tree types of transfer function are available:

- inverse distance weighting algorithm;
- overlapping method;
- TEMASE.

The first and the last transfer algorithms are used in chapters 2 and 3.

Table 1.1. Main interface functions among different disciplines. Adapted from reference [22].

Discipline	Tool	Function
Aerothermodynamics	Tecplot	Import and export
	Ensight	Export
	ATDB interpolation function	Export
Thermal control	ESATAN-TMS GMM	Import
	ESATAN-TMS output temperature	Import
	ESATAN-TMS heat flux time histories	Export
	Excel GMM description	Export
Structure	Nastran Bulk	Import
	Nastran output displacements .f06	Import
	Nastran output displacements .op2	Import
	Nastran output displacements .out4	Import
	Nastran temperature TEMP cards	Export
	Nastran pressure PLOAD cards	Export
	TEMASE procedure within Nastran	Import and export
	Nastran influence matrix and deformations (TEMASE output)	Export
Optics	CodeV input file	Import
	CodeV interferometric data	Export
	CodeV rigid body roto-traslations	Export

Chapter 2

Evaluation of the MaREA temperature mapping algorithm on a case-study

A case-study approach was adopted to evaluate the MaREA transfer function based on the IDW algorithm. The latter is used to assign a temperature map to the FEM starting from the temperature distribution associated to the TMM. To assess the influence of the two variable parameters of the IDW, as explained in paragraph 1.2.4, w.r.t. a set of fixed output displacements of the structural model, a sensitivity analysis was performed.

This chapter shows a thermoelastic study of displacements using the mentioned interpolation function, varying the described IDW numerical parameters. The aforementioned investigation was assayed using a simple case-study inherited by the Euclid program.

Remark 4 In the continuation of the present study, regarding the variable parameters of the distance based interpolation approach (IDW), the following notation is adopted:

- N: number of nearest nodes;
- k: exponent of the distance.

The meaning of these variables is explained in paragraph 1.2.4.

2.1 Apparatus and procedures

In order to perform the proposed sensitivity analysis, the following mathematical models were considered:

- a thermal mathematical model (TMM) generated by Esatan-TMS;
- a finite element model (FEM) devised in the MSC Nastran environment.

These patterns are representative of a typical spacecraft case and they are a simplified part of the Euclid project models (figure 2.1). This choice was adopted to reduce the simulation time and to handle the TMM and FEM easily during the data transfer preparation between the two different environments. In addition, further complications in the numerical models are out of the scope of this didactic activity. Lastly, the general adopted working procedure is the following:

1. thermal and structural models conversion into MATLAB format, by MaREA import functions;
2. interpolation function generation, adopting the MaREA IDW algorithm, varying k and fixing N;
3. temperatures transfer into structural model and consequent Nastran TEMP cards generation [10];
4. Nastran input file writing for each given exponent and so for each set of TEMP cards;
5. temperatures distribution analysis on the finite elements models, to assess the extent of loads discontinuity;
6. static linear analyses by Nastran, to obtain the thermoelastic deformations at the chosen set of the recovery structural nodes and for each selected exponent;
7. output displacements conversion into MATLAB environment, by MaREA, and results analysis.

The latter explained road-map shows the main passages of iteration followed, fixing the number of nearest nodes and varying the exponent of the distance, in the IDW algorithm (see paragraph 1.2.4); in addition it was also repeated adopting different values for the number of nearest nodes.

2.1.1 Mathematical models description

An overview of the Euclid simplified model is showed in figure 2.2. The structure consists of:

- honeycomb panels, with junction elements between them;
- star tracker (STR) mounted on the top platform, for the pointing recovery;

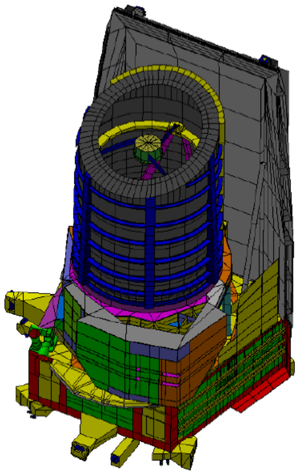

Figure 2.1. Euclid GMM.

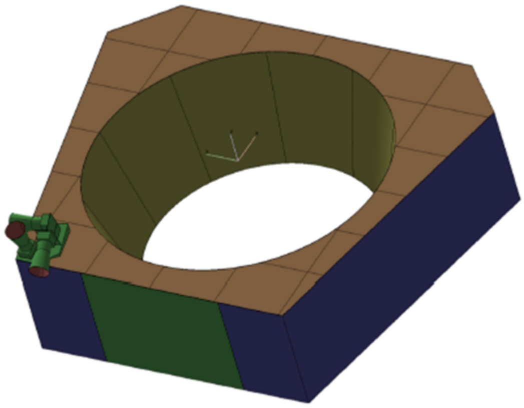

Figure 2.2. Overview of the Euclid model.

- two equipment boxes placed internally and on opposite sides, one close to the STR position.

Remark 5 About the structure panels, the following notation is used:

- main panels lying on the positive and negative part of z axis, perpendicular to it: panel +z and panel -z respectively;

- main panels lying on the positive and negative part of y axis, almost perpendicular to it: panel +y and panel -y respectively;

- panel lying on the positive part of x axis, perpendicular to it: panel +x.

The structural model was created using the software Nastran and Patran; the figures 2.3 and A.1 show an overview of the finite element model. The table 2.1 provides the total number of elements and cards used to build the FEM. The parts identified in this structural model are set out in the list below and their related figures are inserted in the annex A.

- **Upper and lower platform.**

  They are the +z and -z panels, made of a sandwich structure. An appropriate property is assigned to these panels using the PCOMP Nastran card [8]. The figures A.2, A.3 provide views of these platforms.

- **Central cone assembly, shear webs and lateral panels.**

  All these components are made of a sandwich structures and the properties are assigned by PCOMP Nastran cards [8] (figures A.4, A.5).

- **Connections, star tracker and equipment boxes.**

  The six connections between the service module and the payload module (PLM) are modelled by Nastran rigid elements RBE2 [8] (figure A.6). The star tracker is formed by a bar element CBAR [8], that appears in a yellow colour in figure A.8, connected by RBE2 to the panel +z. In addition, The mentioned connections are linked by RBE3 [8] element, as shown in figure A.7. Lastly, the equipment boxes are an example of the satellite on-board data handling subsystems [2] and they are modelled by a network of RBE2 elements that connect the box centre of gravity to the location of the bolts on the lateral panel; figure A.9 shows a detail of the explained equipment modelling. These boxes are called *central data management unit* (CDMU) and *power control data unit* (PCDU).

The recovery points analysed to compare different displacements varying the mapping parameters are the following: star tracker extremity, six interface connections between service module and payload module; table 2.2 summarises these points.

The GMM and TMM were created in an ESATAN-TMS environment and provided by the thermal analysts. Therefore, the thermal model is composed of 469 thermal nodes but the number of TNs used for the thermoelastic analysis perspective is 227. A key aspect is to simplify as much as possible the analysts data handling and to reach this purpose only the thermal nodes that affect thermal-elasticity are

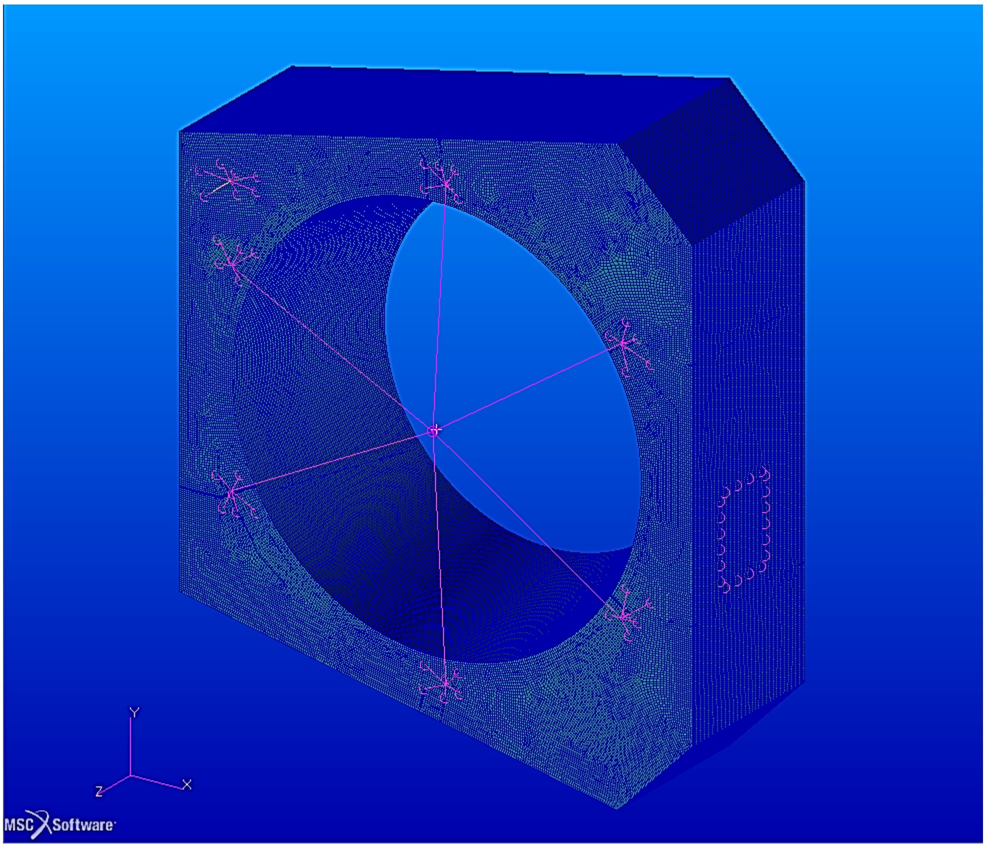

Figure 2.3. FEM isometric view.

Table 2.1. Structural model summary.

FEM	
Bulk data entry	**Number of entries**
CBAR	1
CBUSH	657
CONM2	2
CORD2C	2
CORD2R	31
CQUAD4	232886
CTRIA3	94
GRID	237667
MAT1	2
MAT8	4
PARAM	4
PBAR	1
PBUSH	55
PCOMP	6
RBE2	9
RBE3	1

Table 2.2. Grid ID of recovery points.

Recovery grid ID	Description
1118963	Star tracker node at the base
1194012	Star tracker node at the top
1900004	RBE2 interface nodes
1900005	
1900006	
1900007	
1900008	
1900009	
59289710	RBE3 node

selected, when the MaREA transfer function is created. For example the multi-layer insulation (MLI) blankets [23] thermal nodes are not considered in the FEM. Figure 2.4 shows the number of TNs for each substructure considered in the analysis. A partial thermal nodal breakdown of the GMM and temperature map is provided in the figures 2.5, 2.6. It is underlined that the TMM is adapted to be used in MaREA code and so the format explained in section 3.3 of the user manual [22] is adopted.

Lastly, basing on the conceptual framework proposed by some internal documents and by thermal and mechanical analysts, a second TMM, with a lower number of TNs, is examined. The reason of the latter choice lied on the necessity to asses the thermal mesh size impact on the thermal-elastic analysis results. This new model is composed of 201 nodes and the number of TNs used for the thermo-elastic analysis perspective is 79, as shown in figure 2.7; therefore, the thermal mesh size is much lower than the previous one and it leads to a reduction of the temperature map details, that affects the thermal loads description on the structural model. Figure B.3 shows a comparison of two geometrically identical panels (+z), considering the two different nodal breakdown. The temperature map in the case of coarse TMM is provided in figures B.1, B.2.

Remark 6 To distinguish the two described TMM, the following notation is adopted:

- TMM-A: to indicate the one with 469 thermal nodes.
- TMM-B: to indicate the one with 201 thermal nodes.

2.1.2 Temperatures mapping

According to MaREA working flow, the first step to perform a temperature mapping on the structural model is to check or to obtain consistency between global reference frame systems of the satellite geometrical models, created in different software environments for mechanical and thermal design purpose. Obviously, a coherence is necessary between FEM and GMM regarding the overall primary and secondary

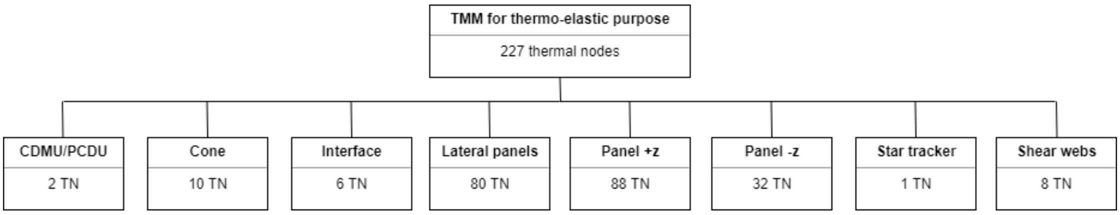

Figure 2.4. Distribution of TMM nodes.

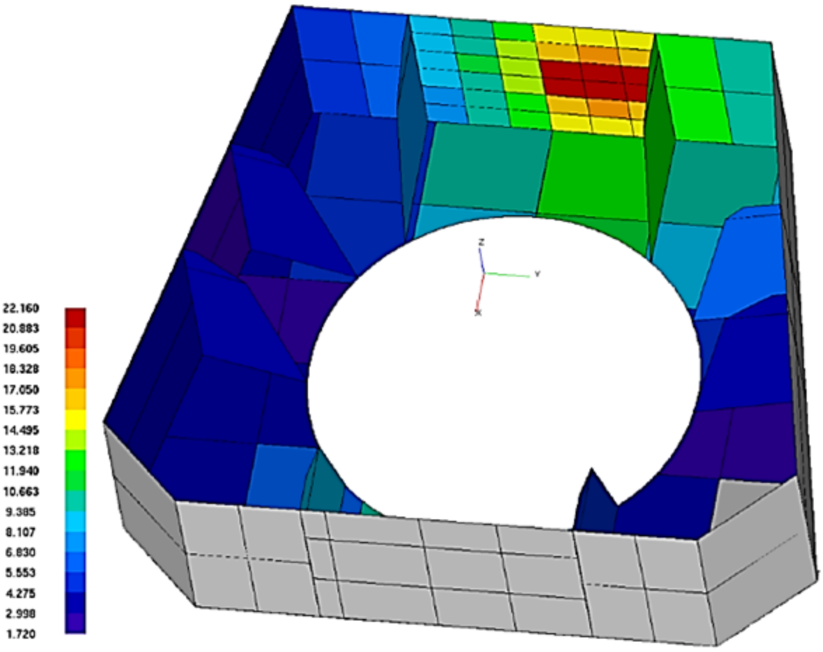

Figure 2.5. TMM nodal breakdown and temperature map (+x view); $[T]$ = °C.

structure dimensions and the correct arrangement of equipment. In fact the data transfer function used is based on spatial interpolation and so an appropriate overlapping of the TNs set on the FEM is crucial, to avoid artificial associations of temperatures on the finite elements nodes. Figure 2.8 shows the aforementioned coherence in the Euclid case-study; the TNs appear as red spheres representing the thermal nodes geometric centre.

Remark 7 The temperatures associated to the thermal nodes are applied at the geometric centre of the TNs shape. In the present work, due to the operation of MaREA transfer functions, the TN is always considered as lumped into its geometric centre.

To avoid the drawbacks discussed in 1.2.4, the FEM was split into five main substructures, according to section 2.1.1: +z panel, -z panel, central cone, lateral

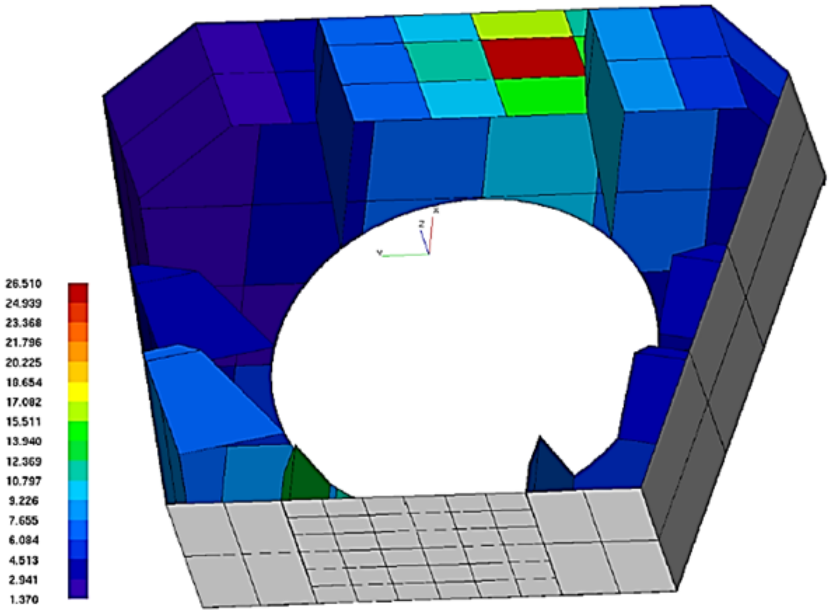

Figure 2.6. TMM nodal breakdown and temperature map (-x view); $[T] = °C$.

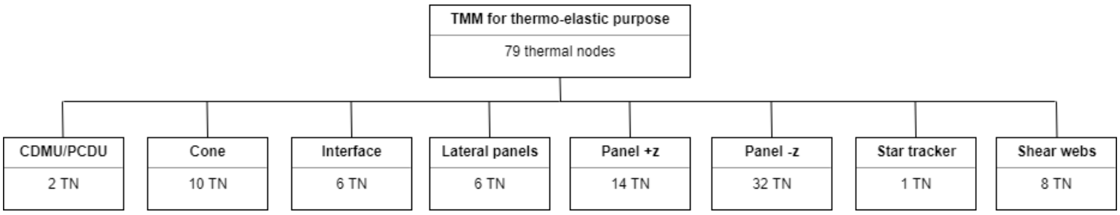

Figure 2.7. Distribution of the coarse TMM nodes.

panels, shear webs, interface elements, star tracker, PCDU/CDMU elements. The number of assigned TNs to these substructures is provided in figure 2.4.

The analysed cases, introduced at the beginning of section 2.1, are listed as follows:

Case-I $N = 12$ and $k = 0,1,\ldots,16,100$;

Case-II $N = 8$ and $k = 0,1,\ldots,16,100$;

Case-III $N = 5$ and $k = 0,1,\ldots,16,100$;

Case-IV $N = 3$ and $k = 0,1,\ldots,16,100$;

Case-V $N = 1$ and $k = 0,1,\ldots,16,100$.

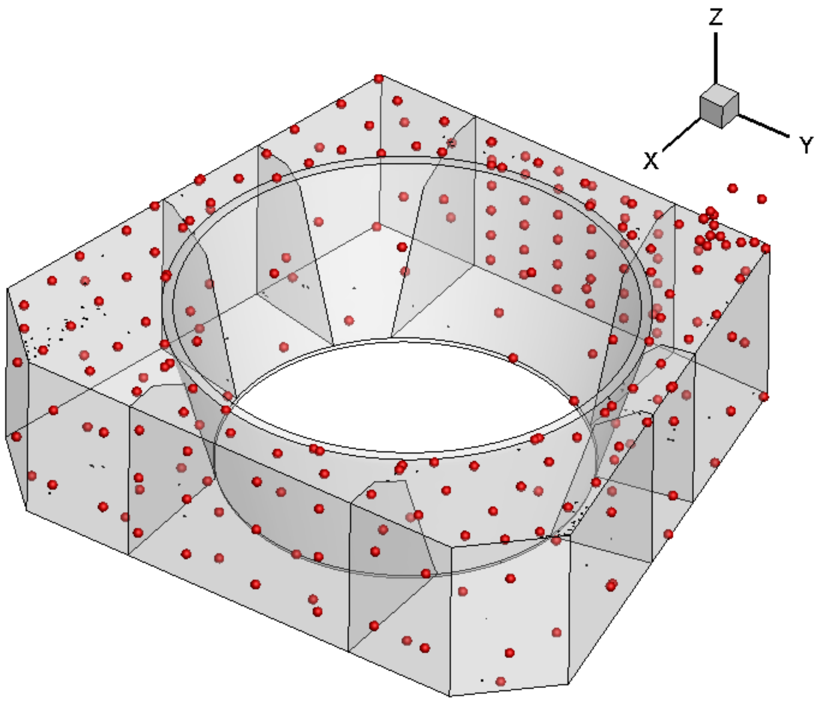

Figure 2.8. Overlap of TMM-A on the FEM.

These cases imply that for each N there are 18 sub-cases and as many temperature maps on the FEM. Therefore, the total number of mapping is 90. The reasoning behind the choice of these values can be treated as follows:

- $k = 0$: it is used to asses the mapping behaviour in the lower IDW extreme case (see remark 2); in addition it may return good results at non-sampled locations with highly clustered TNs in their neighbourhood.
- $1 \leq k \leq 5$: these values fall into the range of those suggested by the numerous literature and they are adopted by commercial software like Tecplot [24].
- $6 \leq k \leq 16$: they are considered in order to investigate the spatial algorithm behaviour in a range out of the canonical one.
- $k = 100$: it is used to asses the mapping behaviour in the upper IDW extreme case (see remark 2); clearly, this relatively high value reproduces numerically, in our study context, the instance $k \to \infty$.
- $N = 12$: it gives the possibility to take into account more TNs further from the estimated point, when in the neighbourhood an increase of sampled data occurs. It is important to state that if in a FEM substructure the TNs number is less than 9, no difference occurs w.r.t. $N = 8$.

- $N = 8, 5$: usually, this set of values is considered in the aforementioned literature and in commercial software; it represents a good logic assumption for the IDW, based on the heritage related to this argument.
- $N = 3$: this number could permit to assign more weight to the closest thermal nodes regardless of the k variation, excluding the extreme cases.
- $N = 1$: this number induces a temperature mapping almost equivalent to the one discussed in section 1.2.1; it follows that the temperatures distribution is equal $\forall k$.

The five cases explained above are performed considering the model TMM-A and the set of recovery points listed in the table 2.2.

Some additional cases were analysed to evaluate other aspects that could influence the thermoelastic analysis and the sensitivity of output displacements to the variation of N and k; these cases are described in the list that follows.

Case-VI Some additional hot spots are added to the model TMM-A; as showed in the figure 2.10, 90 W are included to the previous temperature map; in addition $N = 8$ and $k = 0,1,\ldots,16$. This modification increases the overall thermal-elastic deformations of the structural model, resulting in a possible more influence, on the outputs, of the temperature transfer algorithm.

Case-VII To study the influence of a reduction in thermal model mesh size, the model TMM-B is used; in addition $N = 8$ and $k = 0,1,\ldots,16$. Figure 2.11 shows the TNs as red spheres overlapped to the FEM.

Case-VIII A new set of recovery structural nodes is considered, in order to evaluate the displacements on the lateral panel +x, that exhibits the maximum temperature and the highest temperature difference along the structure; these points are showed in figure 2.9. It is possible to notice that this new nodes are taken where the temperature discrepancies are more pronounced. In addition this case is performed considering the model TMM-A, $N = 8$ and $k = 0,1,\ldots,16$.

Finally, for a better assessment of the convergence range of deformations w.r.t. the temperature mapping and of the influence of local thermal nodes clustering, the following last cases are considered:

Case-IX In order to be sure about the convergence range of the temperature distribution on the FEM, a set of simulations are used considering $k = 18,19,\ldots,52$ and $N = 8$, once the sensitivity regarding N is obtained in the cases from I to V. This case is compared w.r.t. the case II.

Case-X This case is adopted in order to verify the behaviour of the algorithm in a range of lower exponents. Therefore the following parameters are used: $N = 8$, $k = 0{,}0.1,\ldots,1.7$. It is underlined that the interval between consecutive exponents is 0.1. This choice could allow to obtain a better interpolation in the areas with a local increase in the number of TNs and in the temperature gradient; in such way a discontinuities attenuation and a more physical behaviour might be reachable. On the other hand, due to the lack of an adaptive-like parameters tuning, a wrong temperature transfer might be possible where the sampled data are distributed on wide areas (see section 1.2.4).

The table 2.4 presents a summary of all the analysed cases. Table 2.3 shows the second set (Set-2) of recovery points, taken into consideration in the case VIII. The figures B.4 and B.5 provide the ID (identification number) and the temperature field for the two set of recovery nodes.

Remark 8 It is possible to notice that from case VI to X, N is equal to eight. This choice is attributed to the will of evaluate additional aspects that influence the thermoelastic analysis, without excessively increasing the number of cases to be analysed.

Table 2.3. Grid ID of recovery points on the lateral panel.

Second set of recovery grid ID	Description
49579632	Lateral panel +x
49593862	
49589551	
49590886	
49590619	
49585105	
49584826	
49580425	
49579928	

In the following of this chapter some further considerations and qualitative examples of temperature mapping done on the FEM are inserted, considering each of the aforementioned cases.

Remark 9 To avoid any misunderstanding, it is underlined that, in the continuation of this chapter, the word *case* is adopted to indicate the set of all the *sub-cases*, fixing N, adopting a given TMM and varying k.

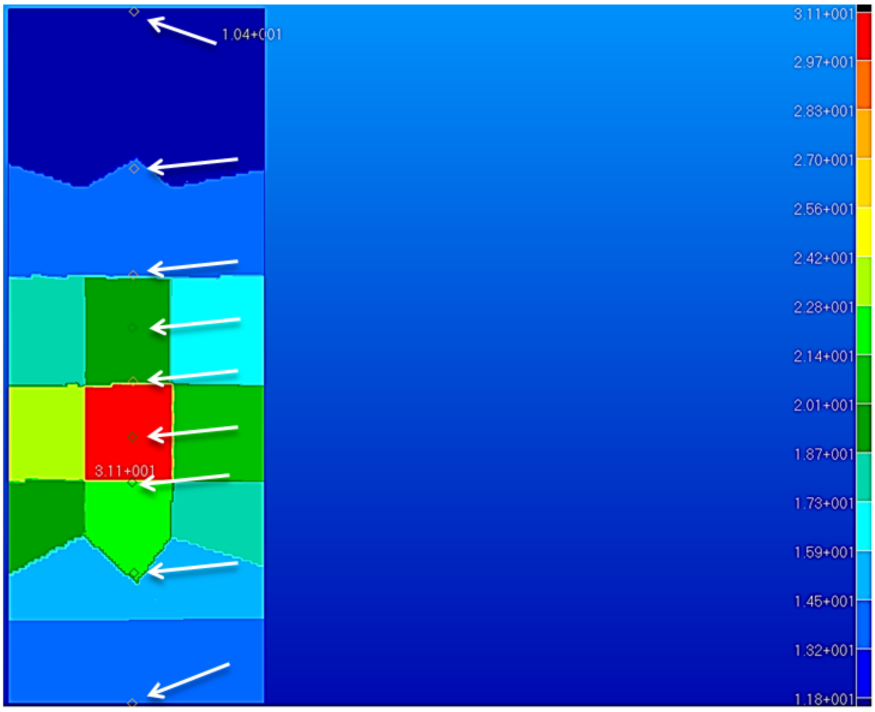

Figure 2.9. New set of recovery points, on the lateral panel, as indicated by the arrows; $[T] = °C$.

Table 2.4. Euclid cases summary.

Case	**TMM**	**Recovery nodes set**	**N**	**k**
I	TMM-A	Set-1	12	0,1,...,16,100
II	TMM-A	Set-1	8	0,1,...,16,100
III	TMM-A	Set-1	5	0,1,...,16,100
IV	TMM-A	Set-1	3	0,1,...,16,100
V	TMM-A	Set-1	1	$\forall k$
VI	TMM-A with additional 90 W	Set-1	8	0,1,...,16,100
VII	TMM-B	Set-1	8	0,1,...,16,100
VIII	TMM-A	Set-2	8	0,1,...,16,100
IX	TMM-A	Set-1	8	18,20,...,52
X	TMM-A	Set-1	8	0,0.1,...,1.7

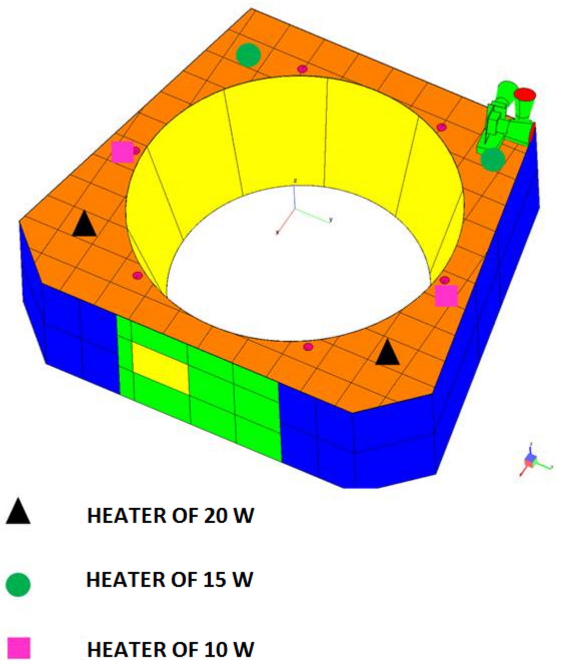

Figure 2.10. Zones of the thermal powers added to the model TMM-A.

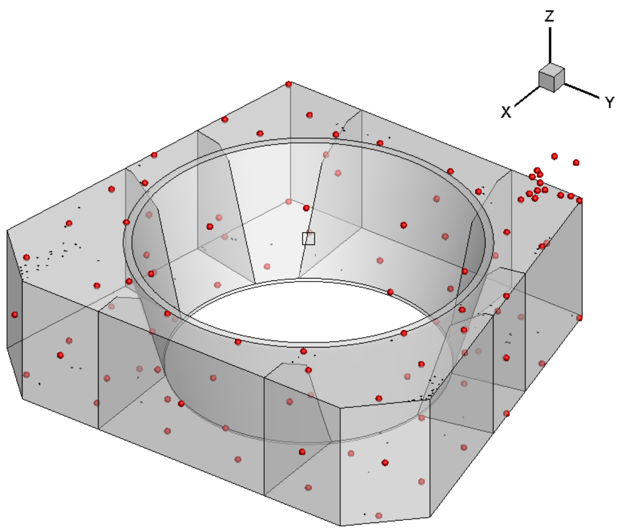

Figure 2.11. Overlap of TMM-B on the FEM.

2.1.3 Thermal-elastic and sensitivity analysis

Once the finite element model has been created and once all the properties of the materials and elements, as well as the temperatures at the structural nodes, have been assigned, according to the appropriate Nastran cards, it is possible to run a linear thermoelastic analysis using the static solution *SOL 101*, in the executive control section [11]. It is underlined that a thermoelastic model adequacy control, as showed in section 11.2.1.2 of reference [1], has been performed in previous studies on the same Euclid service module used in the present work; therefore, this phase is not repeated below. Moreover, according to the analysed cases, the number of simulations performed is greater than one hundred; for this reason, in order to repeat automatically the working procedure exposed at the beginning of section 2.1, an important effort was necessary to write several codes in the MATLAB environment, able to repeat the aforementioned working procedures for all N and k.

The additional assumptions and procedures adopted in this part are the following:

- the variables N, k, TMM-A, TMM-B, Set-1 and Set-2 are considered as independent;
- the translations and rotations of the recovery nodes are function of the mentioned variables, exposed for the ten cases;
- for each recovery node is computed the resultant modulus of translations components and the components resultant modulus of an axial pseudo-vector representing the overall rotations in space, considering the global reference frame system;
- the displacements obtained by setting $N = 1$ are considered as reference values; they almost represent the achievable results if a patch-wise temperature application is performed and so reproducing the same method often adopted in the industrial practice;
- to assess the influence of the two variable parameters of the IDW w.r.t. the set of fixed output displacements of the structural model, for each case is employed:
  - a graphic comparison of results;
  - a normalised root-mean-square error (NRMSE) for different intervals of k w.r.t. the case relative reference value.

The NRMSE is adopted to estimate the deviation of results w.r.t. the adopted reference value, in terms of percentage error. These errors have been computed for all the analysed cases and taking into account different ranges of values for the exponent k. The formula is:

$$NRMSE = \frac{\sqrt{\frac{1}{N}\sum_{i=1}^{N}(D_i - \bar{D}_i)^2}}{\bar{D}}, \tag{2.1}$$

where, in the present context, N is the number of the exponent values in the studied range, D_i is the predicted value of displacement and $\bar{D} = \bar{D}_i$ is the constant reference value adopted. Therefore, the higher the error the stonger is the influence of the two variable parameters of the IDW.

2.2 Results and discussion

In general, the first result to underline is that for each set of simulations a convergence in terms of temperature mapping on the structural model and of deformation outputs is reached for $k \geq 4$, as confirmed by graphic comparison and by the fact that $NRMSE < 2\%$ in the mentioned range; this trend is confirmed for any value of nearest nodes (N). Secondly, a higher outputs sensitivity to the exponent change is present for $0 \leq k \leq 3$. Moreover, as could easily be deduced, in this interval the higher the N the higher is the NRMSE. Figures B.6 and B.7 show the temperature field for the reference case.

2.2.1 From case I to case V

The main results and considerations are inserted in the following list.

- Regarding case I, the number of nearest nodes is quite high, according to the presented literature; therefore, for some substructures (e.g. the internal cone), the total number of TNs is taken into account during the temperature mapping. It means that, potentially, all the thermal nodes provide a non-negligible contribution to a given FEM node, causing a loss of information on the temperature distribution. The latter happen mainly for low values of $k \leq 2$ since a more homogeneous weight is given to all the nodes considered. Figures B.8 shows the latter drawback. Figure B.9 provides an example of temperature field for $k = 1$; it is possible to notice that some good temperature mapping are obtained near areas with strong temperature gradients or with an increase in the TNs density. The trend for $k \geq 3$ exhibits a slight smoothing of temperature discontinuities where an increase of gradients or of the TNs number occurs, as in case of figure B.10.

- The case II shows, for $k \leq 2$ a slight difference in terms of temperature mapping, where a local TNs clustering occurs, as for the lateral panels with PCDU and CDMU equipment (figure B.12). Figures B.15 and B.16 provide examples of temperature field for the case X, comparable w.r.t. the figure B.12. Moreover, the choice $k = 0$ leads always to obtain a non-reliable data exchange, as showed in figure B.11.

- In general, according to the obtained results, it is underlined that for $N = 12,8,5$ and $0.8 \leq k \leq 1.5$ a reliable interpolation is reached, concerning always that local areas where an increase of temperature gradients or of the TNs number occurs. Therefore, a more physical temperature assignment might be replicate. An example of this consideration is provided by figures B.9, B.12, B.16, B.17, B.18.

- Regarding the case IV, an example of temperature field for $N = 3$ and $k = 1$ is showed in figure B.19. In this set of simulations, since the number of nearest nodes is lower, the risk of take into account wrong TNs during the interpolation is reduced. On the other hand, the possibility to smooth almost physically the discontinuities, for $k \leq 2$ is partially lost.

- As underlined above, for $k \geq 4$ and for any N the temperature mapping tends to reproduce the same results in terms of temperature field and also of thermo-elastic deformations.

- As mentioned in section 2.1.2, $k = 100$ is used to asses the mapping behaviour in the upper IDW extreme case (see section 1.2.4) and so to reproduce numerically, in our study context, the instance $k \to \infty$. Nevertheless, considering the results, this choice proved useless for the following reasons:
  - the choice $k = 16$ is sufficient to have an example of upper IDW extreme case;
  - numerically, low distances with exponent -100 gives infinite.

- In appendix C are inserted a set of bar charts that compare for each node of Set-1 the resultant modulus of translations and of rotations. Considering also the worst scenario of non-reliable results in terms of temperature mapping (i.e. usually when $k = 0$), three main trends are evident:
  - for any N if $k \geq 4$ the displacements tend to converge;
  - at the same value of N, if $k \leq 3$ the difference between the actual case and the reference one ($N = 1$) can be also higher than 10 µm, in case of translations, or 10 µrad, in case of rotations; however, only for sporadic cases, this gap is greater than 20 microns, remaining nearly always below ten microns;
  - even if $k \leq 3$, when $N = 3$ the displacements approach mainly to the reference values.

  Table C.1 provides a comparison among different intervals of k, using the aforementioned NRMSE in percentage and considering the translations. In general there are relatively low percent errors with respect to the extent of the deformations involved. The same considerations apply to table C.2 which refers to the rotations. Looking at these tables, it is possible to confirm the evaluations highlighted above. In addition, the overall amount of NRMSE experiences a slight fall in case of rotations w.r.t. the translations case.

2.2.2 From case VI to case VIII

Table C.3 shows the main results of this simulation set. Further considerations are inserted in the following list.

- The case VI shows an overall increase of deformations by adding thermal power to the +z panel of the model TMM-A. In addition, a slight sensitivity of deformations w.r.t. the exponent is still present for $k \leq 3$, even if it can be considered negligible; the latter result may be somewhat counterintuitive. As a first instance, could be possible to deduce the following:
  - not enough cases have been done in order to obtain a reliable trend;
  - the distortion threshold is high enough to make the spatial interpolation contribution ineffective, to detect slight variations in deformations of the structure, already very stressed;
  - the local number of thermal nodes is not sufficient to evaluate correctly the thermal behaviour, considering the new amount of thermal power.
- The case VIII shows similar considerations to those made for case II.
- A comparison between the case VII and the case II shows, consistently with the internal literature, a strong difference between the thermal models TMM-A and TMM-B in terms of translations and rotations. Considering for example the Set-1, this difference can reach 70 µm and exceed 100 µrad for some nodes. Moreover, in most cases, this discrepancy is greater than 20 microns. A comparison among the displacements obtained with the two thermal models is inserted in figures C.20, C.19, C.21, C.22,C.24, C.23, C.25, C.26. This dissimilarity is given by the following reasons:
  - for TMM-B, the level of mesh detail does not allow to have a good and realistic temperature field over large areas, giving back an average of the temperature physical distribution present in the area belonging to the wide thermal node;
  - the great loss of detail concerning the temperature field, resulting from a thermal simulation with less TNs, results in a consequent loss of information on the FEM and so in different structural deformations.

Further considerations on these results are presented in the chapter 4.

Chapter 3

The assessment of stability performance of a satellite structure

In this part of the study a typical procedure for pointing stability analysis is performed on a representative satellite structure. In general, this procedure is useful when several temperature data interpolations are necessary (i.e. transient analysis) to compute the displacements of a set of recovery FEM points. Therefore, this method gives the possibility to obtain deformations using a simple multiplication between matrices, instead of transferring all the temperature vectors from TMM to FEM for each analysed case [25]. The goal of this method is to obtain local mechanical deformations and performance contributions on the FEM, applying unitary thermal loads of 1 °C [25]. As second step, this local information is combined in matrix form and they are multiplied by a matrix containing all the temperature vectors belonging to the transient thermal analysis of the satellite. As a result, a matrix with the actual structural deformations is obtained, according to the linearity hypothesis. Therefore, two matrices are used:

- the unitary loads matrix, also called influence matrix (IM) or sensitivity matrix;
- the thermal loads matrix, provided by thermal analysts, with all the temperature vectors to be studied.

This method is also used to determine the models zones where higher influences on thermo-elastic output is present, in order to assess the key contributors to the stability performance [25, 4]; so it is possible to evaluate further improvement on meshing or on physical representation of these sensible areas, to increase the results numerical prediction according to the mission needs.

In this chapter two methods to obtain the IM and the actual structural deformations are compared; in particular, an approach with a low level of automation, which can be considered manual, and an almost totally automated approach, thanks to the MaREA code, are considered.

3.1 Constructing the unitary load matrix

In general, to build the IM the following conceptual steps are necessary:

- to associate the nearest thermal node for each mechanical node, in coherence with the geometry and the spatial coordinates, in order to obtain a set of thermal zones;
- to rise, one at a time, by 1 °C each thermal zone, in order to have the response of all the structure to this unitary and local perturbation.

The IM is the set of all unitary structural contribution to the deformations. In general, it is possible to define:

$$IM = \begin{bmatrix} \gamma_{11} & \cdots & \gamma_{1j} \\ \vdots & \ddots & \vdots \\ \gamma_{i1} & \cdots & \gamma_{ij} \end{bmatrix}_{n \times m},$$

where the coefficient γ_{ij} is the unitary load contribution for the j-th thermal zone on the i-th mechanical node. Therefore, the amount of rows represent the number of chosen recovery structural nodes and the columns are the aforementioned thermal zones.

Remark 10 In the context of the present study, the matrix dimension n is given by the set of all the translations and rotations considered for each recovery mechanical node, in the three dimensional reference frame system.

The thermal load matrix or thermal matrix is the following:

$$TM = \begin{bmatrix} \Theta_{11} & \cdots & \Theta_{1k} \\ \vdots & \ddots & \vdots \\ \Theta_{j1} & \cdots & \Theta_{jk} \end{bmatrix}_{m \times p},$$

where Θ_{jk} is the temperature of the j-th thermal node at the k-th instant of the transient thermal results. Therefore the number m is equal to the TNs number and the value p is the number of the selected temperature vectors to be studied. This matrix is provided by the thermal analysts. As mentioned above, the matrix product between IM and TM gives a linear combination of unitary contributions and thermal loads:

$$[\mathbf{Q}] = [\mathbf{IM}][\mathbf{TM}], \quad where \quad Q = \begin{bmatrix} q_{11} & \cdots & q_{1k} \\ \vdots & \ddots & \vdots \\ q_{i1} & \cdots & q_{ik} \end{bmatrix}_{n \times p} .$$

The matrix $[\mathbf{Q}]$ is the set of all the output response. Therefore, the result is:

$$q_{ik} = \sum_{j=1}^{m} \gamma_{ij} \Theta_{jk}, \tag{3.1}$$

where the summation term $\gamma_{ij}\Theta_{jk}$ is the actual weighted contribution of the j-th thermal node to the i-th requested response at the k-th instant. Therefore, q_{ik} may be a displacement, a stress or an unknown response of the system. In the present study context, q_{ik} can be a translation or a rotation along the three reference axes, for a given mechanical node.

The numerical procedure to construct IM is obtainable in several ways, using finite element analyses codes and programming languages. Once again, a key aspect is the consistency between the geometries and the global coordinate systems adopted for the mathematical models, in the two different calculation environments; such correspondence makes it possible to reach an appropriate association between FEM and TMM. Once the latter has been reached, the IM is the result of a suitable finite element analysis.

Considering for example the Nastran code, in the case control section is defined one *SUBCASE* [11] for each thermal zone. Subsequently, the unit thermal load is applied to all the structural nodes belonging to and associated with the current thermal zone, by the command *TEMPERATURE(LOAD)*; the latter recalls the definition of the unitary increase in temperatures, present in the bulk data section as TEMP-type entries [8]. The constant temperature of reference, to which the increment is applied, is usually set at 20 °C. During the main Nastran simulation, for each sub-case the code applies the rise in temperature, leaves the temperature of the remaining sub-cases unchanged and returns the effect of this perturbation on the set of recovery nodes; therefore, a number of mechanical linear analyses equal to the number of thermal zones is performed. The influence matrix is thus computed and may be assembled by means of an appropriate post-processing. Following, there is a partially listed example of case control section and bulk data section for this purpose:

```
$
SOL 101
$
CEND
TITLE =  (to be defined)
ECHO = (to be defined)
```

```
SPC = 1
AUTOSPC(NOZERO)=YES
RIGID=LAGR
$
SET 100 =  (to be defined)
$
DISP(PLOT) = 100
DISP(PUNCH) = 100
STRESS(PLOT) = 100
$

(missing part)

$
TEMPERATURE(INITIAL)=99999999
$
SUBCASE         1
LABEL= (to be defined)
TEMPERATURE(LOAD)=         1
$
SUBCASE         2
LABEL= (to be defined)
TEMPERATURE(LOAD)=         2
$
SUBCASE         3
LABEL= (to be defined)
TEMPERATURE(LOAD)=         3
$

(missing part)

$
BEGIN BULK
$

(missing part)

$
TEMPD    99999999     20.
$
$
$
TEMPD           1     20.
$
TEMP            1 1011549    21.00
TEMP            1 1011550    21.00
TEMP            1 1011616    21.00
TEMP            1 1013361    21.00
TEMP            1 1013372    21.00

(missing part)

$
```

As introduced at the beginning of this chapter, the advantages to use the explained procedure are the following:

- only one numerical simulation, linked to the assembling of IM, is needed, to assess several thermal load cases;
- to build the IM is sufficient to establish a priori, with the thermal analysts, the number and the arrangement of the thermal nodes of the primary and of the secondary structure;
- by a simple matrix product, it is possible to obtain quickly a displacement, a stress or an unknown response of the system;
- to determine the model zones where higher influences on thermo-elastic output is present, in order to assess the key contributors to the stability performance.

Some limitations of this approach may be summarised as follows:

- in case of very detailed TMM and in absence of procedure automation, a considerable effort has to be made in order to divide properly the FEM in thermal zones, to define the Nastran sub-cases, to correctly set the temperature rise of the structural nodes belonging to the considered sub-case;

- the IM validity depends on the initially defined thermal nodal breakdown and so further TMM changes affect it;

- it is not possible to integrate this method with an interpolation method which takes into account heat transfer analysis, trying to reproduce a more physical distribution of temperatures on the FEM, starting from a coarse TMM.

In the sections that follow are provided examples to overcome some of the drawbacks related to this approach.

3.1.1 Automatic procedure implemented in MaREA

As previously stated, the multidisciplinary tool MaREA provides an algorithm called TEMASE, acronym of Temperature Mapping Sensitivity, which is able to generate the Nastran analysis launch files; the latter are suitable to compute the terms γ_{ij} and so the influence matrix, as articulated in the explanation above. In this way the IM building procedure is completely automated, reducing the writing and the verification time of the launch files. In addition, further MaREA post-processing functions are able to assemble the IM, loading the Nastran output f06, op2 or out4 files [22, 10]. The main inputs needed by TEMASE are:

- a file with the IDs and the coordinates of the thermal nodes, in the global coordinate system;

- a file containing the FEM in *NASTRAN GRID* entry format [8];

- a set of files with the IDs of all the satellite substructures, both for TMM and FEM, in order to be used during the temperature transfer process [22], avoiding the drawback explained in section 1.2.4.

To summarise the overall procedure, needed by MaREA to assemble the IM and to obtain the displacements, the working steps are the following:

1. thermal and structural models conversion into MATLAB format, by MaREA import functions;

2. creation of the thermal zones on the structural model and writing of all the Nastran SUBCASE and the related TEMP-type entries, by TEMASE algorithm;

3. execution of the Nastran static linear analysis, including the Nastran BULK-DATA and SUBCASE cards generated by TEMASE;

4. assembling of the influence matrix into MATLAB data format, by MaREA post-processing functions;

5. generation of a spreadsheets file containing: [**IM**], [**TM**] and [**Q**].

Remark 11 The creation of thermal zones on the structural model, i.e. the association of the generic mechanical nodes to the closest TN is performed by the function *temase* [22] thanks to a spatial interpolation, equal to the one used in chapter 2. In particular, it is adopted the IDW method with $N = 1$. This correspondence between the two types of node allows to apply the local unit temperature increase. Therefore, a constant value of 21 °C is set on all the FEM nodes of the related sub-case.

Remark 12 Using the automated TEMASE approach, it occurs that the thermal nodes number of the TMM coincides with the thermal zones number on the FEM and so with the number of Nastran sub-cases. It is underlined that, in industrial practice, using different procedure to obtain the IM, especially for manual writing of Nastran files, the number of thermal zones on the FEM and so the number of sub-cases may be different from the TNs number. The latter occurs based on how satellite substructures and connection elements are processed.

3.2 Application case: the *IRIDIUM NEXT* platform

The procedures exposed above were applied to a test article, representative of a typical satellite structure: the IRIDIUM NEXT platform. The latter is the aim of the study of an experimental validation campaign in the field of thermo-elasticity, currently underway. Similarly to the Euclid case-study, the mathematical models are designed in MSC Nastran and ESATAN-TMS environments.

3.2.1 Mathematical models description

The aforementioned test article consists of a primary structure and of three subsystems. Referring to the FEM in figure 3.1, the former is mainly composed of:

- aluminium honeycomb panels +x, -x, +y, -y, +z, -z;
- internal stiffeners;
- connection elements.

The three sub-systems are:

- a sandwich structure composed of three panels, in composite material, defined as *bridge structure* or simply composite structure;
- an antenna support realised in additive manufacturing, called also *ADPM support* (Antenna Deployment & Positioning Mechanism);
- a telescope mock-up, defined also *DSS telescope simulator* (Dynamic Satellite Simulator).

Figure 3.2 shows an overview of the FEM with the primary and secondary structure. Moreover, it is underlined that:

- the junction elements are modelled with rigid elements RBE2 [8];
- the primary structure panels are mainly designed with Nastran surface elements (e.g. CQUAD4 [8]);
- the ADPM support is made of Nastran solid elements;
- the telescope is primarily composed of line and surface elements;
- the bridge structure is modelled with surface elements.

The total amount of the FEM structural nodes, which are combined with TNs, is 446699. In addition, it is underlined that an iso-static suspension of the satellite is set on panel +z of the FEM, consistently with the mentioned testing configuration.

Regarding the GMM and TMM, they were created in ESATAN-TMS environment. The thermal model is composed of 475 thermal nodes but the TNs used for the thermo-elastic analysis purpose are 469, as shown in figure 3.3. Similarly to chapter 2, only the TNs that affect thermal-elasticity are selected, when the MaREA transfer function is created. Therefore, the multi-layer insulation (MLI) blankets are not considered on the FEM of the telescope or the bridge structure. Figure D.1 shows the nodal breakdown of the primary structure. In figures 3.4 and 3.5 it is possible to notice the nodal breakdown of the sub-systems. The overall TMM was subsequently adapted to be used in the MaREA code and so the format explained in section 3.3 of the user manual [22] is adopted. It is underlined that, in order to achieve a more realistic test configuration, the MLI, considered on the DSS cylinder and on the composite structure internal surface, has the function of isolation, of the relative subsystems, w.r.t. the radiative environment.

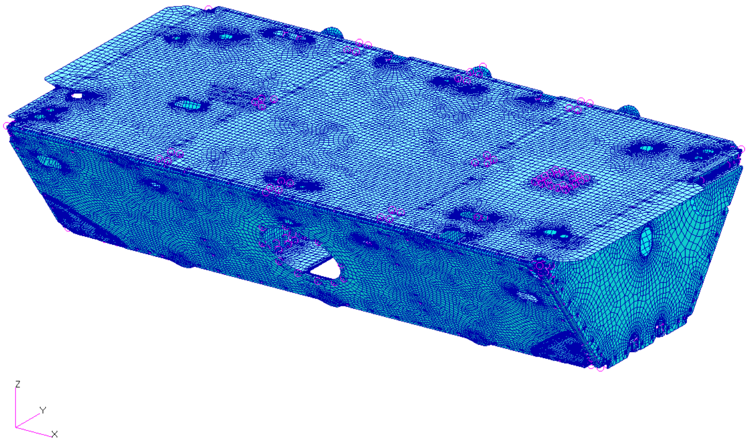

Figure 3.1. FEM of the IRIDIUM primary structure.

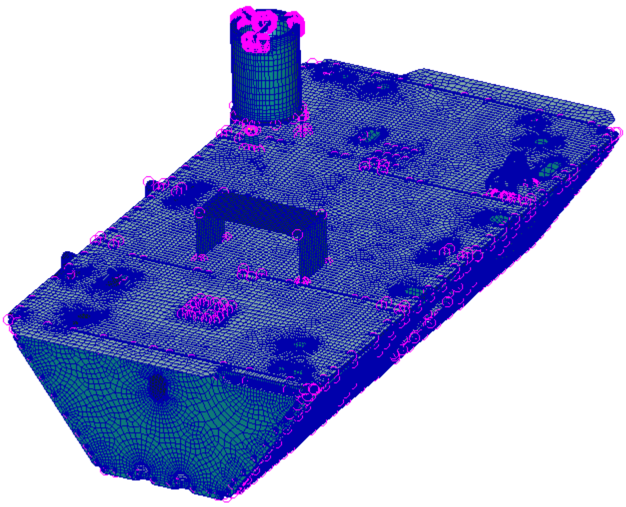

Figure 3.2. FEM of the IRIDIUM primary and secondary structure.

3.2.2 Thermal-elastic and sensitivity analysis

Before the choice of recovery nodes and before the thermo-elastic analysis, according to the method exposed in section 3.1, a preliminary coordinates modification of some thermal nodes was carried out. Indeed, there was an inconsistency between global coordinate systems of the two mathematical models; in addition, the thermal nodes geometric arrangement of some subsystems was conflicting with their position in the case of structural model. Consequently, a series of iterations were necessary, through some functions integrated into the MaREA code, to bring the two models

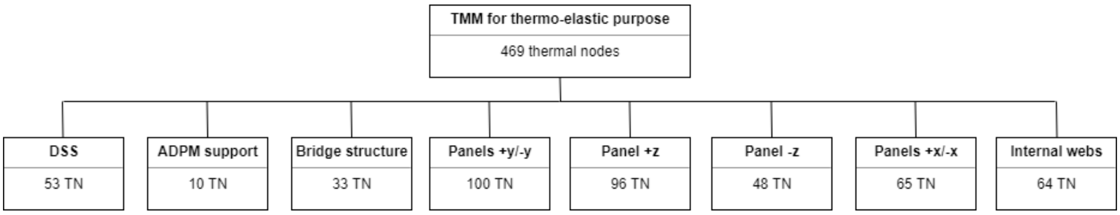

Figure 3.3. Distribution of TMM nodes, for IRIDIUM NEXT platform.

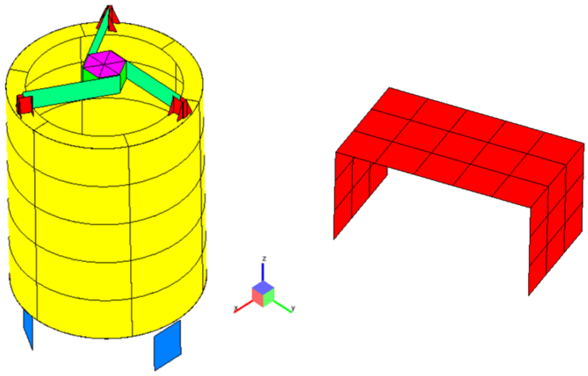

Figure 3.4. Thermal model nodal breakdown of the DSS and of the bridge structure.

back to congruence. Figure D.2 is an example of some inconsistencies; the figure 3.6 shows the right overlap between the two models, considering the thermal nodes as red spheres (see remark 7). Therefore, it is underlined that, thanks to the additional functions integrated in MaREA, it was possible to modify the thermal model without using the dedicated software. Moreover, before the phase of association of the TNs on the FEM, the satellite was split into more suitable substructures to avoid wrong TNs association, due to the proximity of thermal and structural nodes belonging to different elements. The substructures are: the ADPM support, the DSS telescope, composite structure lateral panels, composite structure +z panel, +x/-x panels, +y/-y and +z/-z panels.

The recovery points adopted for the thermo-elastic analysis are set according to the testing configuration of IRIDIUM; they are explained in the list below.

– Panel +z

On the Earth panel (+z), a set of 91 output locations are considered. In particular, they are located on seven equidistant lines which extend throughout the panel along the x direction and thirteen equidistant lines along the y axis. Figure 3.7 shows the structural recovery points. Furthermore, as the image demonstrates, each position is labelled with a capital letter and a number, to simplify the visualisation; the same

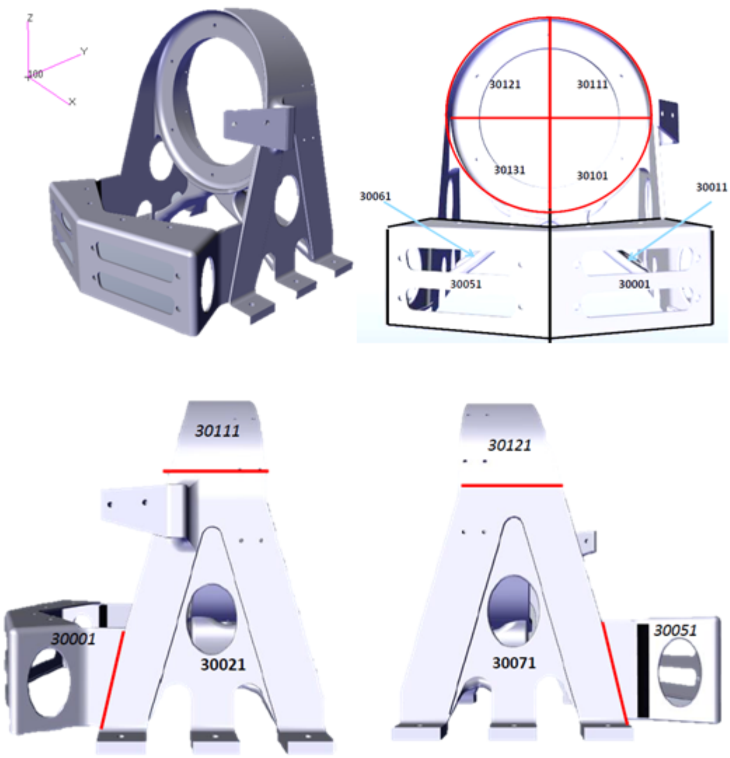

Figure 3.5. Thermal model nodal breakdown of ADPM support, with nodes numbering.

letter or number is respectively used for each horizontal or vertical line.

– DSS telescope

For what concerns the telescope, it is considered a set of 12 output locations; these points take into account: brackets at the cylinder top, parts of mirror (M1 or M2) cages, portion of the crown and of the external surface of the cylinder. These recovery nodes are well showed and labelled in figure 3.8.

– ADPM support

A set of 6 output locations are adopted on the antenna support; three at the top and three at the bottom, as presented in figure D.3.

– Composite structure

In the case of composite structure, all the TNs are taken into account. Figure D.4 provides some labels of the recovery nodes positions.

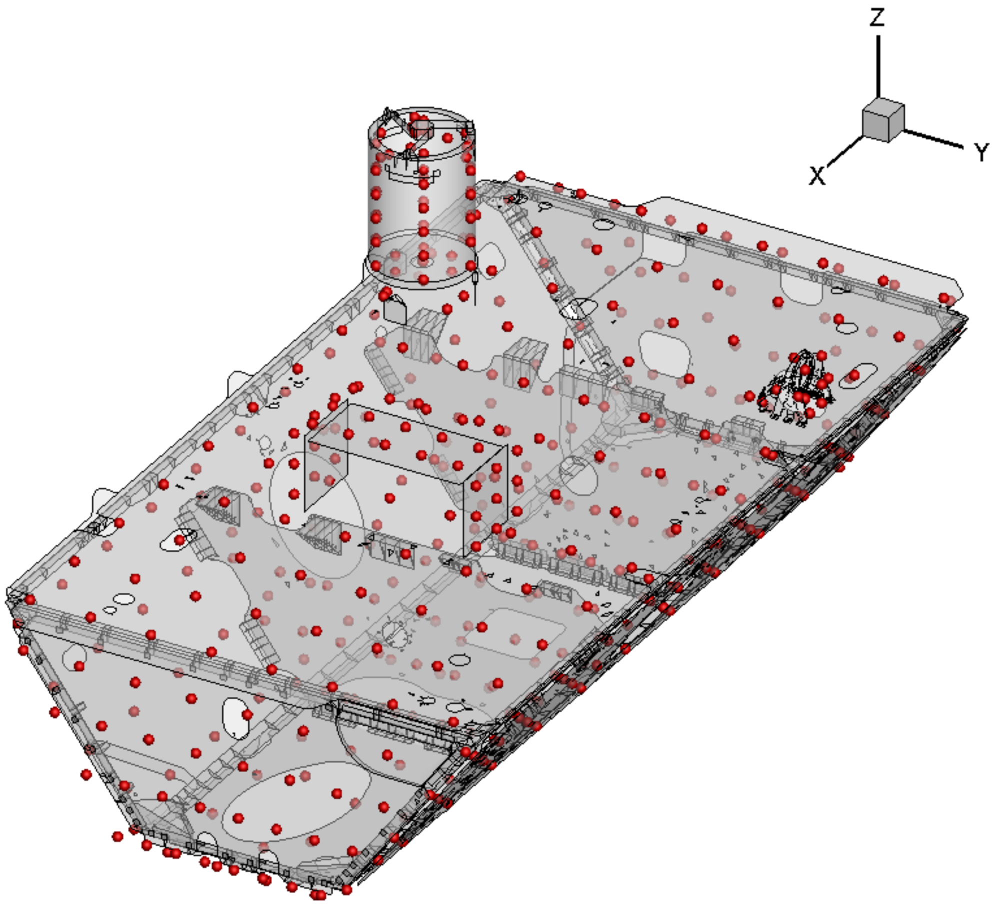

Figure 3.6. Overlap of the TMM (red spheres) on the FEM.

Therefore, the total amount of recovery structural nodes is 142. For each of these points, the unitary load contribution is computed for the j-th thermal zone on the current mechanical node, considering translations and rotations in the coordinate system: $T_x, T_y, T_z, R_x, R_y, R_z$. All these components represent the dimension n of the influence matrix, as underlined in remark 10.

Once the geometric consistency between the two models is verified and once the set of recovery structural nodes is chosen, the IM is obtainable, according to the method explained in sections 3.1 and 3.1.1. A subsequent verification of the procedure is achieved thanks to some tools integrated in TEMASE. For example, the figure 3.9 shows each generated sub-case as coloured spot around the related thermal node which appears as a black sphere. It can be seen that each zone of the structural model, including the subsystems, is associated with a TN. In addition, thanks to the Tecplot environment, an internal stiffener and some internal brackets are visible and consistently subdivided into thermal zones, according to the adjacent

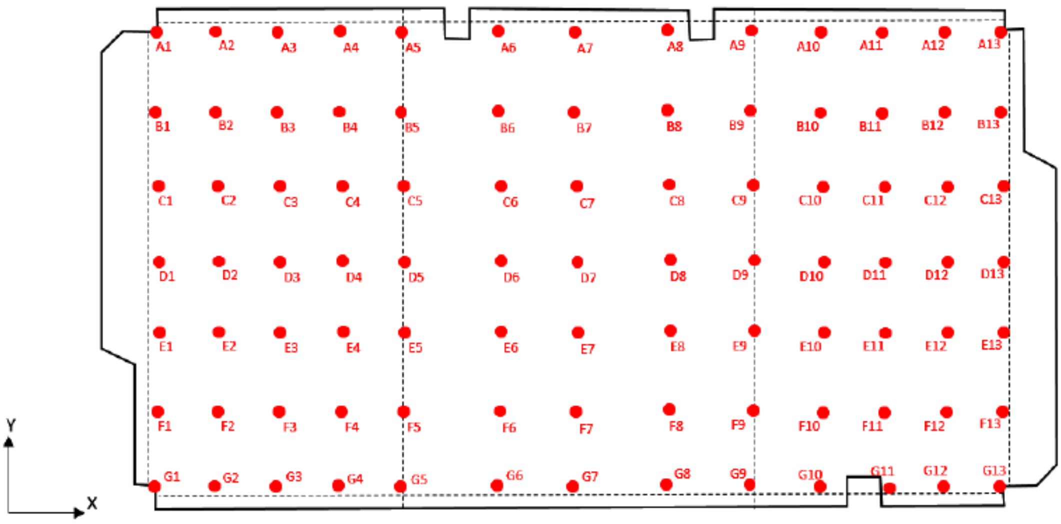

Figure 3.7. Earth panel output locations.

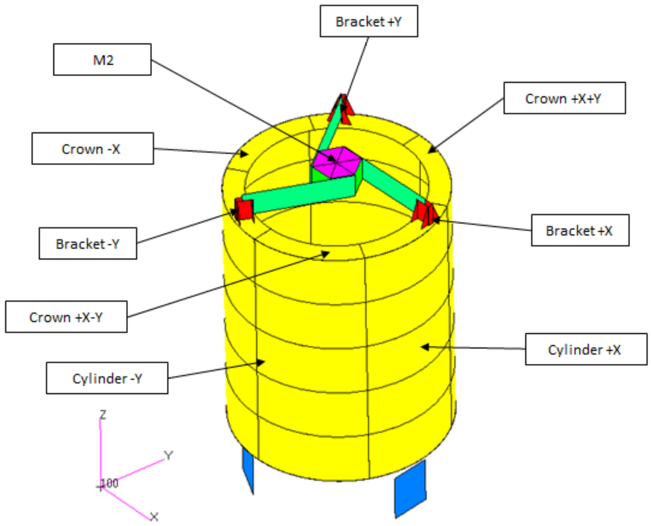

Figure 3.8. DSS output locations.

panels.

To obtain part of the aforementioned matrix [**Q**], a temperature vector representative of a test configuration is used; a hypothesis of active thermal control system, equipped with heaters, is taken into account in the ESATAN numerical simulation. The complete temperature values distribution on the satellite is shown in the figures D.5, D.6, D.7, D.8, D.9, D.10, D.11, D.12, D.13, D.14, D.15. Thus, the obtained deformations are compared with those resulting from an approach with a low level of automation, often adopted in the industrial practice. In the present study context,

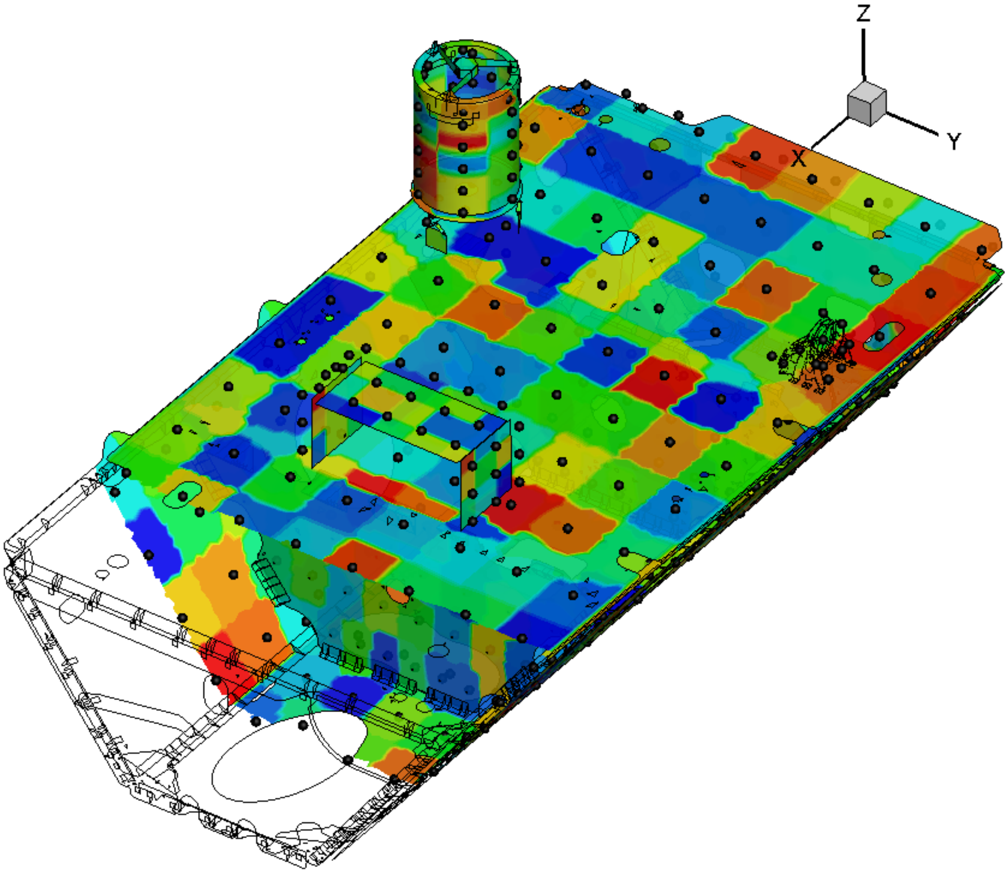

Figure 3.9. TEMASE check of Nastran subcases.

this latter method is called also manual and it can be summarised as follows:

- manual split of the FEM into thermal zones, thanks to spreadsheets file and specific tools of the software MSC Patran;
- manual definition of *case control section* and of *bulk data section*, according to the file pattern explained in section 3.1;
- deformation calculation by spreadsheets and ad hoc codes.

3.2.3 Results and discussion

In order to visualise the extent of deformations and to compare the two mentioned approaches, for each structural recovery node is employed:

- a detailed presentation of the translations and rotations obtained by TEMASE;
- a graphic comparison of results for the two methods;
- a qualitative evaluation of computational time needed to build the IM.

Table D.1 provides all the translations and rotations for the recovery nodes belonging to the Earth panel. The tables D.2, D.3 and D.4 include the results of the three subsystems. The labels that appear in these latter four tables are consistent with those stated in section 3.2.2; it can be notice that, for each set of deformations, the maximum value, the minimum value and their difference is highlighted. In general, basing on numerical simulation, the extent of deformations, both according to a positive or a negative axis direction, is detectable by distortion measurement systems (e.g. videogrammetry), during the testing configuration; for example, more than the 90% of mechanical nodes translations are $\geq$ 10µm. Therefore, the chosen thermal load case is adequate to be employed in the experimental validation campaign.

To visualise the extent of differences between the aforementioned methods, used to generate the IM and to obtain the deformations, the figures D.16, D.17, D.18, D.19, D.20, D.21, D.22, D.23, D.24, D.25, D.26, D.27, D.28, D.35, D.36, D.37, D.38, D.39, D.40 provide scatter plots for comparison; they are a version of the known mean-difference plot [26]. Considering two values of translations or rotations calculated with the two approaches, for the same structural node and for the same reference axis, on the abscissa are indicated the arithmetic averages between them and on the ordinate the differences between them. Furthermore, the mean of the differences is highlighted. In this way it is possible to obtain the magnitude of discrepancy between the two values and eventually to evaluate which method overestimates or underestimates the actual value. In the absence of experimental results, the abscissa values are considered as a reference.

– Panel +z

The panel +z is subjected to the highest translations along the z direction, perpendicularly to the plane on which the component lies. These displacements interfere significantly with the stability and orientation of the payload. In order to better visualise the deformation mode, the figures 3.10 and 3.11 show the component T_z considering respectively the recovery nodes horizontal lines, identified by the capital letter in the labels, and the nodes vertical columns, given by the fixed numerical label. It is possible to notice that the maximum values are in the central part of the panel, regarding the nodes of the lines C, D, E.

Considering figure 3.10, the highest range of displacement between the maximum and the minimum T_z is equal to 996 µm, along the line C; the lowest range is of 789 µm along line G, i.e. at the bottom edge of the panel as in figure 3.7. Regarding the direction y, figure 3.11 shows a maximum and a minimum displacement range of 746 µm and 604 µm respectively along the columns 11 and 1.

The comparison between methods is provided by the figures D.16, D.17, D.18, D.19, D.20, D.21. The capital letters on the legend refer to the labels described above (figure 3.7). Some possible considerations on these results are listed below.

- T_x: the mean difference value is about 55 µm; the maximum difference is equal to 135 µm. For the majority of points, TEMASE tends to underestimate the actual value. This behaviour is stronger for higher values of translations.

- T_y: in this case, TEMASE seems to overestimate the actual value w.r.t. the manual method. The highest absolute value of the differences is equivalent to 143 µm. The mean difference is about -60 µm.

- T_z: most of values computed with TEMASE are lower than those computed manually. The mean difference is about 86 µm and the maximum discrepancy is of 201 µm.

- R_x: the mean and the maximum difference is respectively 100 µrad and 536 µrad. Also in this case and mainly for the set B, C, D, E, F, the manual method overestimates the actual one.

- R_y, R_z: the mean differences tend to zero because the points are scattered all over the place, below and above zero. R_y shows important differences for higher absolute values of translations; moreover, the differences are consistent with the sign of the horizontal values. The maximum absolute difference is 231 µrad and 242 µrad respectively for R_y and R_z.

– Telescope mock-up

The figures 3.12 and 3.13 show translations and rotations occurring on the telescope. Considering the three rotation components individually, it can be seen that all the nodes rotate solidly according to the same quantity; the value of the component is approximately constant. For example, the mirrors, which define the line of sight, undergo rotations up to about 188 arcsec. The translations have a greater variation, for the same component; for example the values of T_z are between 1011 and 711 µm.

The comparison between methods is provided by the figures D.22, D.23, D.24, D.25, D.26, D.27. Further considerations on these results are listed below.

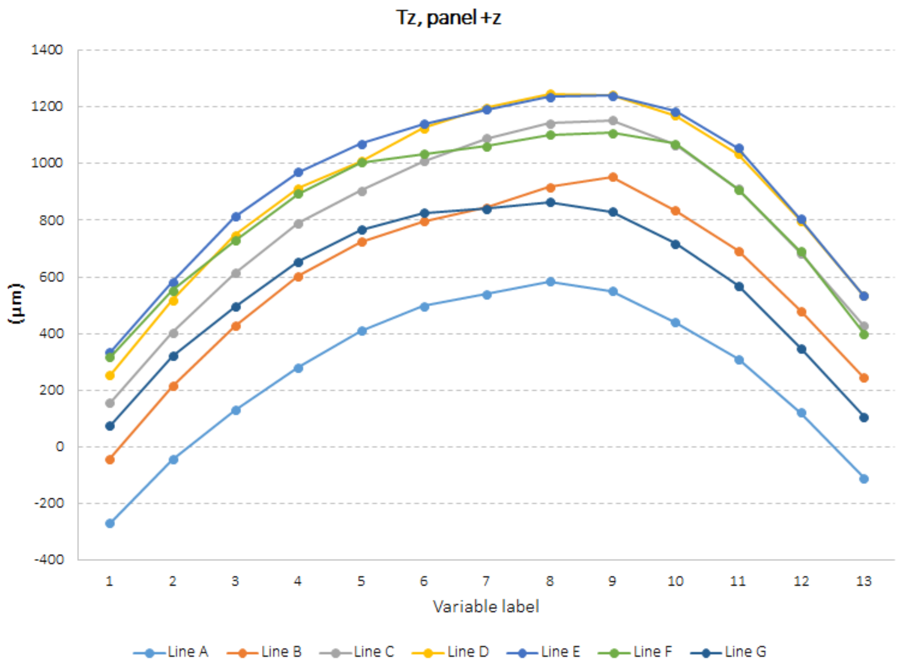

Figure 3.10. Translations T_z on panel +z; recovery nodes lines along direction x (see figure 3.7).

- R_x, R_y, R_z: the differences between the two methods are almost constant, for each component. The mean values of differences are respectively equal to 112 µrad, -101 µrad and 80 µrad.

- T_x, T_y, T_z: the differences variation is more important w.r.t. the rotations one. In T_x and T_y TEMASE presents lower negative values w.r.t. the manual approach. For T_z TEMASE presents lower positive values; thus, the latter approach may underestimate the actual deformations. The mean differences are respectively about: -49 µm, -155 µm and 35 µm.

– ADPM support

This component undergoes zero rotations. It mainly presents translations along the direction z, with values that reach 619 µm. It is emphasised that it is mounted in a very stable area of the main panel. Figure D.28 shows the comparison between methods; also in this case, the differences are concentrated around their average value.

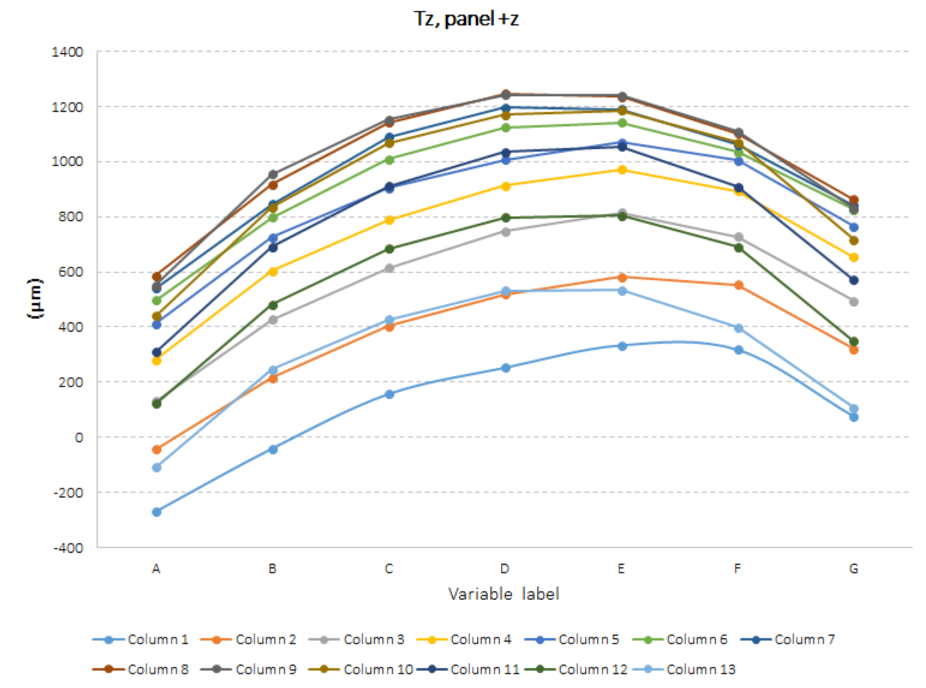

Figure 3.11. Translations T_z on panel +z; recovery nodes columns along direction y (see figure 3.7).

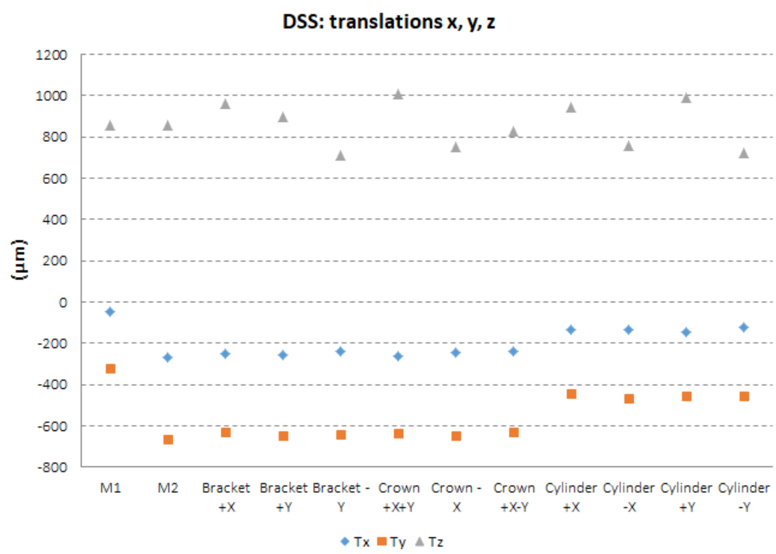

Figure 3.12. Translations on telescope mock-up.

– Composite structure

A detailed visualisation of deformations is presented in the figures D.29, D.30, D.31, D.32, D.33 and D.34. It is possible to notice that each chart shows the recovery

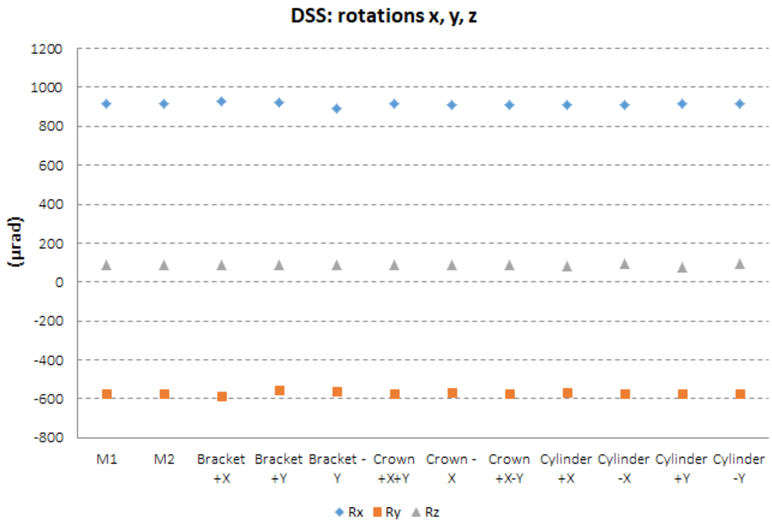

Figure 3.13. Rotations on telescope mock-up.

nodes labels, on the abscissa. The comparison between methods is provided by figures D.35, D.36, D.37, D.38, D.39 and D.40; similar considerations can be made to those made for previous substructures.

The assessed TEMASE algorithm is able to generate instantaneously the Nastran analysis launch files; therefore, the overall procedure exposed in section 3.1.1 can be performed in few hours of work, considering in this time also the finite element analysis. As mentioned previously, in the present study it was also necessary to modify the mathematical models to make them coherent from the point of view of the reference coordinates; however, this inconvenience can happen in industrial practice, precisely because one has to deal with different mathematical modelling environments. In the study described here, the additional functions of the MaREA code were used. Thus, considering all the drawbacks, the matrices [**IM**] and [**Q**] were obtained in less than a week; whereas the manual approach can also take more than 3 weeks.

Chapter 4

Conclusions

In this investigation, the aim was to assess some critical issues which are commonly dealt with in industrial practice when satellite structures are studied from a thermo-elastic point of view. These problems mainly reside:

- in the dissimilarity of the mathematical models, used to perform the thermal and the structural verification, in terms of detail level of continuum mechanics problem discretization and of simulation method assumptions;
- in the temperature data exchange from the TMM to FEM, between different numerical modelling environments;
- in the adequacy of TMM and FEM for thermo-elastic purpose;
- in the level of automation and reliability of approaches to determine the consequent stresses and deformations;
- in the level of generality of one method compared to another and of the software used.

These issues are increasingly urgent to be analysed and mitigated, due to the stability requirements that are becoming increasingly stringent. In the last three decades, the missions objectives have required progressively higher spacecraft performances. As response to these growing needs, the space agencies are paying close attention to research in the thermo-elastic field, in order to improve the current guidelines.

This thesis is a contribution to better address some of the problems mentioned above. Primarily, the attention is focused on the inverse distance weighting algorithm, on the multidisciplinary software MaREA and on the automated procedure to construct an influence matrix.

The study starts with an overview of: main issues affecting the dimensional stability, typical problems that occur during the thermo-elastic stresses and deformations prediction, common temperature mapping methods on the structural model. Section 1.2.4 shows the IDW algorithm working principle, emphasising the role of the parameters k and N and the advantages or disadvantages of this spatial interpolation method.

In chapter 2 the service module of the Euclid program is employed to evaluate the MaREA code and to obtain the thermo-elastic displacements, varying the IDW numerical parameters, the set of recovery structural nodes, the thermal nodal breakdown and the type of thermal loads. The purpose of this exercise is to understand the influence of the latter input on the temperature mapping process.

The results exposed in section 2.2 may support the hypothesis that the possibility of tuning the interpolation parameters, basing on the sampling configuration, is convenient to smooth the discontinuities and to avoid artificial temperature association on the structural model. This combination of findings provides some support for the conceptual premise (section 1.2.4) that an adaptive and more complex IDW method is desirable. However, it is interesting to note that in all the cases, although there is a sensitivity of temperature mapping w.r.t. the k and N variation, the overall influence on deformations of this interpolation parameters tuning exercise is negligible. Therefore, this observation may support the idea that further improvements of a pure spatial interpolation approach, like the IDW, could help to have a slightly better mapping on the structural model, remaining however ineffective in producing very different thermo-elastic results from those obtainable with $N = 1$ or with the discussed approach in section 1.2.1. The latter could be attributable to the fact that the overall range of load discontinuities is irrelevant on the variational formulation [6] of the finite element method. To conclude, it is emphasised that in general a low sensitivity to the used IDW method is present in case of coarse thermal models and, clearly, a pure spatial interpolation is not able to replicate a physical temperature distribution for TMM-B (remark 6), becoming ineffective when the level of detail of the thermal model is very low.

The cases studied in chapter 2 show the most important variation in terms of deformations when the model TMM-B is adopted; comparing the case VII and the case II, the difference between the two situations can reach 70 µm or exceed 100 µrad, for some nodes, and in most cases this discrepancy is greater than 20 microns. In general, it is known that the detail level of TMM mesh is a key aspect of the temperature mapping on the FEM, on the other hand it is underlined that in case of the IDW, and probably for the spatial interpolation, the thermal model influence on results is predominant w.r.t. the temperatures transferring algorithm.

These findings may suggest that in general:

- exceeded a certain threshold of TMM detail, it is not convenient to add complexity to the IDW method;
- for coarse meshes of the TMM, if it is not possible to modify the thermal model for reasons of time and of design, it is useful to integrate the IDW

with a method which considers heat transfer analysis, trying to obtain a more physical distribution of temperatures on the FEM.

In addition, the current context suggests that it is convenient to use the version of the IDW algorithm present in MaREA with $k \geq 4$ and $N = 8$.

This first study was applied to the service module of the Euclid program, so this choice could be a possible limit of the results, being this module a very stable and rigid structure.

Moreover, this exercise shows that the most promising part is the code MaREA, both for the multidisciplinary nature and time saving of its functions, and for the possibility of integrating it with other tools, in the overall design process and into the MATLAB language.

Chapter 3 presents a procedure for pointing stability analysis of satellite structure. The approach consists in the construction of an influence matrix, containing local mechanical deformations and performance contributions on the FEM, applying unitary thermal loads of 1 °C. Once the IM is generated, thanks to the linearity hypothesis, a matrix $[\mathbf{Q}]$ with the actual structural deformations is obtained, according to the linear relation $[\mathbf{Q}] = [\mathbf{IM}][\mathbf{TM}]$ (see section 3.1). Basically, this procedure is useful with several temperature data set (i.e. transient analysis) since it allows a considerable time saving. This procedure is applied to the IRIDIUM NEXT platform and two methods to obtain the IM and the structural deformations are compared; it is considered an approach with a low level of automation, which can be considered manual, and an almost totally automated approach, called TEMASE.

The study exposed in chapter 3 showed a remarkable difference between the manual and the TEMASE method, in terms of procedure automation and of writing and verification time of the Nastran launch files. Indeed, the latter are generated instantaneously by TEMASE and the overall procedure can be performed in a few hours of work, considering at this time also the finite element analysis. In addition, it was also necessary to modify the mathematical models to make them coherent from the point of view of the reference coordinates; this inconvenience can happen in industrial practice because of the different mathematical modelling environments. In this phase some of the additional MaREA functions were used. Thus, despite all the drawbacks, the matrices $[\mathbf{IM}]$ and $[\mathbf{Q}]$ were obtained in less than a week, while the manual approach can also take more than 3 weeks.

The results of section 3.2.3 also showed that the extent of differences between the aforementioned methods is on average between a few tens and two hundred units, both for translations and rotations. Considering the absolute values of the differences and calling the generic difference of translation and of rotation respectively T and R, it occurs that:

- for the panel +z, in 58% of translations $50\text{µm} \leq T \leq 200\text{µm}$ and also in about 58% of rotations $50\text{µrad} \leq R \leq 200\text{µrad}$, moreover only a value exceeds the

200µm and only for the 8% of rotations is higher than 200µrad;

- for the subsystems, the 85% of translations indicates that 50µm $\leq T \leq$ 200µm and the 66% of rotations shows that 50µrad $\leq R \leq$ 200µrad, moreover the remaining percentages fall below 50 units.

In addition the extent of deformations, both according to a positive or a negative axis direction, is detectable by distortion measurement systems, during the testing configuration; for example, more than the 90% of mechanical nodes translations are $\geq$ 10µm. It is unfortunate that the study did not include a comparison with experimental data, so the experimental validation campaign, currently underway, could solve this lack.

Once again, the key strength of this automated approach is the time saving and the possibility to make geometric changes to the models, in the MATLAB environment, and to easily modify the IM, if it is necessary to change the number of thermal zones. On the contrary, with the manual approach, the modification of the influence matrix requires considerable effort.

Further research on MaREA might explore the possibility to introduce, in the actual transfer algorithms, an automatic recognition of contiguous structural nodes belonging to different components of the primary or secondary structure. Thereby, it is possible to overcome the second drawback exposed in remark 3, resulting in a further time saving of the thermo-elastic study. Finally, for a better and quicker learning of the general functioning of the MaREA code, it is recommended to enrich the manual with examples and tutorials that can be used by any user outside the industrial environment of the developers.

Bibliography

[1] ECSS-E-HB-32-26 working group. Space engineering – spacecraft mechanical loads analysis handbook. Standards, ECSS, February 2013.

[2] Miguel A. Aguirre. *Introduction to Space Systems: Design and Synthesis.* Springer, 2013.

[3] Eloi Ferrer, Luisa Buinhas, and Roger Förstner. System design and thermal stability analysis for the irassi infrared space interferometer – aiaa space 2016. In *AIAA SPACE Forum*, Long Beach, California, 13 - 16 September 2016. American Institute of Aeronautics and Astronautics (AIAA).

[4] Menno Koot, Simon Appel, and Samo Simonian. Temperature mapping for structural thermo-elastic analyses – mehod benchmarking. Presented at the ECSSMET 2018, ESTEC, Noordwijk, The Netherlands.

[5] James Etchells. Integrating finite element analysis into the spacecraft thermal analysis process. Technical note, ESA, July 2005.

[6] O.C. Zienkiewicz, R.L. Taylor, and J.Z. Zhu. *The Finite Element Method: Its Basis and Fundamentals.* Butterworth-Heinemann – Elsevier, 2013.

[7] I. S. Sokolnikoff. *Mathematical theory of elasticity.* McGraw-Hill, second edition, 1956.

[8] MSC Software Corporation. *MSC Nastran – Reference guide*, 2018.

[9] S. de Zotti, J.-M. Lome, J.-L. Parquet, and C. Lemcke. Thermo-mechanical verification techniques. In *European Conference on Spacecraft Structures – Materials and Mechanical Testing*, page 359, ESTEC – Noordwijk, Netherlands, 2001. European Space Agency.

[10] MSC Software Corporation. *MSC Nastran – Quick reference guide*, 2018.

[11] MSC Software Corporation. *MSC Nastran – Linear Static Analysis User's Guide*, 2018.

[12] Donald Shepard. A two-dimensional interpolation function for irregularly-spaced data. In *Proceedings of 23rd National Conference, Association for Computing Machinery*, pages 517–524. Laboratory for Computer Graphics, Harvard University, 1968.

[13] Lixin Li, Travis Losser, Charles Yorke, and Reinhard Piltner. Fast inverse distance weighting-based spatiotemporal interpolation: A web-based application

of interpolating daily fine particulate matter pm2:5 in the contiguous u.s. using parallel programming and k-d tree. *International Journal of Environmental Research and Public Health*, 11:9101–9141, 2014.

[14] Jeroen A.S. Witteveen and Hester Bijl. Explicit mesh deformation using inverse distance weighting interpolation. In *19th AIAA Computational Fluid Dynamics*, volume Fluid Dynamics and Co-located Conferences, San Antonio, Texas, 2009. AIAA.

[15] George Y. Lu and David W. Wong. An adaptive inverse-distance weighting spatial interpolation technique. *Computers & Geosciences*, 34:1044– 1055, 2008.

[16] Louis de Mesnard. Pollution models and inverse distance weighting: some critical remarks. *Computers & Geosciences*, 52:459–469, 2013.

[17] Zhanglin Li and Ping Wang. Intelligent optimization on power values for inverse distance weighting. In *2013 International Conference on Information Science and Cloud Computing Companion*, pages 370–375, Guangzhou, China, 7-8 Dec. 2013. IEEE.

[18] W. R. Tobler. A computer movie simulating urban growth in the detroit region. *Economic Geography*, 46:234–240, 1970.

[19] Zimmerman D., Pavlik C., Ruggles A., and Armstrong M.P. An experimental comparison of ordinary and universal kriging and inverse distance weighting. *Mathematical Geology*, 31(4):375–390, 1999.

[20] Komahan Boopathy and Markus P. Rumpfkeil. A multivariate interpolation and regression enhanced kriging surrogate model. In *21st AIAA Computational Fluid Dynamics Conference*, volume Fluid Dynamics and Co-located Conferences, San Diego, CA, June 24-27 2013. AIAA.

[21] Jef H., Clemens M., Gerwin D., and Frans F. Spatial interpolation of ambient ozone concentrations from sparse monitoring points in belgium. *Journal of Environmental Monitoring*, 8:1129–1135, 2006.

[22] Mareschi V. MaREA – user manual. Unpublished document, Thales Alenia Space Italy, May 2018.

[23] David G. Gilmore. *Spacecraft Thermal Control Handbook: Fundamental Technologies*, volume 1. The Aerospace Corporation, 2 edition, 2002.

[24] Tecplot, Inc., Bellevue, WA. *Tecplot 360 – User's Manual*, 2008. Release 2.

[25] Marie Bourdeaud'hui, John Ponsy, Sébastien Laborde, and Philippe Corberand. Designing satellites from the main thermo-elastic stability contributors quantification – process and tool applied on juice.

[26] John M. Chambers, William S. Cleveland, Beat Kleiner, and Paul A. Tukey. *Graphical methods for data analysis.* CRC Press, 2018.

Appendices

Appendix A

Structural model details images

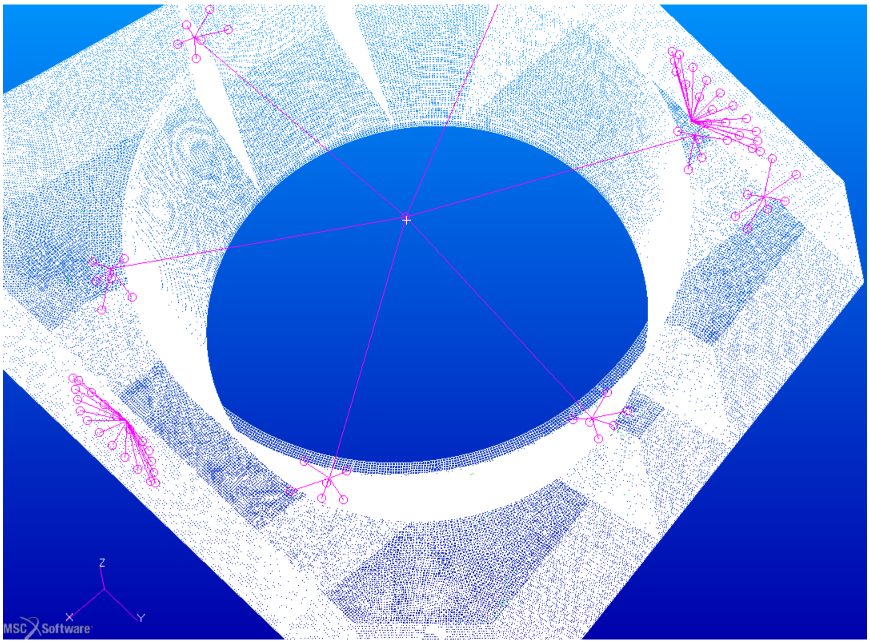

Figure A.1. FEM internal details.

Figure A.2. Panel +z.

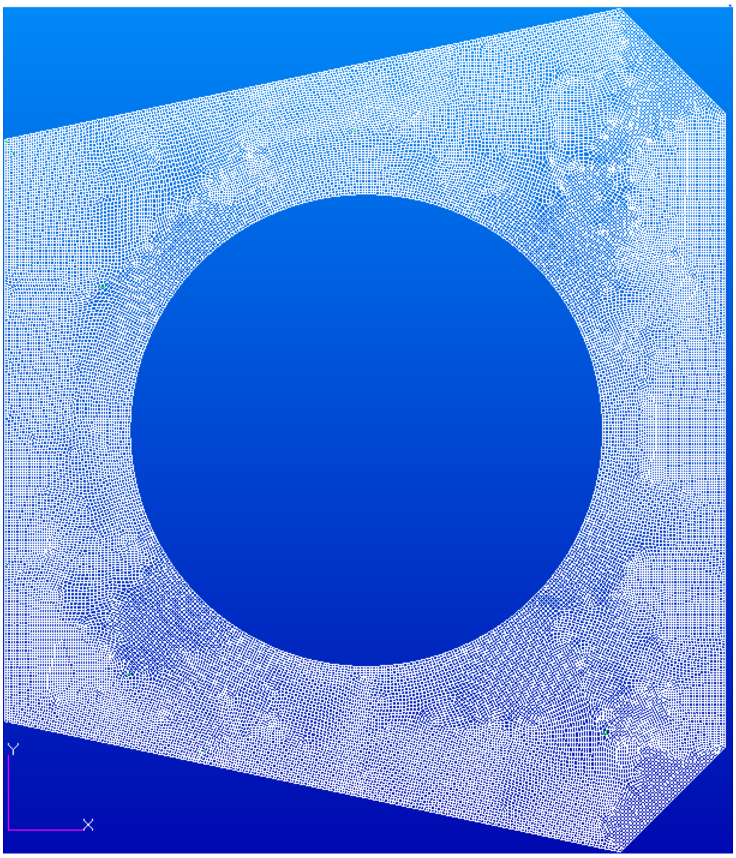

Figure A.3. Panel -z.

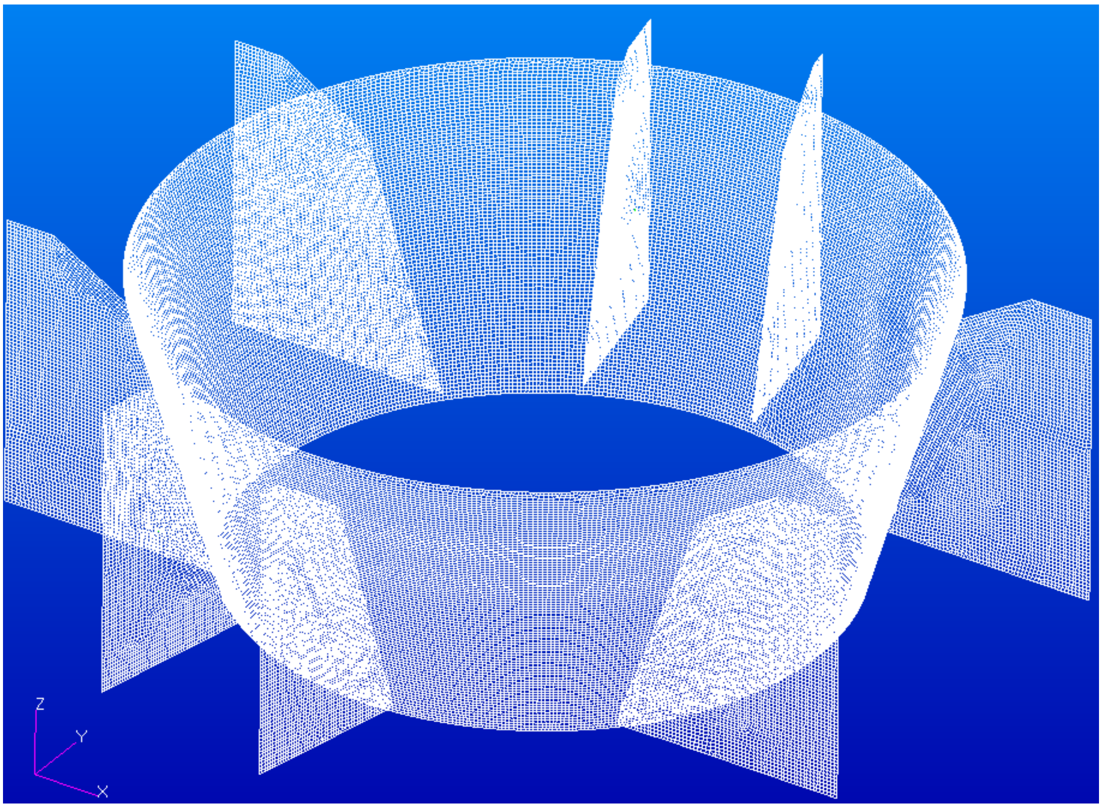

Figure A.4. Central cone and shear webs.

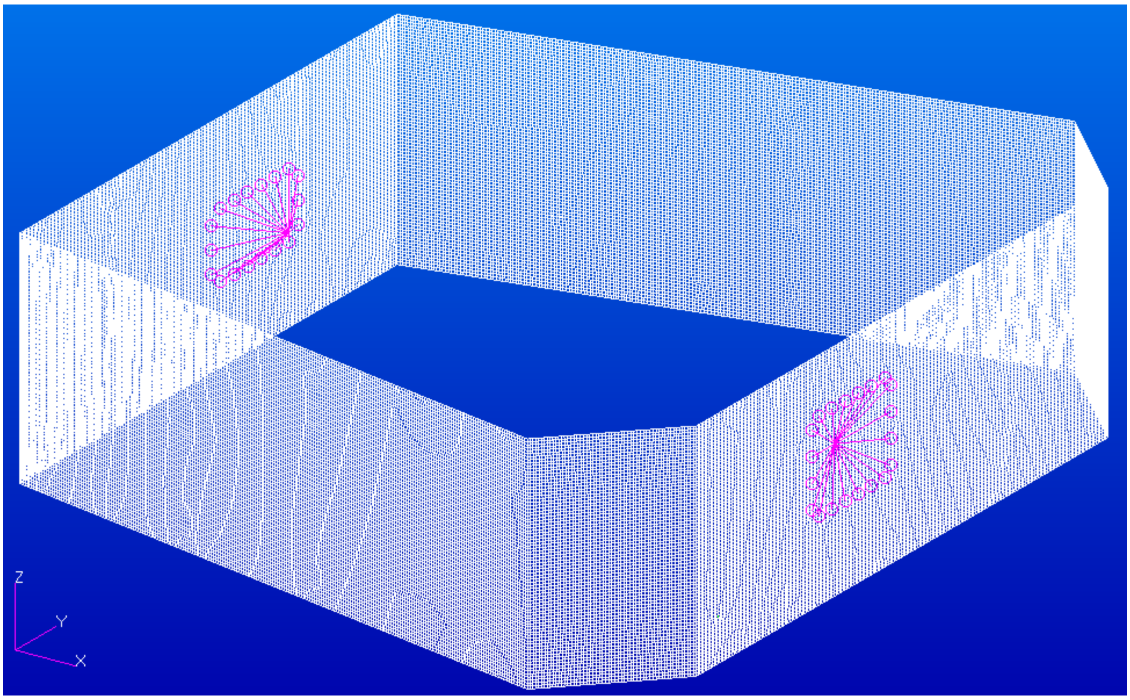

Figure A.5. Lateral panels and equipment boxes models.

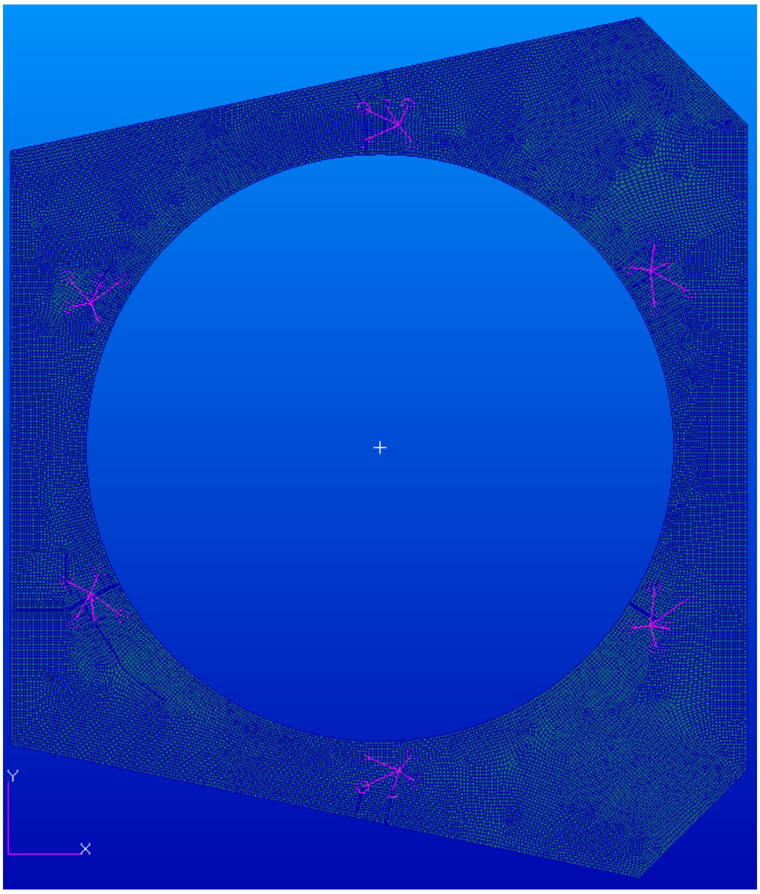

Figure A.6. Upper platform and six connections.

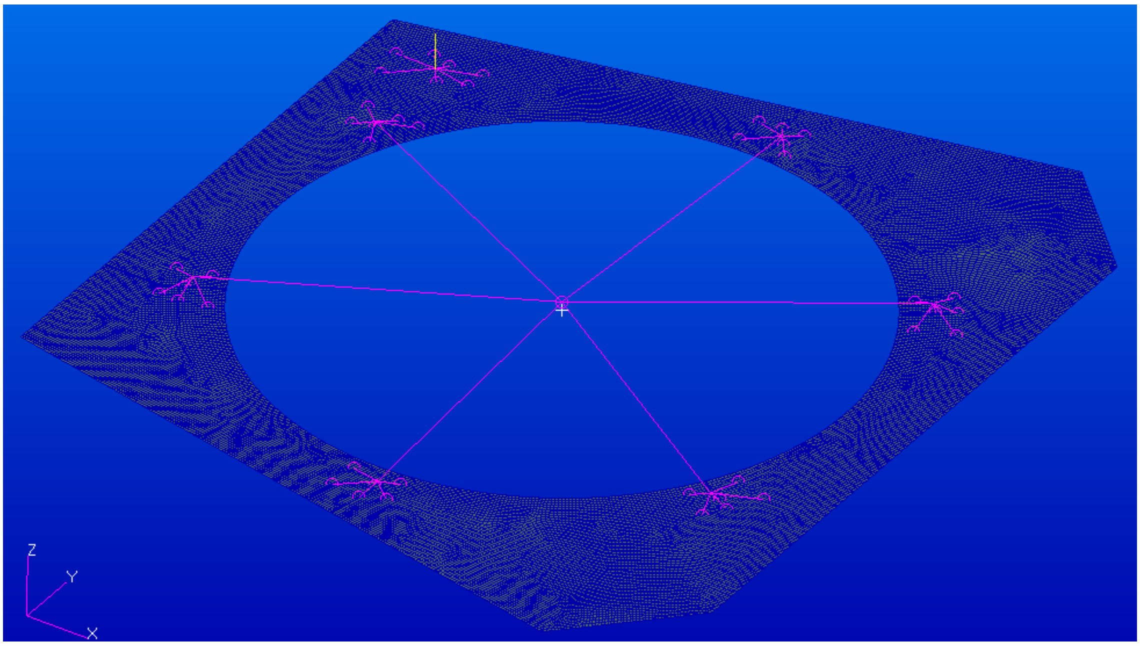

Figure A.7. Upper platform, rigid connections and star tracker.

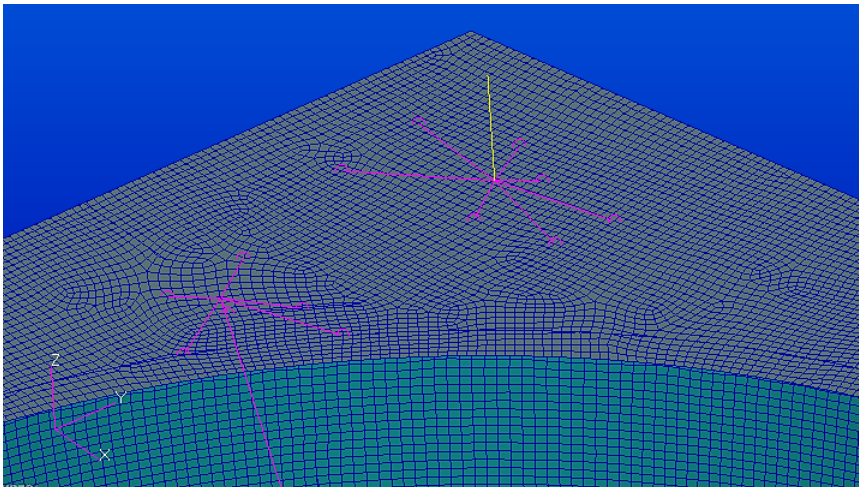

Figure A.8. Detail of star tracker model.

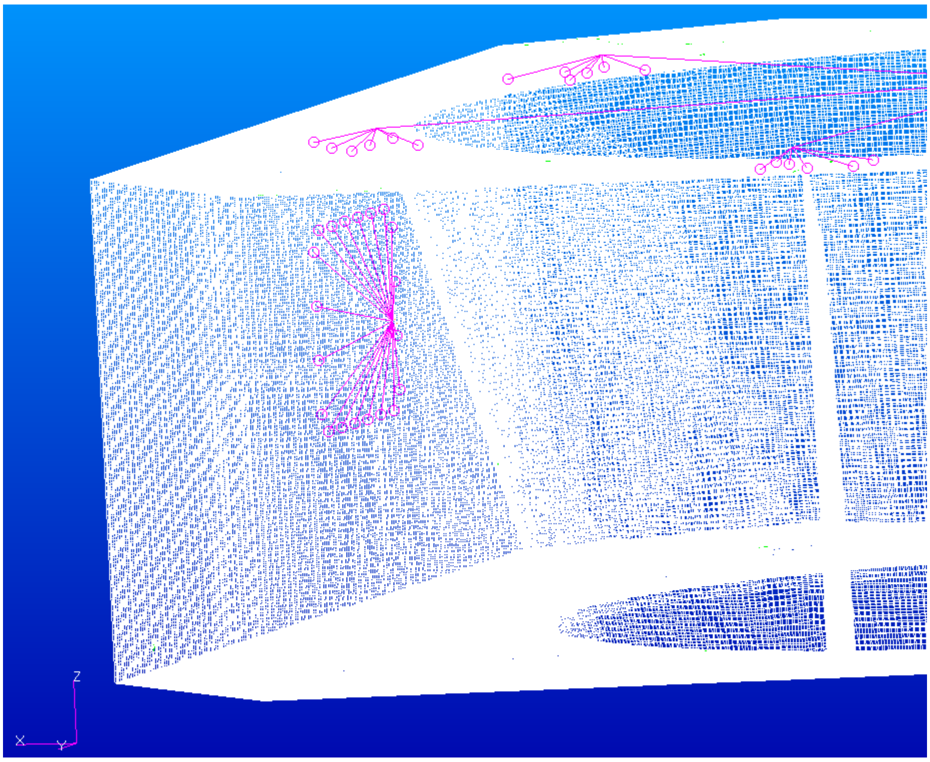

Figure A.9. Detail of equipment box model.

Appendix B

Euclid temperature mapping

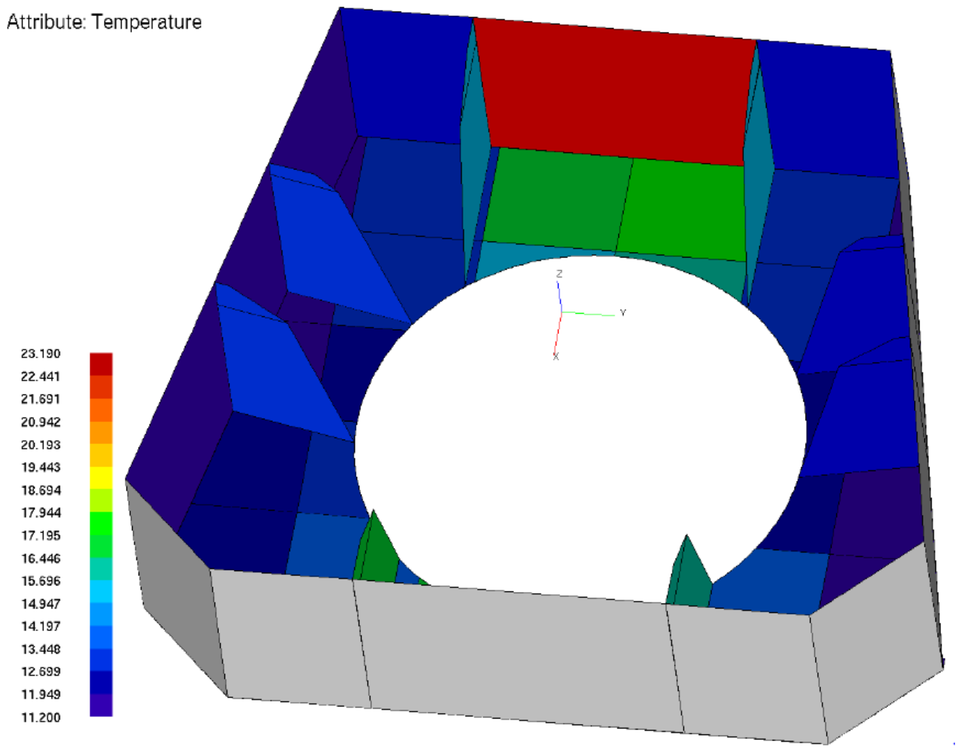

Figure B.1. Coarse TMM nodal breakdown and temperature map (+x view); $[T]$ = °C.

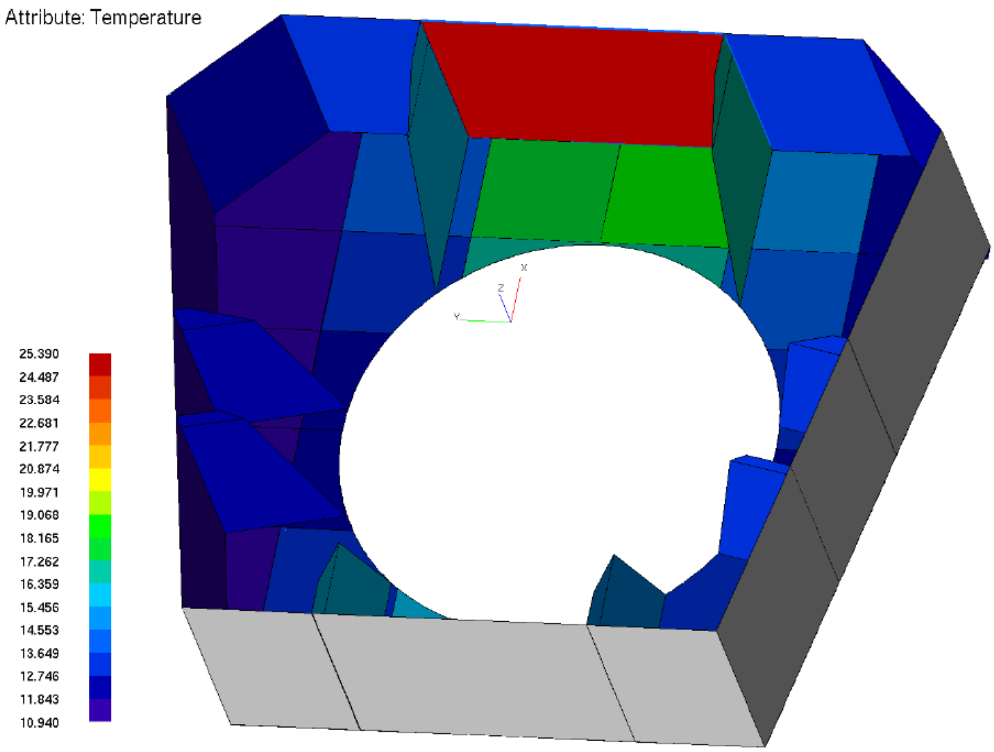

Figure B.2. Coarse TMM nodal breakdown and temperature map (-x view); $[T]$ = °C.

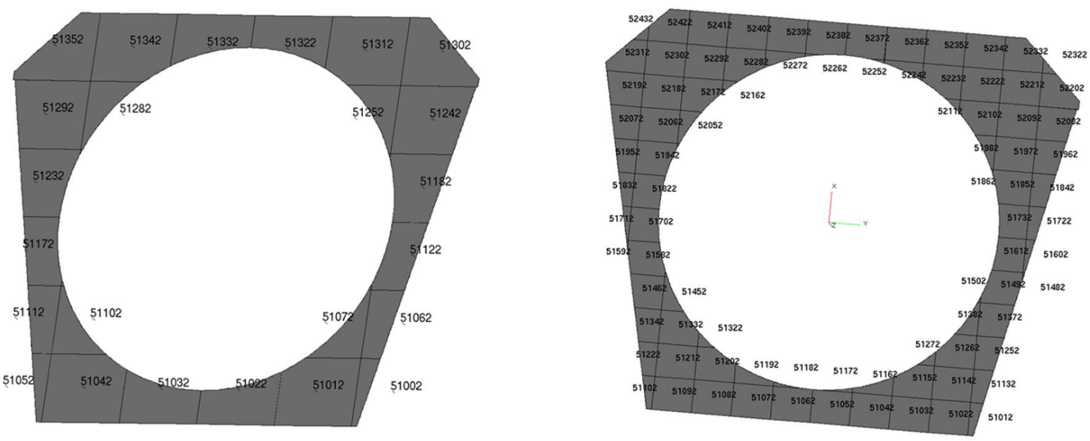

Figure B.3. Panel +z nodal breakdown; coarse TMM on the left, related to the second described thermal model.

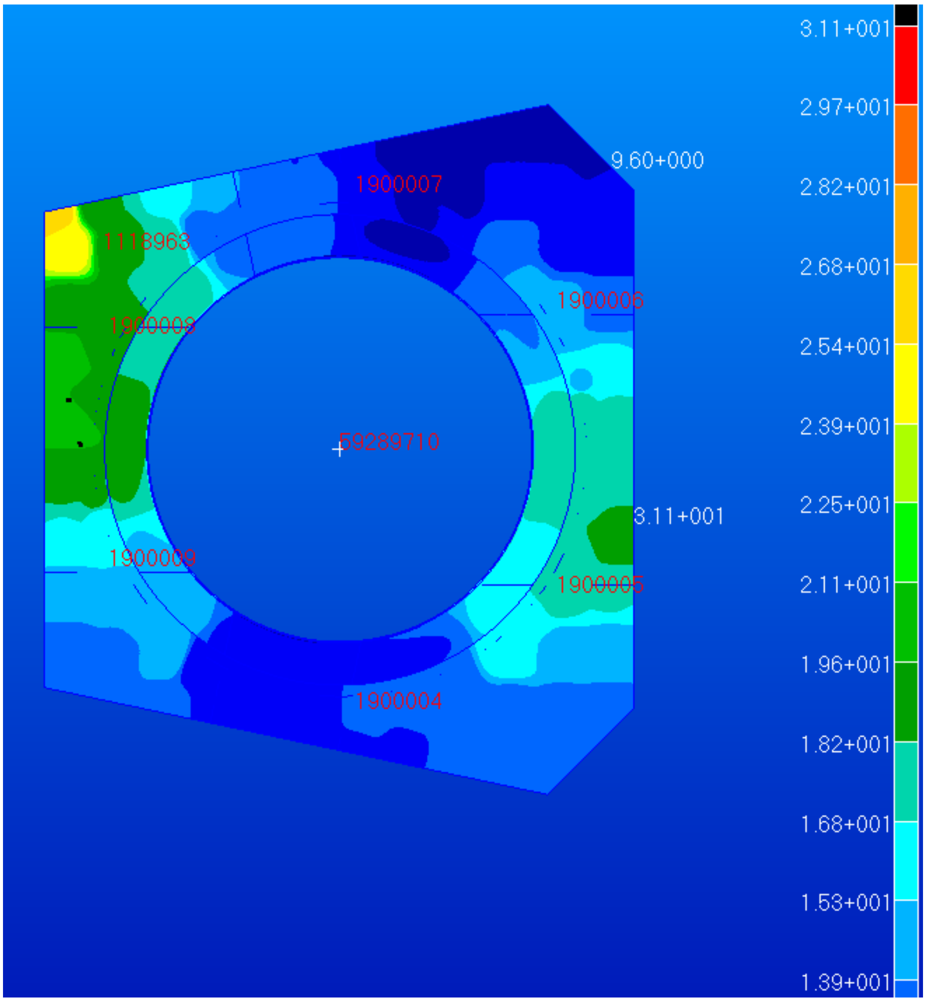

Figure B.4. ID numbers and temperature field for the first set of recovery nodes on +z panel.

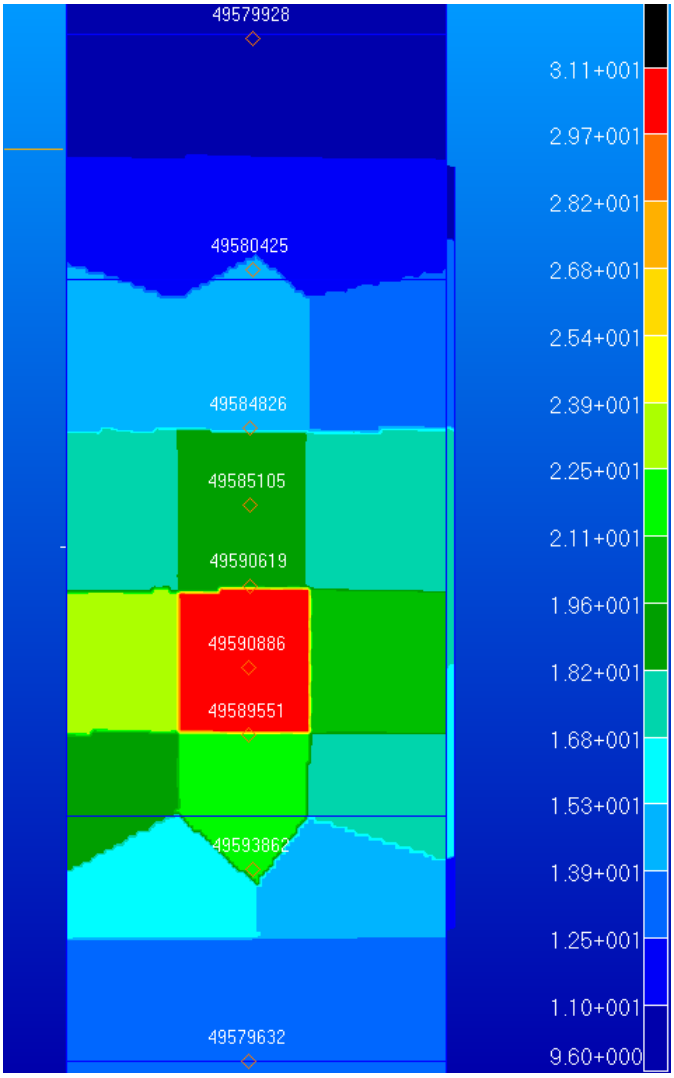

Figure B.5. ID numbers and temperature field for the second set of recovery nodes on the lateral panel.

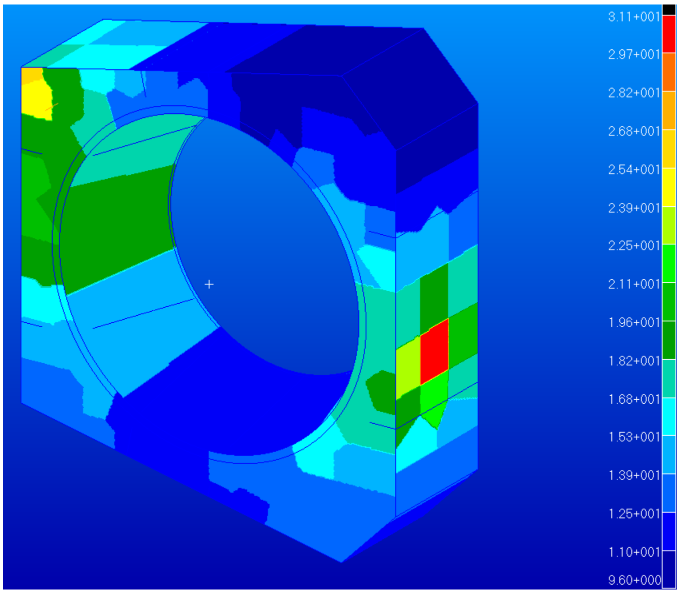

Figure B.6. Temperature field for the reference case ($N = 1$), +z view; $[T] = °\mathrm{C}$.

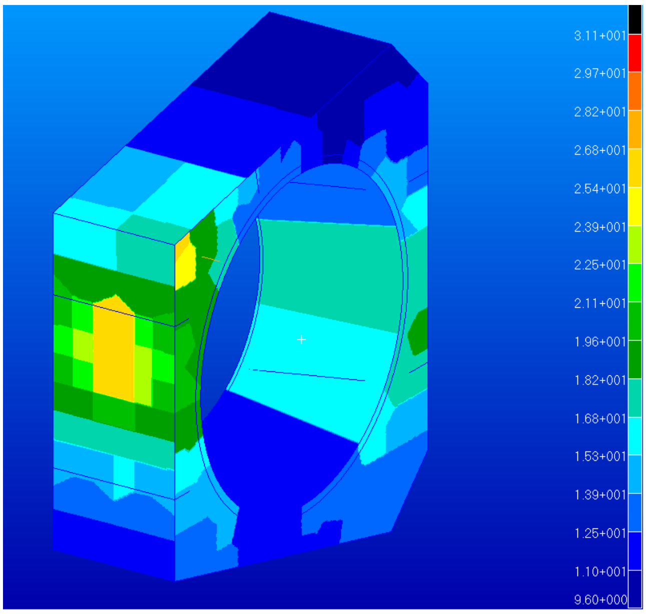

Figure B.7. Temperature field for the reference case ($N = 1$), -z view; $[T] = °\mathrm{C}$.

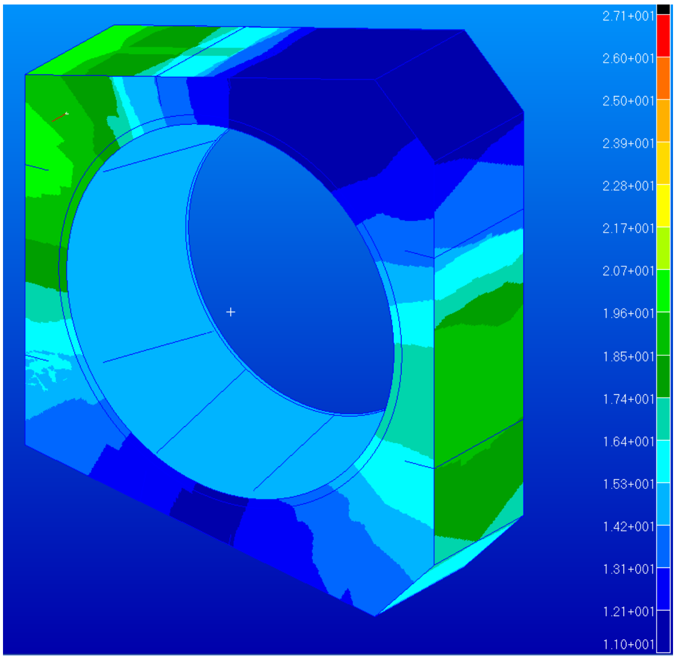

Figure B.8. Temperature field for $N = 12$ and $k = 0$; $[T] = °\mathrm{C}$.

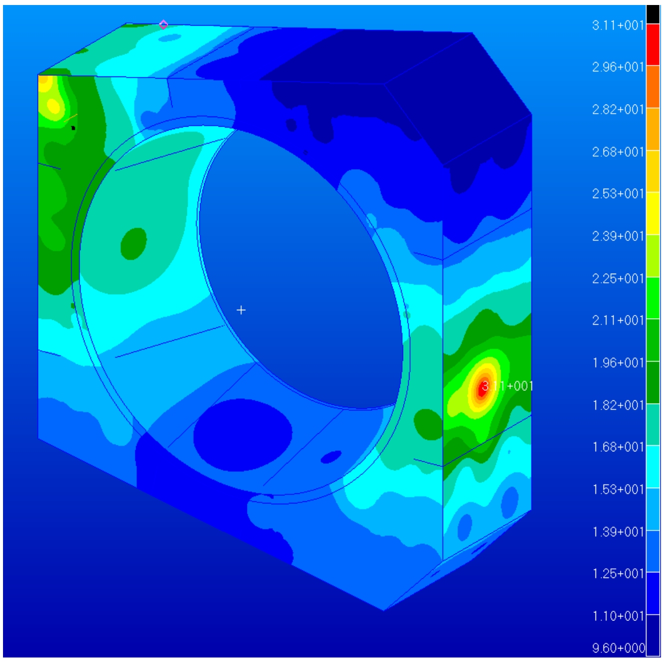

Figure B.9. Temperature field for $N = 12$ and $k = 1$; $[T] = °\mathrm{C}$.

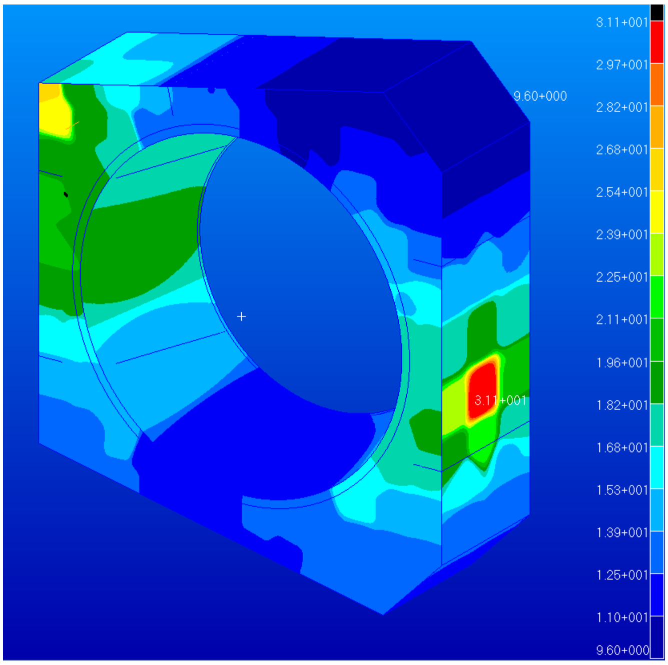

Figure B.10. Temperature field for $N = 12$ and $k = 4$; $[T] = °C$.

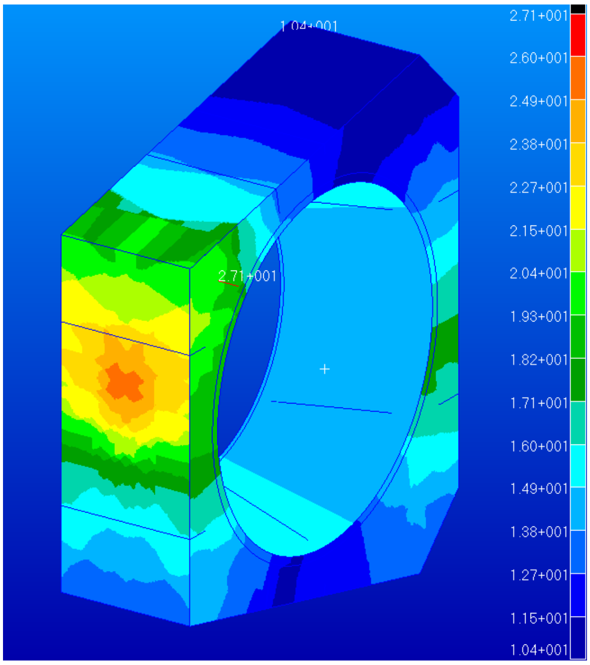

Figure B.11. Temperature field for $N = 8$ and $k = 0$, -z view; $[T] = °C$.

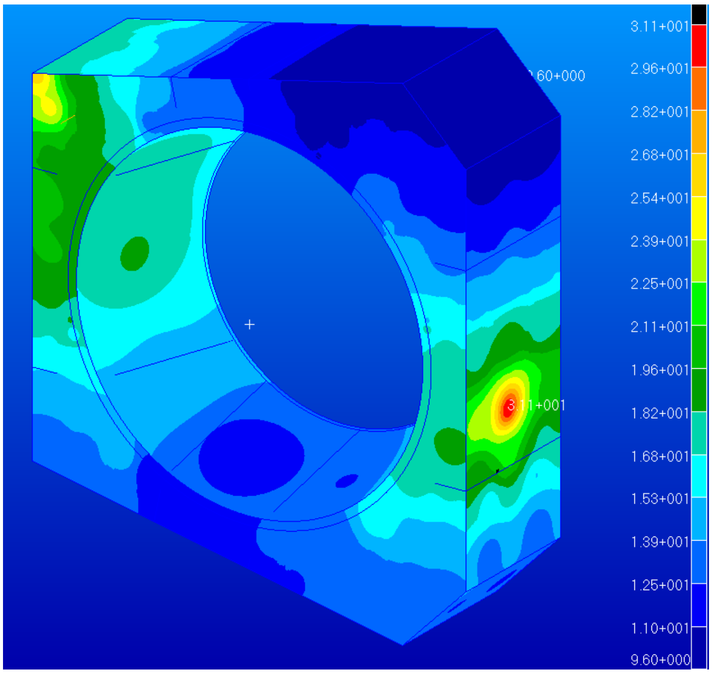

Figure B.12. Temperature field for $N = 8$ and $k = 1$, +z view; $[T] = °C$.

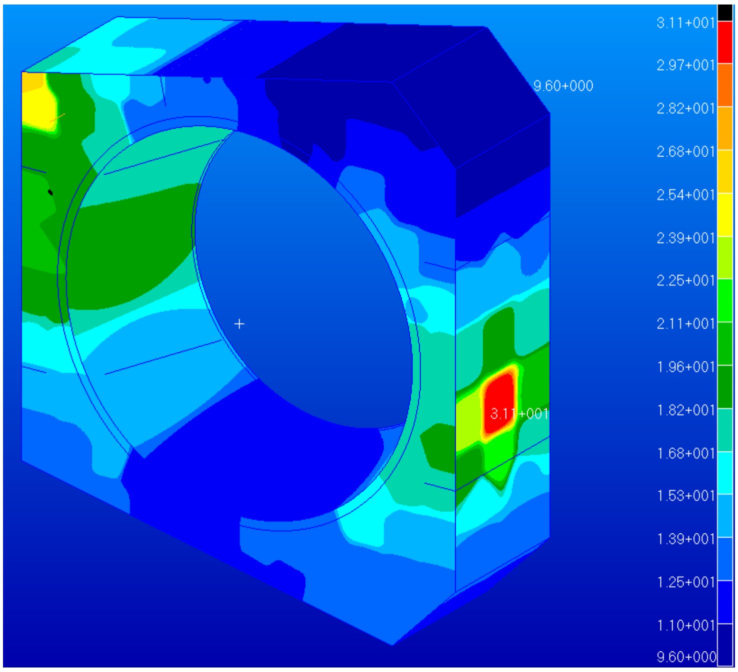

Figure B.13. Temperature field for $N = 8$ and $k = 4$, +z view; $[T] = °C$.

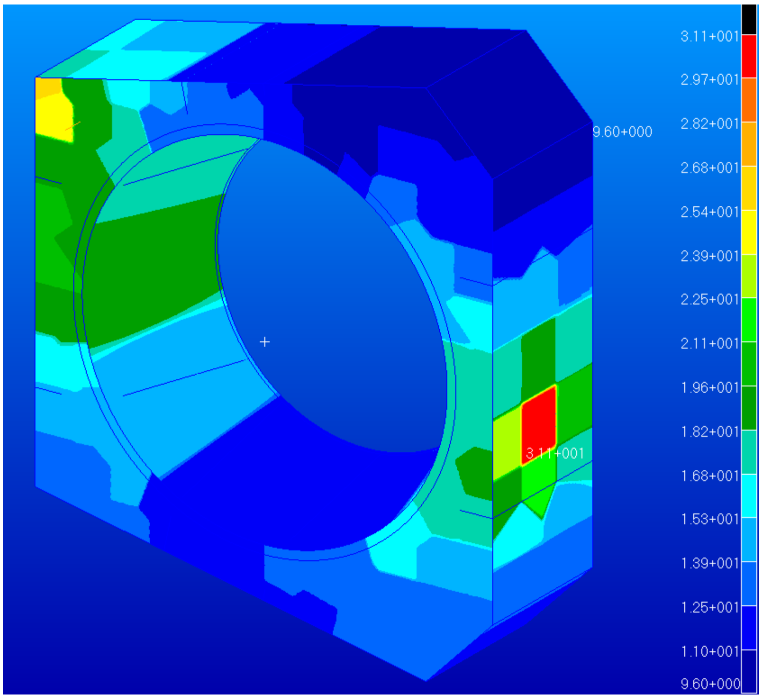

Figure B.14. Temperature field for $N = 8$ and $k = 16$, +z view; $[T] = °C$.

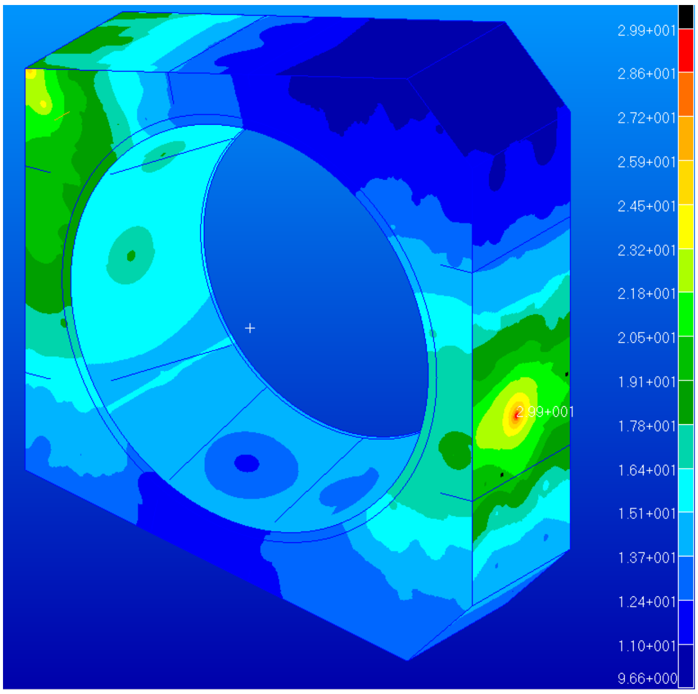

Figure B.15. Temperature field for $N = 8$ and $k = 0.5$, +z view; $[T] = °C$.

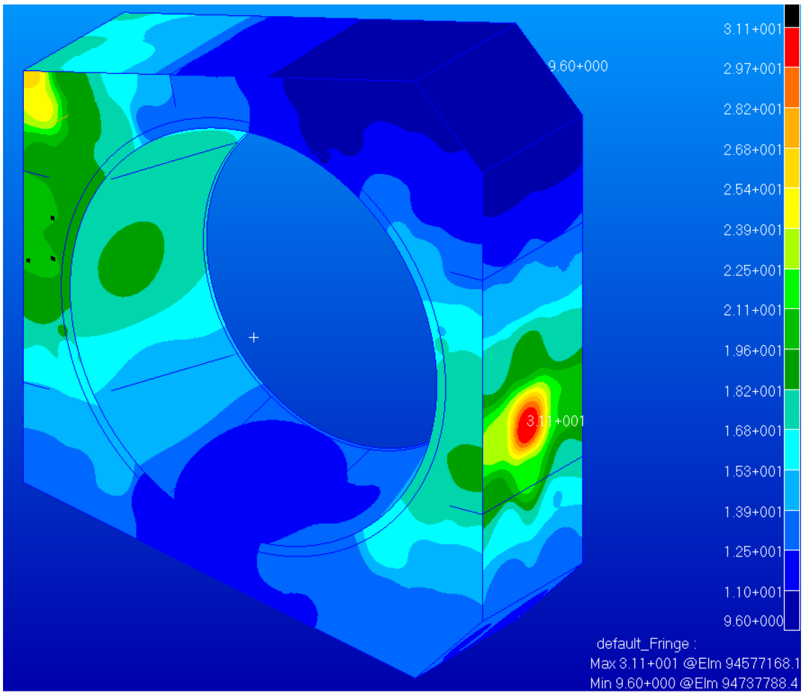

Figure B.16. Temperature field for $N = 8$ and $k = 1.5$, +z view; $[T] = °\mathrm{C}$.

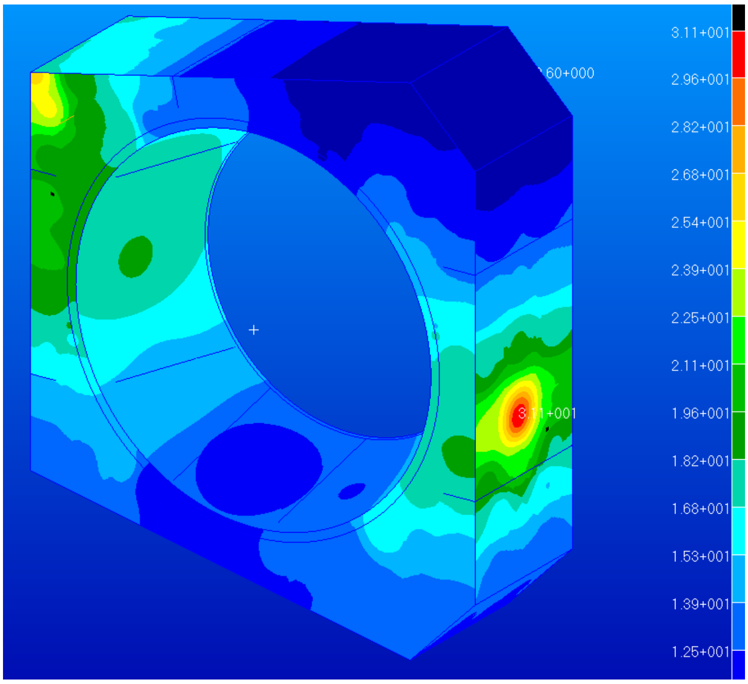

Figure B.17. Temperature field for $N = 5$ and $k = 1$, +z view; $[T] = °\mathrm{C}$.

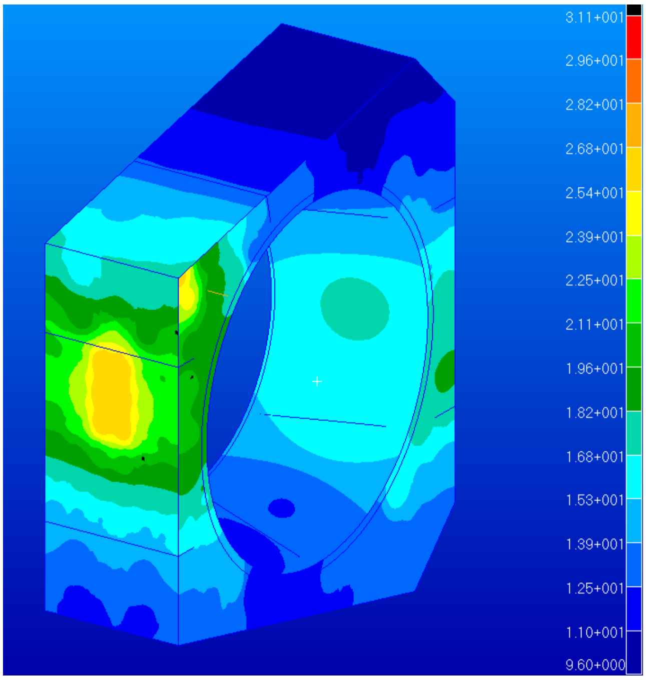

Figure B.18. Temperature field for $N = 5$ and $k = 1$, -z view; $[T] = °C$.

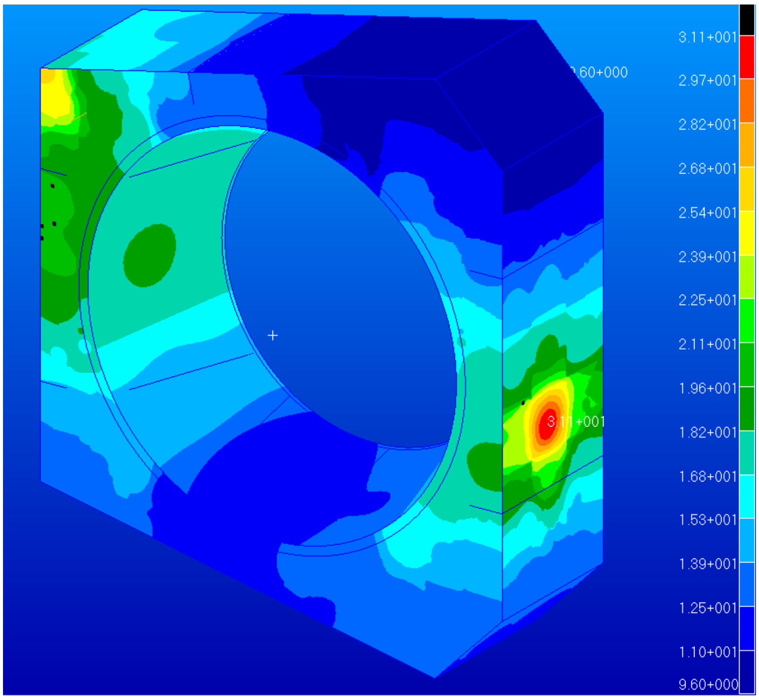

Figure B.19. Temperature field for $N = 3$ and $k = 1$, +z view; $[T] = °C$.

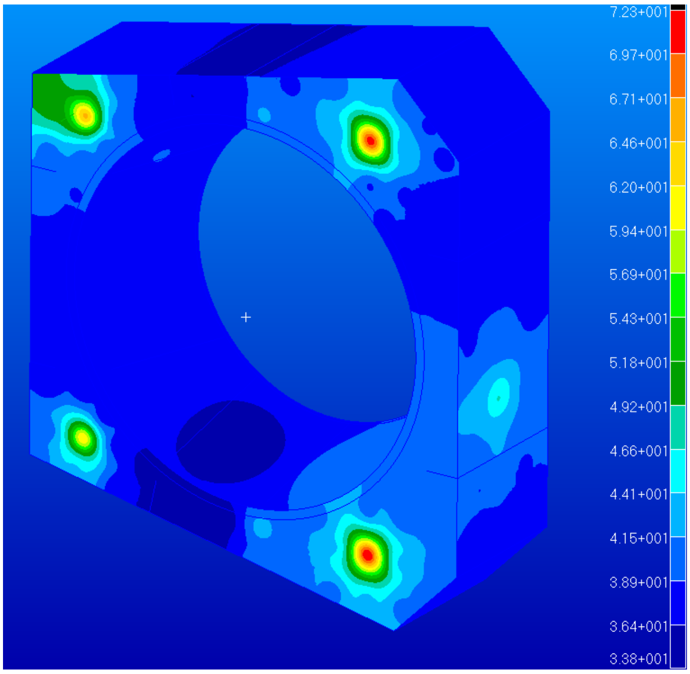

Figure B.20. Temperature field for case VI and $k = 1$, +z view; $[T] = °C$.

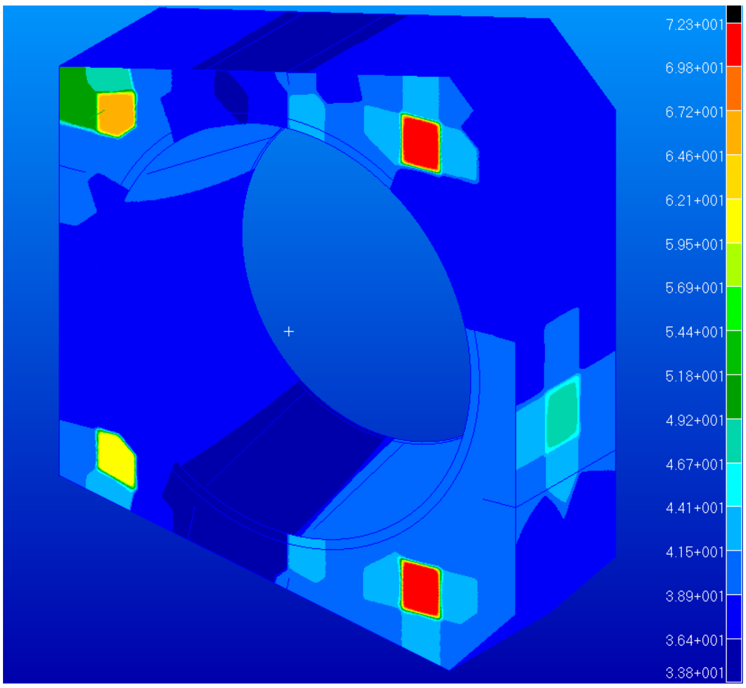

Figure B.21. Temperature field for case VI and $k = 5$, +z view; $[T] = °C$.

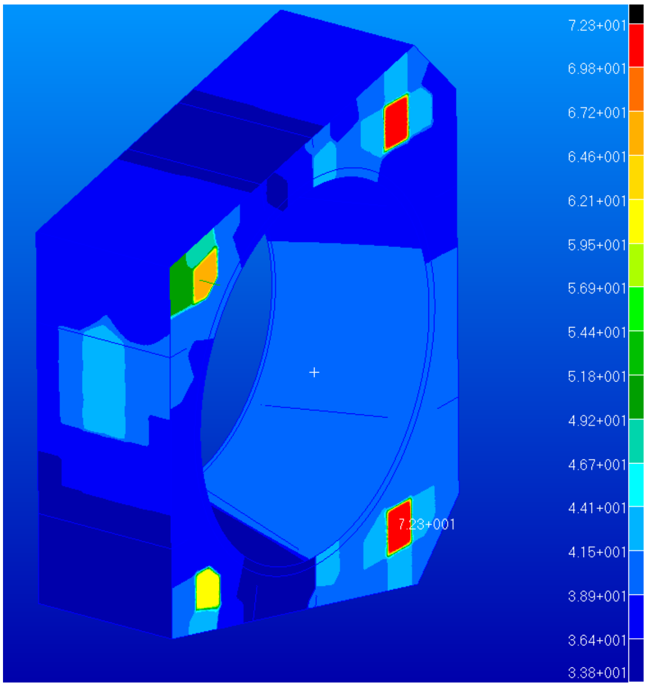

Figure B.22. Temperature field for case VI and $k = 5$, later panel view; $[T] = °C$.

Appendix C

Euclid thermo-elastic analysis

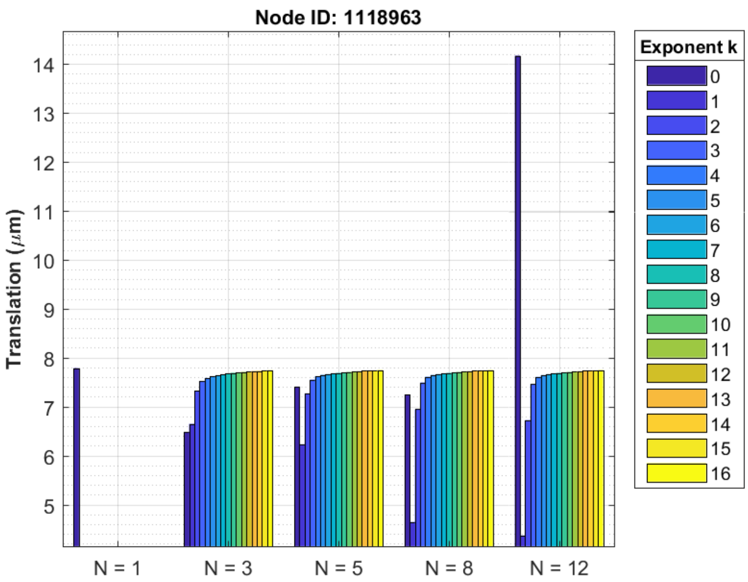

Figure C.1. Translations comparison for node 1118963.

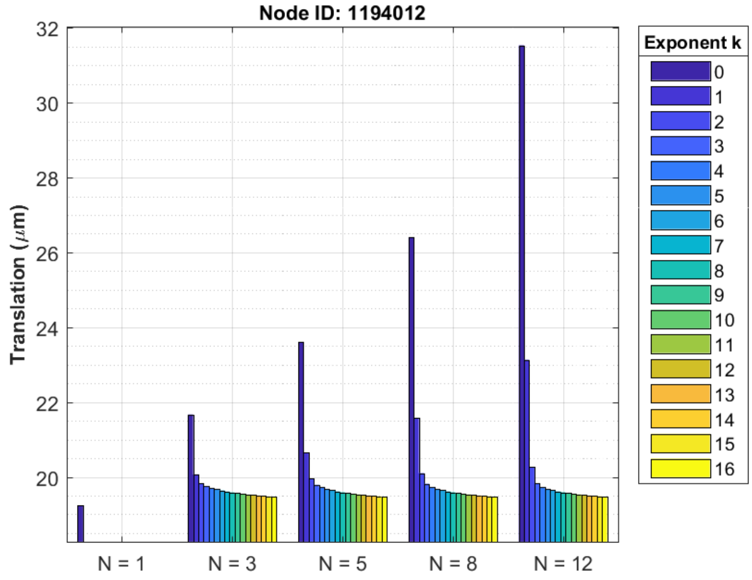

Figure C.2. Translations comparison for node 1194012.

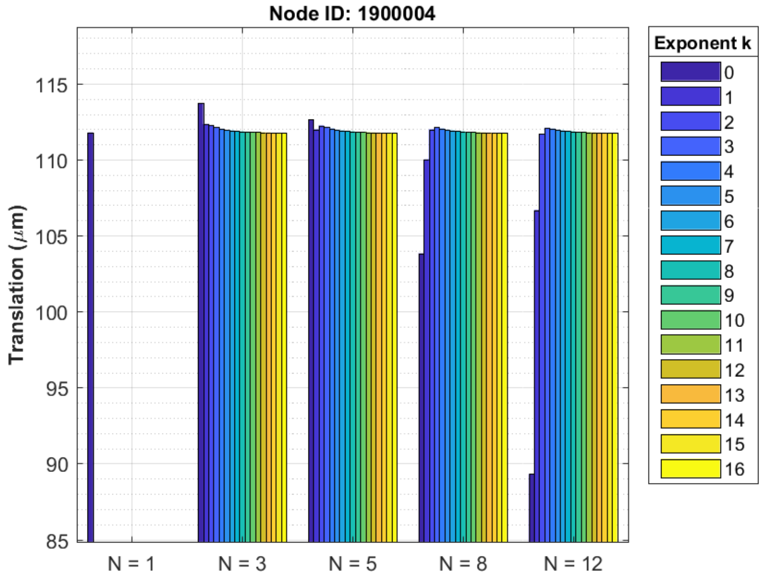

Figure C.3. Translations comparison for node 1900004.

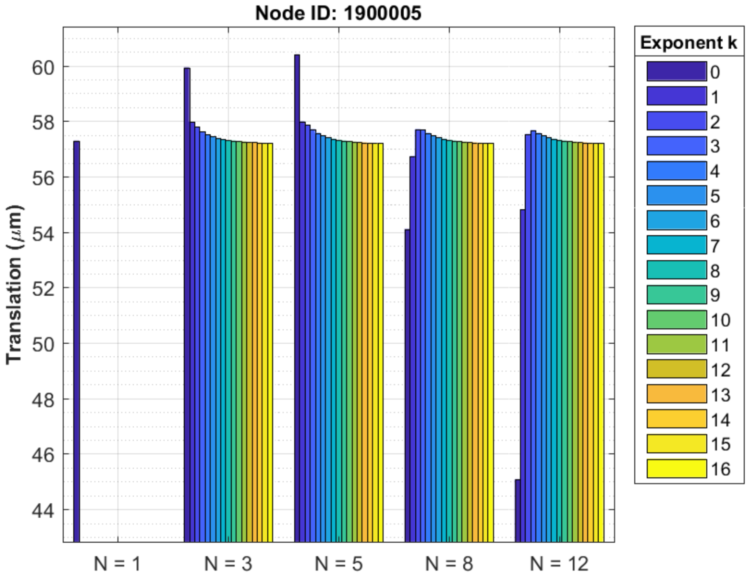

Figure C.4. Translations comparison for node 1900005.

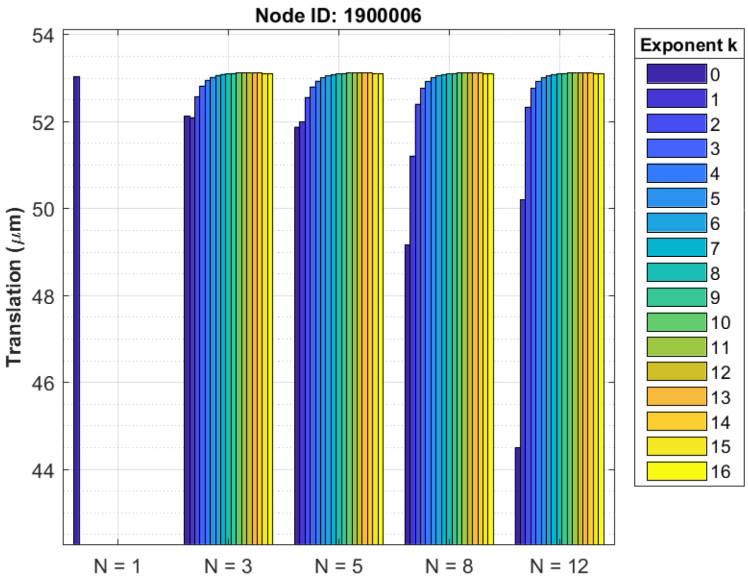

Figure C.5. Translations comparison for node 1900006.

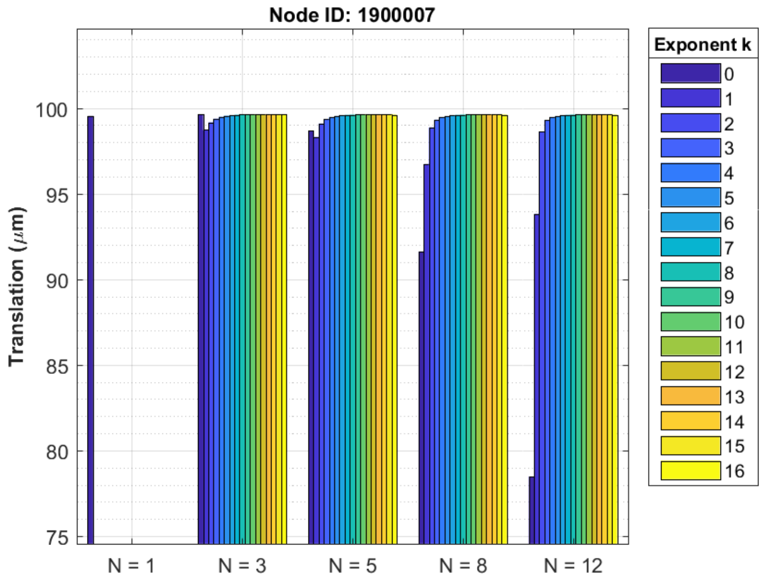

Figure C.6. Translations comparison for node 1900007.

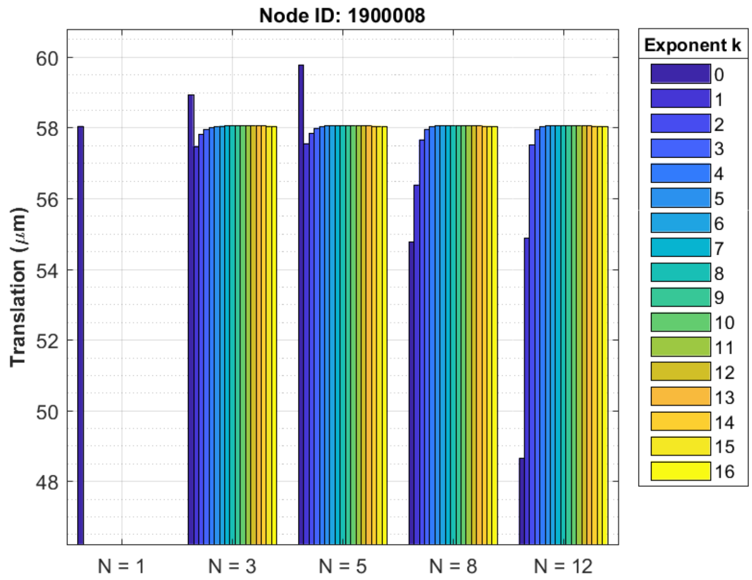

Figure C.7. Translations comparison for node 1900008.

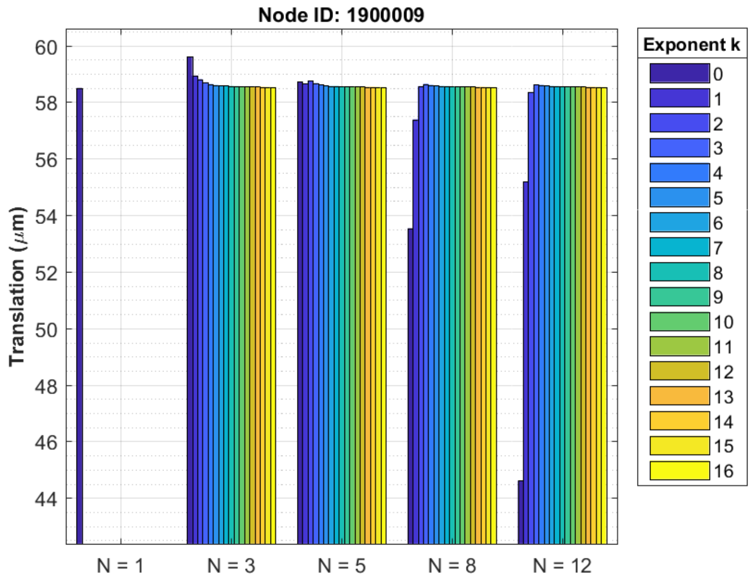

Figure C.8. Translations comparison for node 1900009.

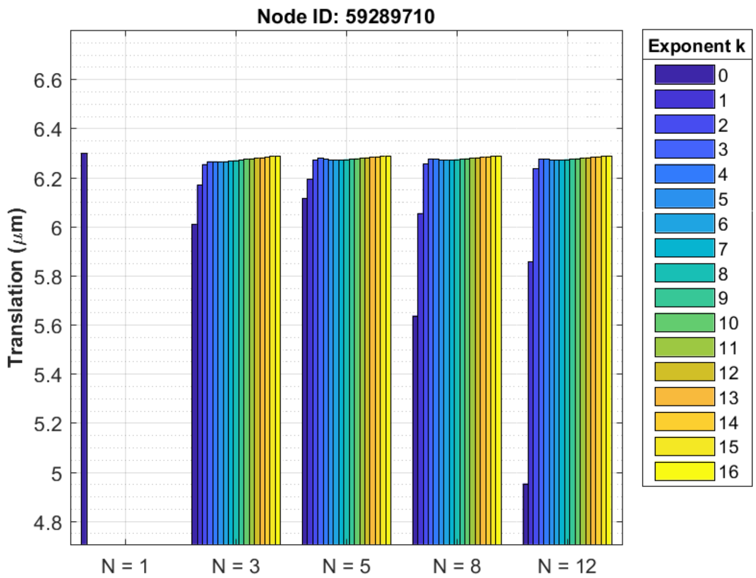

Figure C.9. Translations comparison for node 59289710.

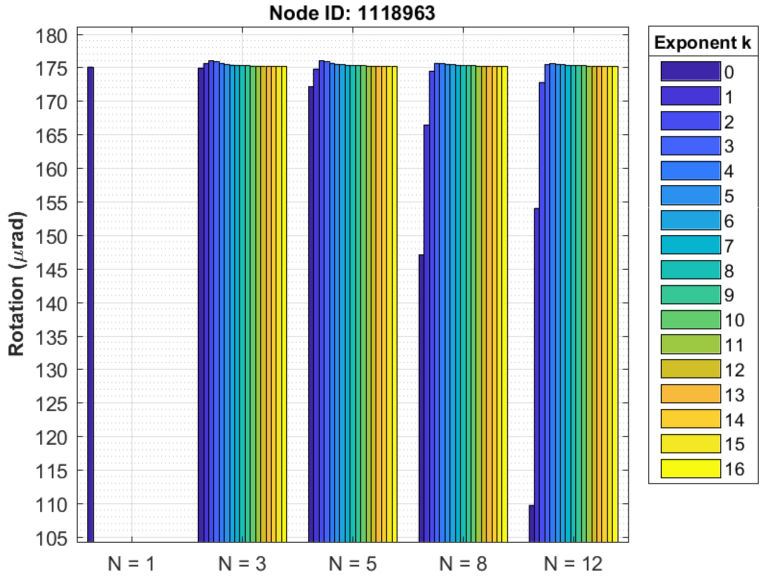

Figure C.10. Rotations comparison for node 1118963.

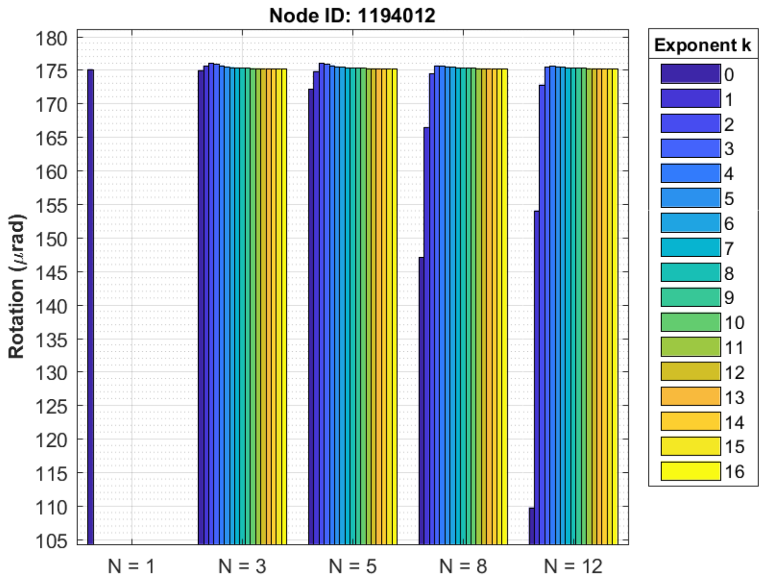

Figure C.11. Rotations comparison for node 1194012.

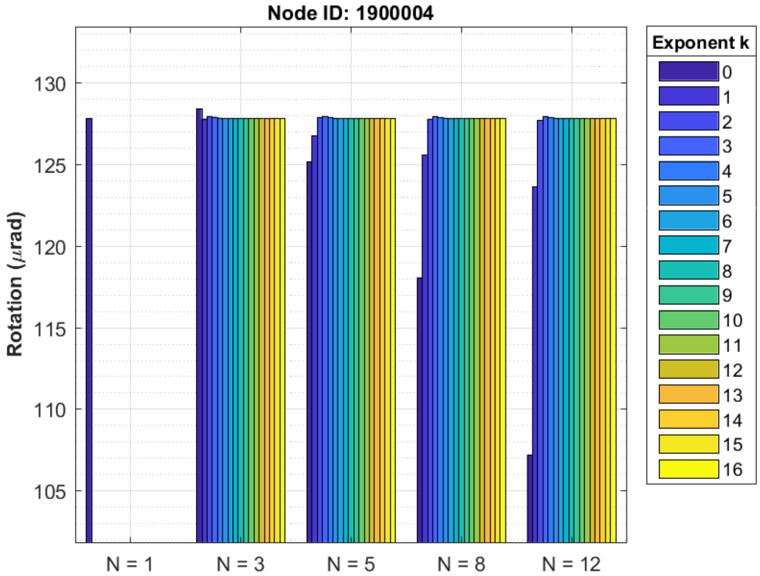

Figure C.12. Rotations comparison for node 1900004.

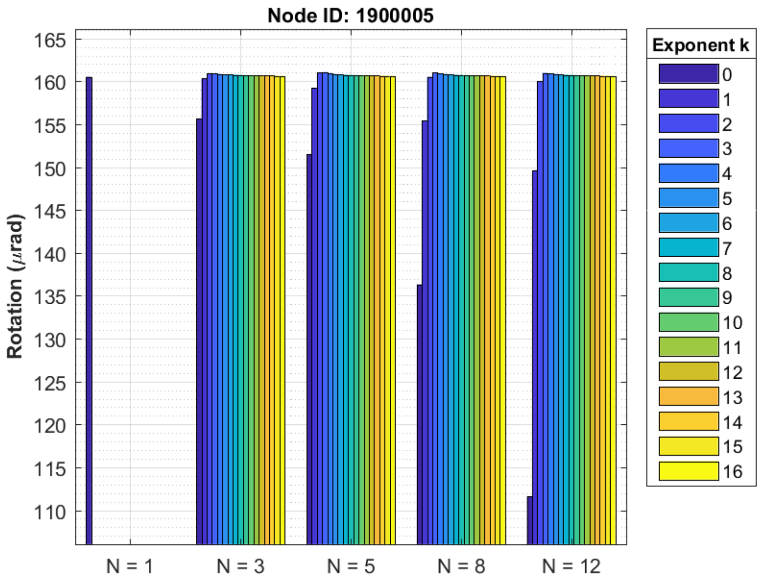

Figure C.13. Rotations comparison for node 1900005.

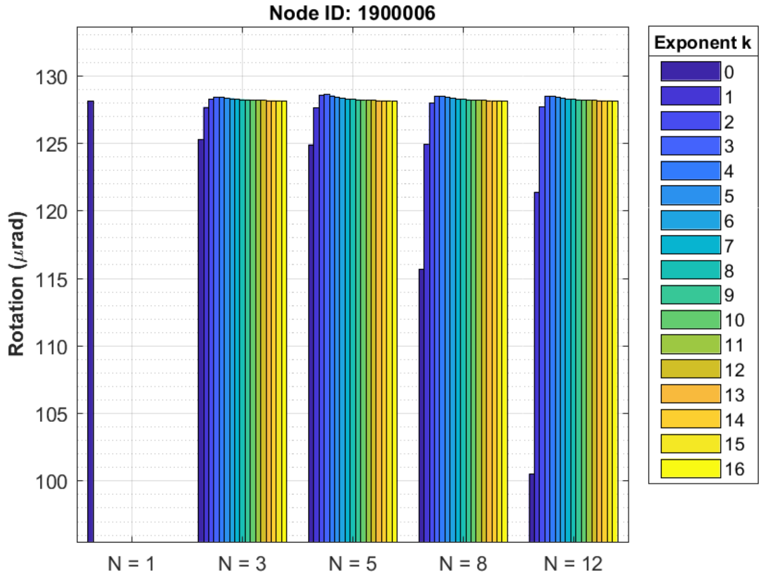

Figure C.14. Rotations comparison for node 1900006.

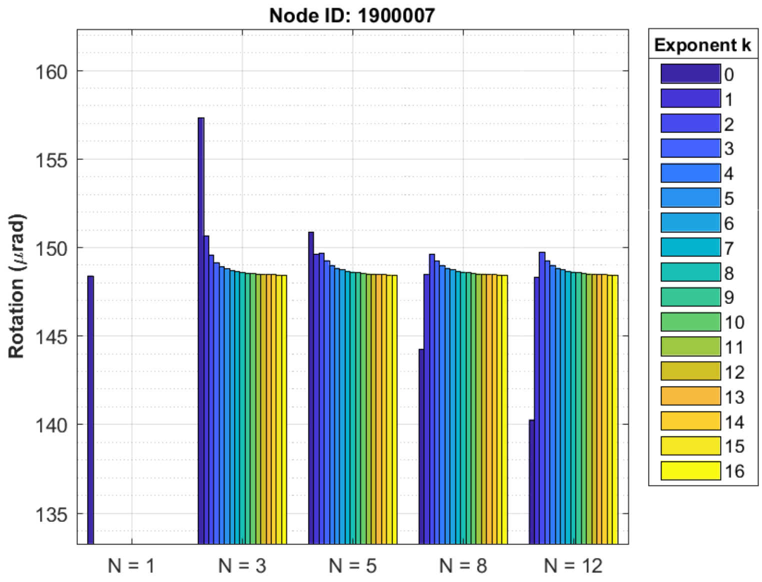

Figure C.15. Rotations comparison for node 1900007.

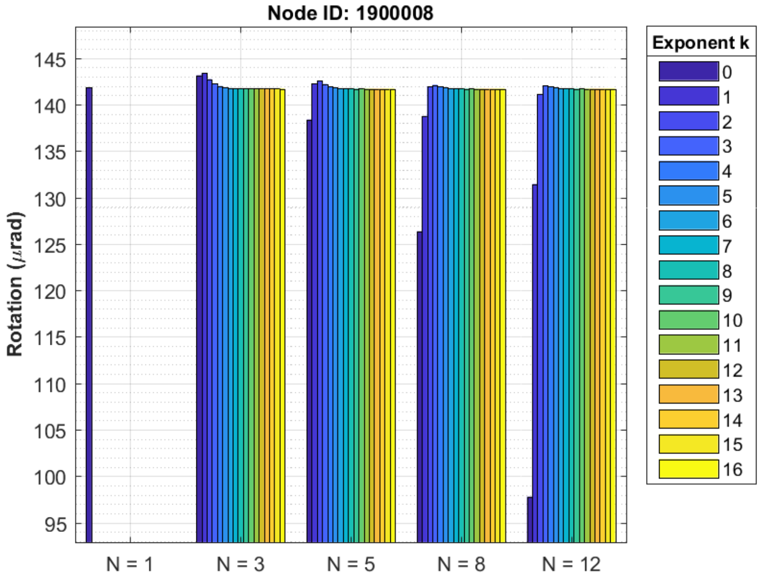

Figure C.16. Rotations comparison for node 1900008.

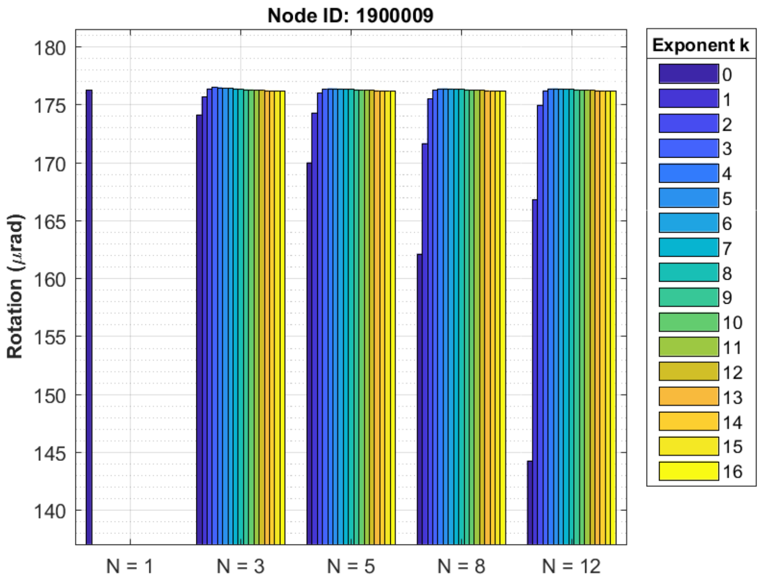

Figure C.17. Rotations comparison for node 1900009.

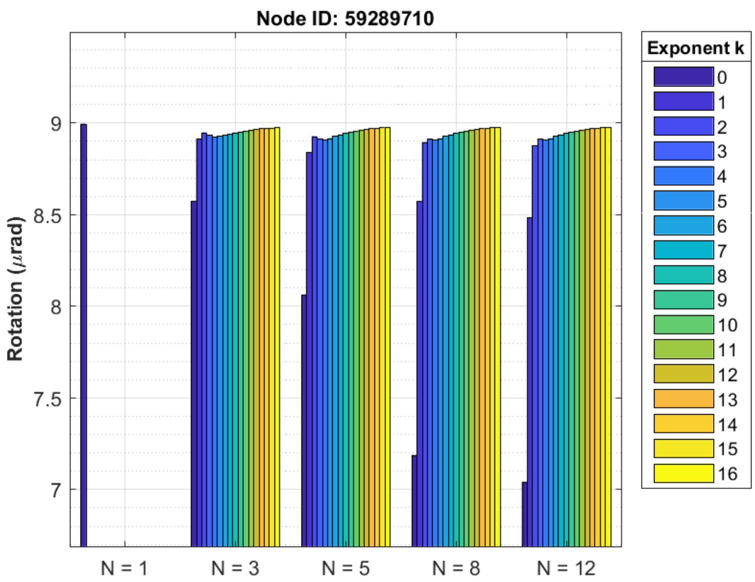

Figure C.18. Rotations comparison for node 59289710.

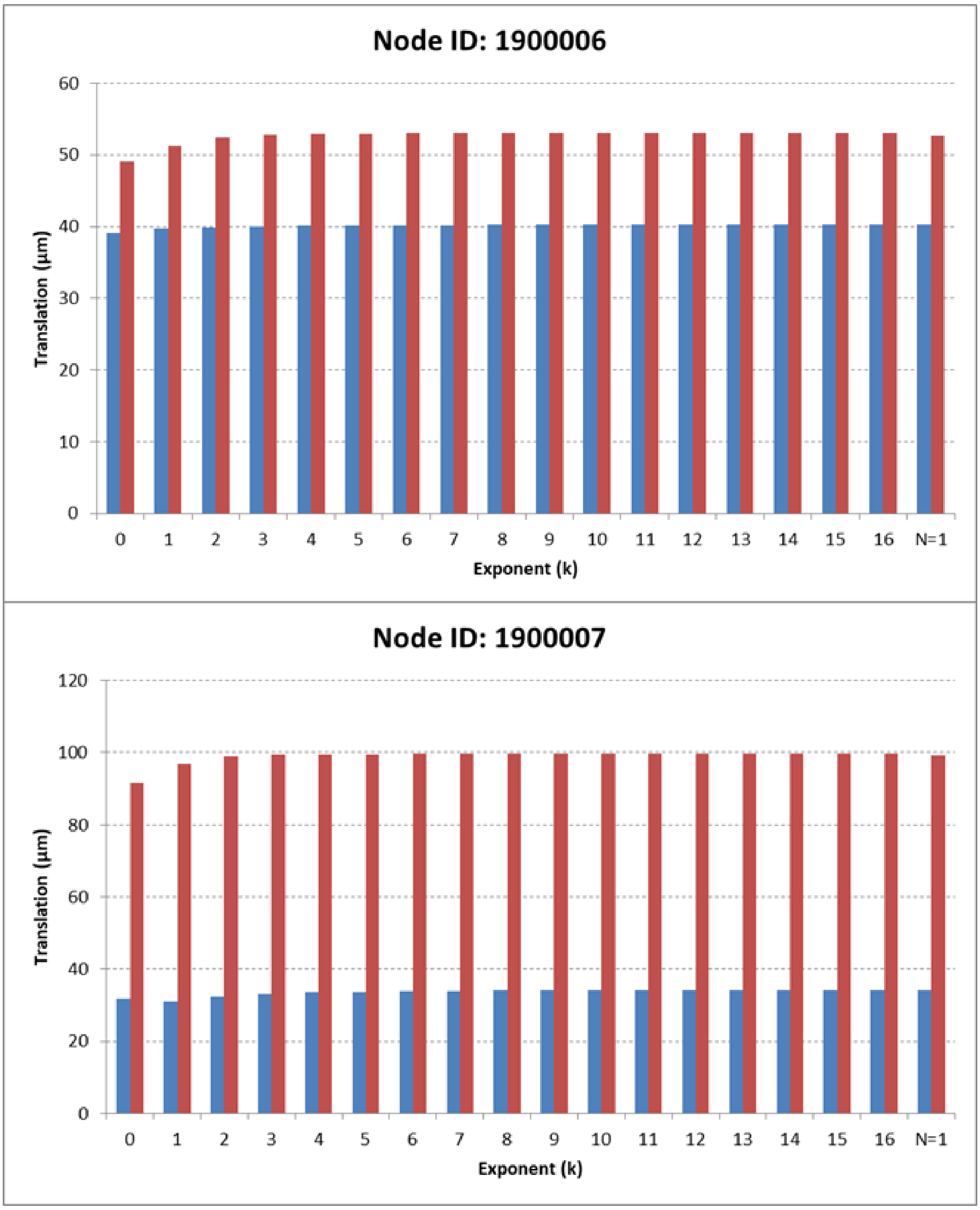

Figure C.19. Comparison of translations between the cases II and VII; nodes 1900004 and 1900005 (blue bars for the case VII).

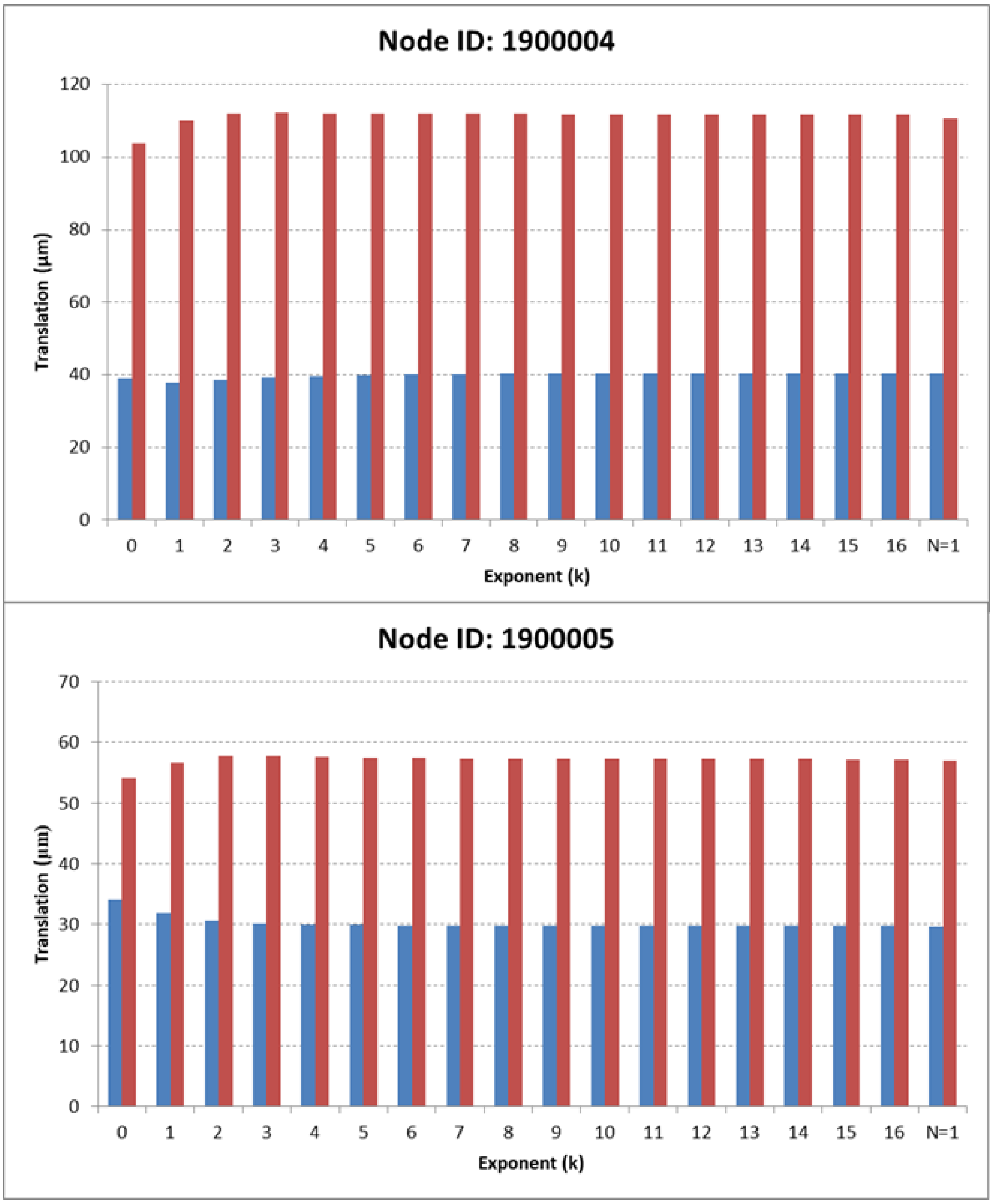

Figure C.20. Comparison of translations between the cases II and VII; nodes 1900006 and 1900007 (blue bars for the case VII).

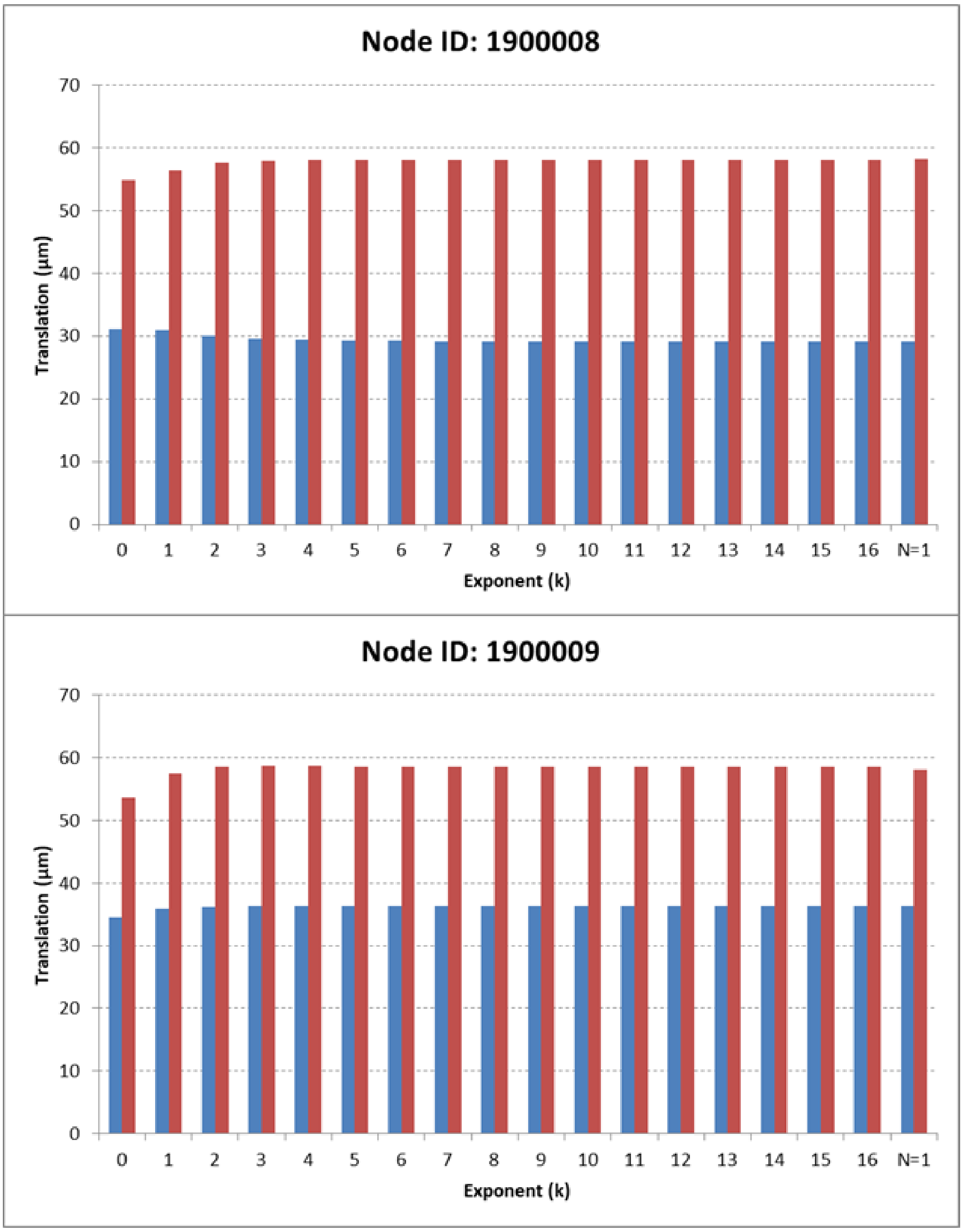

Figure C.21. Comparison of translations between the cases II and VII; nodes 1900008 and 1900009 (blue bars for the case VII).

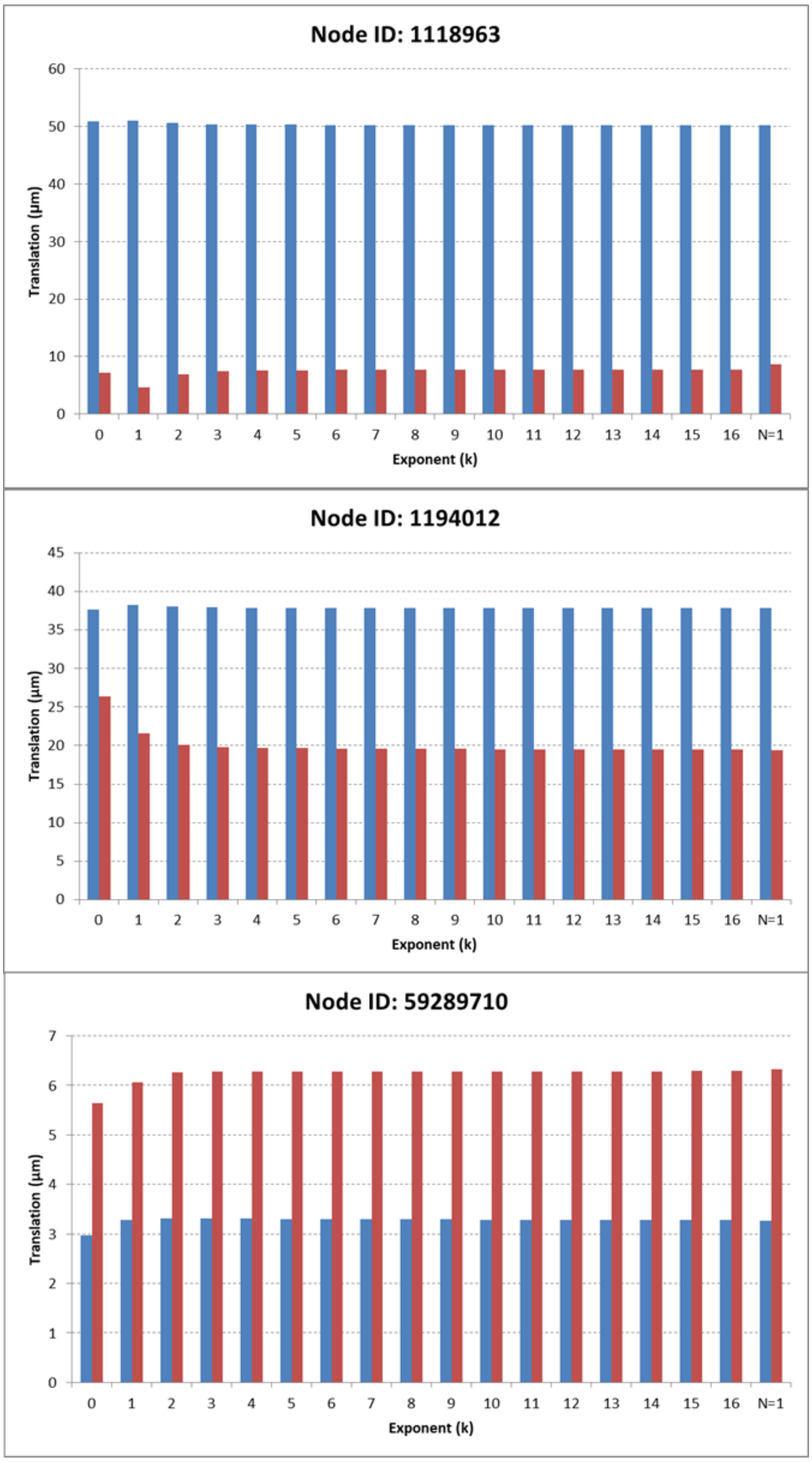

Figure C.22. Comparison of translations between the cases II and VII; nodes 1118963, 1194012 and 59289710 (blue bars for the case VII).

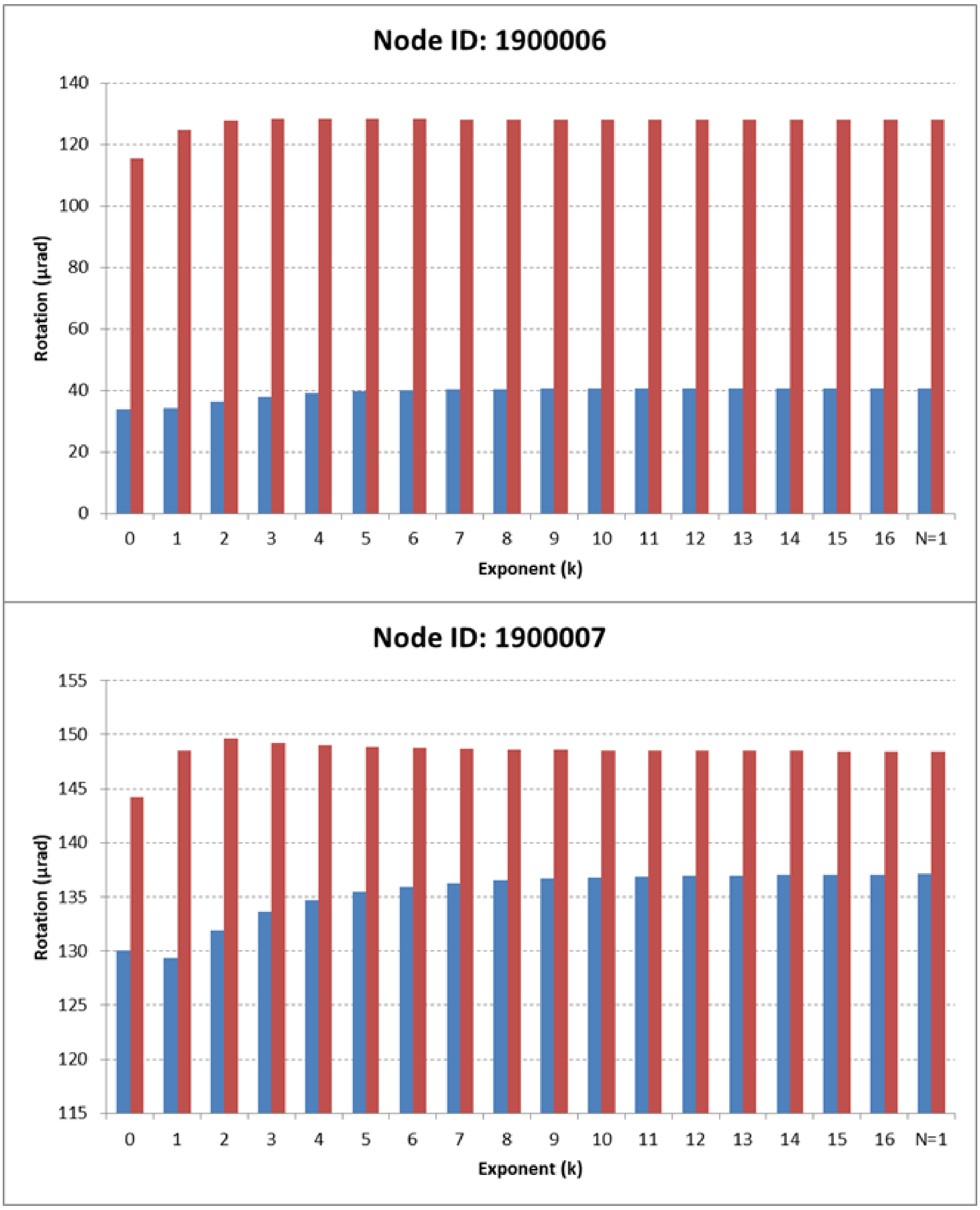

Figure C.23. Comparison of rotations between the cases II and VII; nodes 1900004 and 1900005 (blue bars for the case VII).

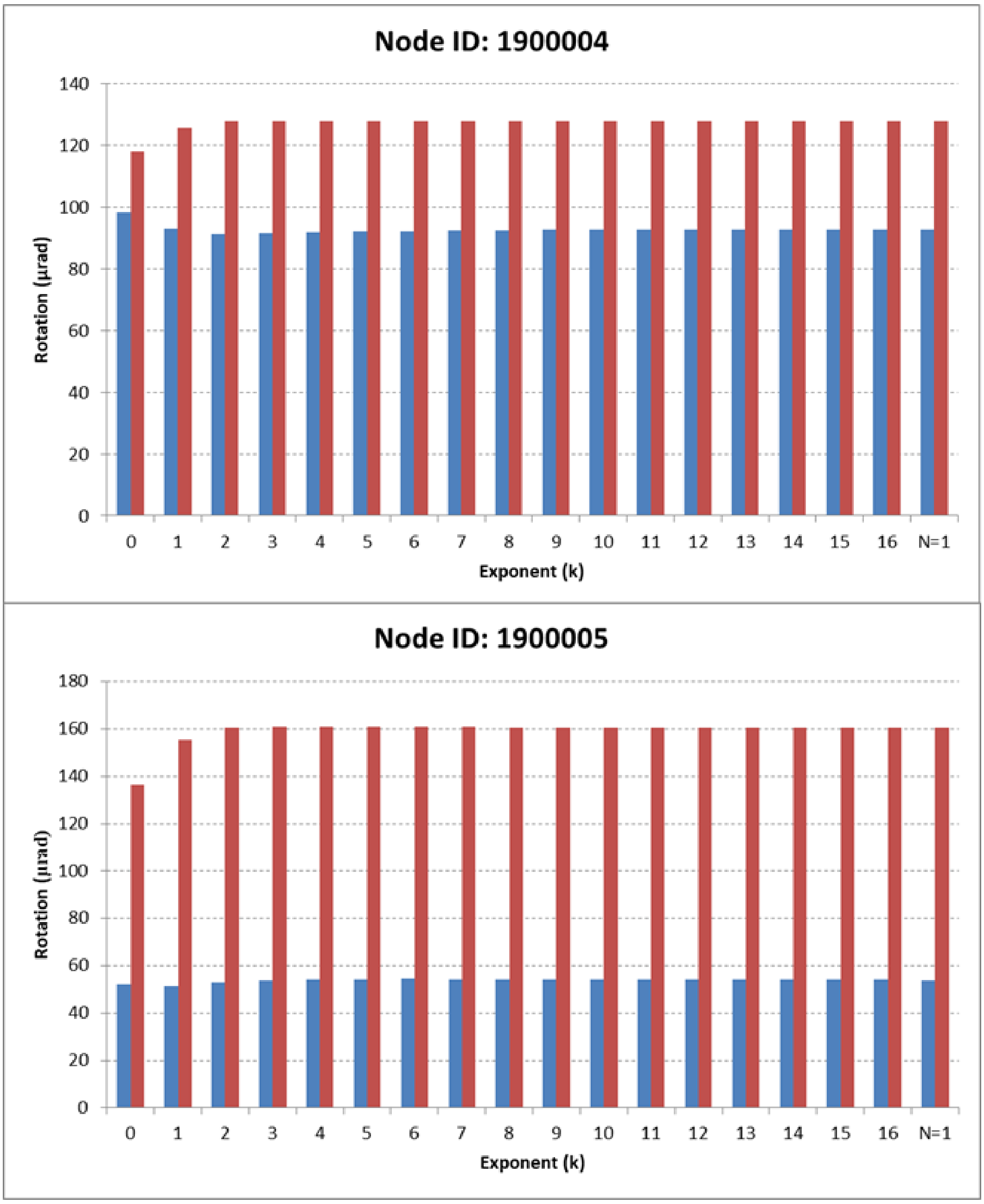

Figure C.24. Comparison of rotations between the cases II and VII; nodes 1900006 and 1900007 (blue bars for the case VII).

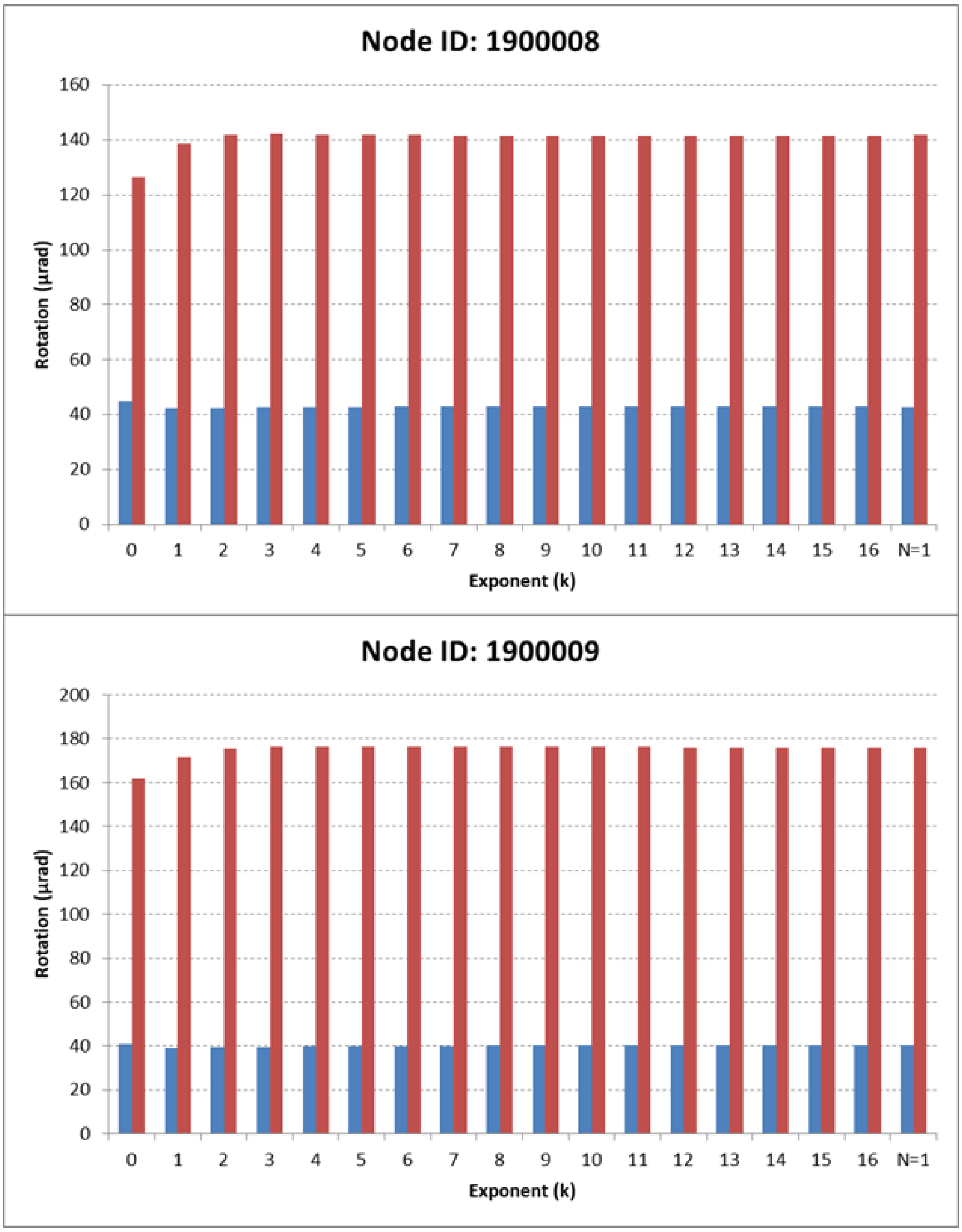

Figure C.25. Comparison of rotations between the cases II and VII; nodes 1900008 and 1900009 (blue bars for the case VII).

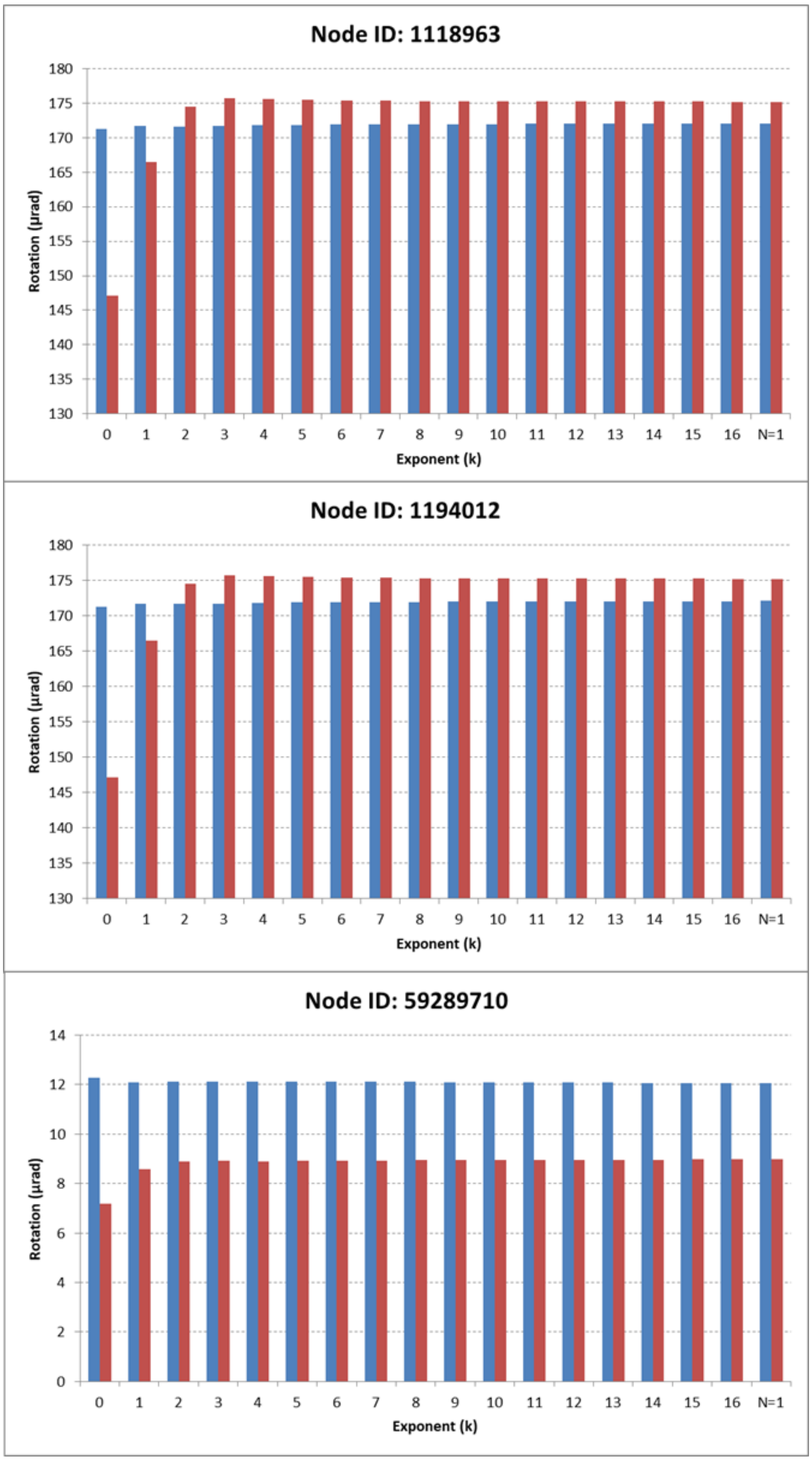

Figure C.26. Comparison of rotations between the cases II and VII; nodes 1118963, 1194012 and 59289710 (blue bars for the case VII).

Table C.1. NRMSE comparison for translations, considering different intervals of k, from case I to V.

Node ID	**Reference translation** (µm)	**NRMSE (%)** $\forall k$	$0 \leq k \leq 3$	$k \geq 4$	**N**
1118963	7.8	5,8	11,7	1,4	3
		5,4	10,9	1,2	5
		10,4	21,3	1,2	8
		22,8	47	1,2	12
1194012	19.2	3,7	7	1,8	3
		6,1	12,2	1,8	5
		9,7	19,8	1,8	8
		16,4	33,7	1,8	12
1900004	111.8	0,5	0,9	0,1	3
		0,2	0,5	0,1	5
		1,8	3,6	0,1	8
		5	10,3	0,1	12
1900005	57.3	1,2	2,4	0,2	3
		1,4	2,9	0,2	5
		1,4	2,9	0,2	8
		5,3	10,9	0,2	12
1900006	53	0,7	1,3	0,1	3
		0,8	1,6	0,1	5
		2	4,1	0,1	8
		4,1	8,5	0,1	12
1900007	99.5	0,2	0,5	0,1	3
		0,4	0,8	0,1	5
		2,1	4,2	0,1	8
		5,3	11	0,1	12
1900008	58	0,5	0,9	0	3
		0,8	1,6	0	5
		1,5	3,2	0	8
		4,1	8,6	0	12
1900009	58.5	0,5	1,1	0,1	3
		0,2	0,3	0,1	5
		2,1	4,3	0,1	8
		5,9	12,2	0,1	12
59289710	6.30	1,3	2,6	0,4	3
		0,9	1,7	0,3	5
		2,7	5,6	0,3	8
		5,5	11,3	0,3	12

Table C.2. NRMSE comparison for rotations, considering different intervals of k, from case I to V.

Node ID	**Reference rotation** (µrad)	**NRMSE (%)**			**N**
		$\forall k$	$0 \leq k \leq 3$	$k \geq 4$	
1118963	175.1	0,2	0,4	0,1	3
		0,5	0,9	0,1	5
		4,1	8,4	0,1	8
		9,5	19,6	0,1	12
1194012	175.1	0,2	0,4	0,1	3
		0,5	0,9	0,1	5
		4,1	8,4	0,1	8
		9,5	19,6	0,1	12
1900004	127.8	0,1	0,2	0	3
		0,5	1,1	0	5
		1,9	3,9	0	8
		4	8,2	0	12
1900005	160.5	0,8	1,5	0,1	3
		1,4	2,8	0,1	5
		3,7	7,7	0,1	8
		7,6	15,6	0,1	12
1900006	128.1	0,6	1,1	0,1	3
		0,6	1,3	0,1	5
		2,4	5	0,1	8
		5,4	11,1	0,1	12
1900007	148.4	1,5	3,1	0,2	3
		0,5	1,1	0,2	5
		0,7	1,5	0,2	8
		1,4	2,8	0,2	12
1900008	141.8	0,4	0,8	0,1	3
		0,6	1,3	0,1	5
		2,7	5,6	0,1	8
		7,7	16	0,1	12
1900009	176.2	0,3	0,6	0,1	3
		0,9	1,9	0	5
		2	4,2	0	8
		4,6	9,5	0	12
59289710	9	1,3	2,4	0,5	3
		2,6	5,3	0,5	5
		5	10,3	0,5	8
		5,5	11,3	0,5	12

Table C.3. NRMSE comparison for translations and rotations, considering different intervals of k, for cases VI, VII, VIII.

Case	Node ID	Reference translation (µm)	NRMSE (%)			Reference rotation (µrad)	NRMSE (%)		
			$\forall k$	$0 \leq k \leq 3$	$k \geq 4$		$\forall k$	$0 \leq k \leq 3$	$k \geq 4$
VII	1118963	50,2	0,5	1	0	172,1	0,2	0,3	0,1
	1194012	37,9	0,3	0,6	0	172,1	0,2	0,3	0,1
	1900004	40,4	2,3	4,7	0,6	92,6	1,6	3,1	0,3
	1900005	29,7	4	8,2	0,3	53,8	1,5	2,8	0,8
	1900006	40,3	0,8	1,6	0,1	40,8	6,6	13,3	1,5
	1900007	34,2	3,3	6,8	0,7	137,2	2,3	4,5	0,7
	1900008	29,2	2,4	4,8	0,2	42,8	1,2	2,5	0,3
	1900009	36,3	1,3	2,7	0	40,2	1	2	0,3
	59289710	3,3	2,3	4,7	0,6	12,1	0,6	1	0,4
VI	1118963	192,2	1,3	2,7	0,2	374,4	0,8	1,6	0,3
	1194012	229,1	1	2,1	0,1	374,4	0,8	1,6	0,3
	1900004	87,8	1,2	2,5	0,1	53,9	6,3	13	0,2
	1900005	145,1	0,3	0,5	0	195,8	0,1	0,2	0
	1900006	117,5	0,4	0,8	0	204,2	0,2	0,4	0
	1900007	76,8	0,6	1,2	0	125,2	2,1	4,4	0,1
	1900008	171,3	0,9	1,8	0,1	103,1	1,6	3,3	0,2
	1900009	124,7	0,4	0,9	0	162,4	1	2	0
	59289710	41,1	0,2	0,4	0	26,2	2,1	4,4	0,1
VIII	49579632	178,7	7,6	15,7	0,1	493,7	5,6	11,5	0
	49579928	270,9	2,8	5,7	0,1	456,2	2,6	5,3	0
	49580425	29,6	2	3,8	0,9	300,4	2,6	5,5	0
	49584826	64,6	2,4	4,9	0,2	141,3	2,4	5	0,2
	49585105	83,2	2,4	4,9	0,4	82	2,5	4,7	1
	49589551	75,1	3,6	7,4	0,2	91,3	5,6	11,6	0,4
	49590619	91,5	3,3	6,7	0,2	56,1	4,4	3,5	4,6
	49590886	76,9	2,5	4,7	1,2	75,7	4,3	8,4	1,6
	49593862	23,6	1,4	2,8	0,5	324,7	5,9	12,1	0

Table C.4. NRMSE comparison for translations and rotations, considering different intervals of k, for the case X.

Case	Node ID	Reference translation (µm)	NRMSE (%)			Reference rotation (µrad)	NRMSE (%)		
			$\forall k$	$0 \leq k \leq 0.9$	$1 \leq k \leq 1.6$		$\forall k$	$0 \leq k \leq 0.9$	$1 \leq k \leq 1.6$
X	1118963	7,8	36,7	40,9	29,5	175,1	9,1	11,5	3,2
	1194012	19,2	20,8	26,1	9	175,1	9,1	11,5	3,2
	1900004	111,8	3,8	4,9	0,9	127,8	4,1	5,3	1
	1900005	57,3	2,9	3,8	0,5	160,5	7,6	9,7	1,9
	1900006	53	4,8	5,9	2,6	128,1	5,1	6,5	1,6
	1900007	99,5	4,8	6	2	148,4	1,6	2	0,6
	1900008	58	4	5	2	141,8	5,6	7,2	1,2
	1900009	58,5	4,5	5,8	1,1	176,2	4,6	5,8	1,8
	59289710	6,3	6,5	8,2	2,6	9	10,1	12,9	3,1

Table C.5. Summary of some results.

Node	TMM	Δt_{max} (°C) [a]	Translation (μm) [b]	Interval of k	N	NRMSE (%)[e]
Interface STR – +z panel (ID: 1118963)	469 TNs[d]	7	7.8	0,1,...,3	3	11.7
					5	10.9
					8	21.3
					12	47
				0.5,0.6,...,1.7	8	38
	201 TNs	3	50.2	0,1,...,3	8	1
	469 TNs with 90 W [c]	26	192.2	0,1,...,3	8	2.7
Interface SVM – PLM (ID: 1900005)	469 TNs	5	57.3	0,1,...,3	3	2.4
					5	2.9
					8	2.9
					12	10.9
				0.5,0.6,...,1.7	8	1.7
	201 TNs	2	29.7	0,1,...,3	8	8.2
	469 TNs with 90 W [c]	4	145.1	0,1,...,3	8	0.5
CDMU – PCDU (ID: 49589551)	469 thermal nodes	18	75.1	0,1,...,3	8	7.4
CDMU – PCDU (ID: 49593862)	469 thermal nodes	9	23.6	0,1,...,3	8	2.8
CDMU – PCDU (ID: 49593862)	469 thermal nodes	18	91.5	0,1,...,3	8	6.7

[a] Considering a radius of 30 cm around the node.
[b] It is the reference value, obtained using N=1.
[c] 469 thermal nodes with additional 90 W (different Esatan inputs).
[d] TN: thermal nodes.
[e] **In general, if $k \geq 4 \Longrightarrow NRMSE < 2\%$**

Appendix D

IRIDIUM thermo-elastic analysis

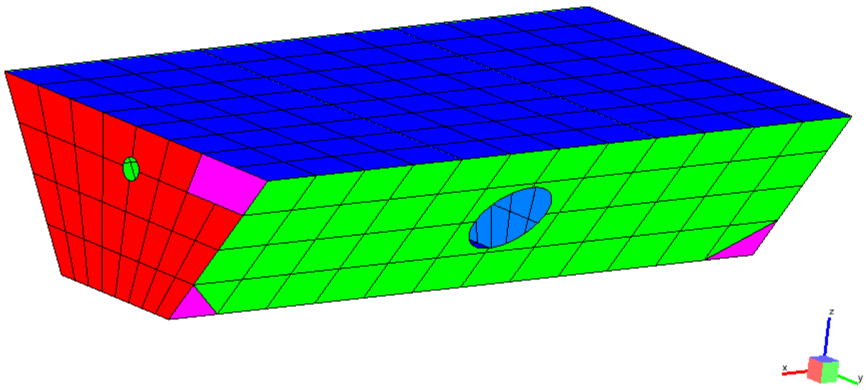

Figure D.1. Thermal model nodal breakdown of the primary structure.

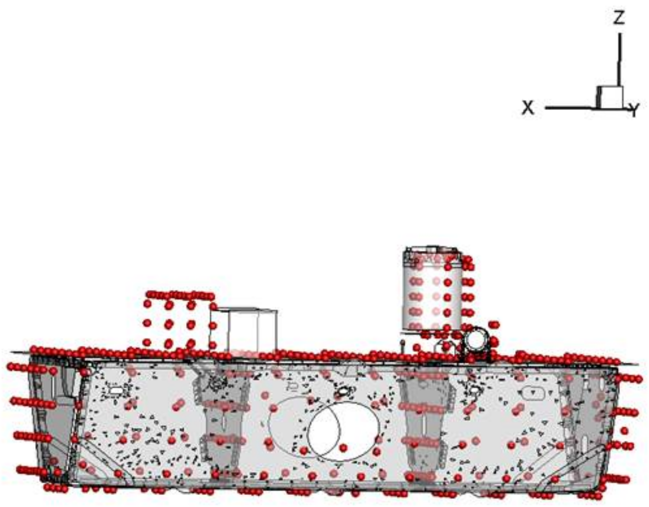

Figure D.2. Some inconsistency between TMM and FEM.

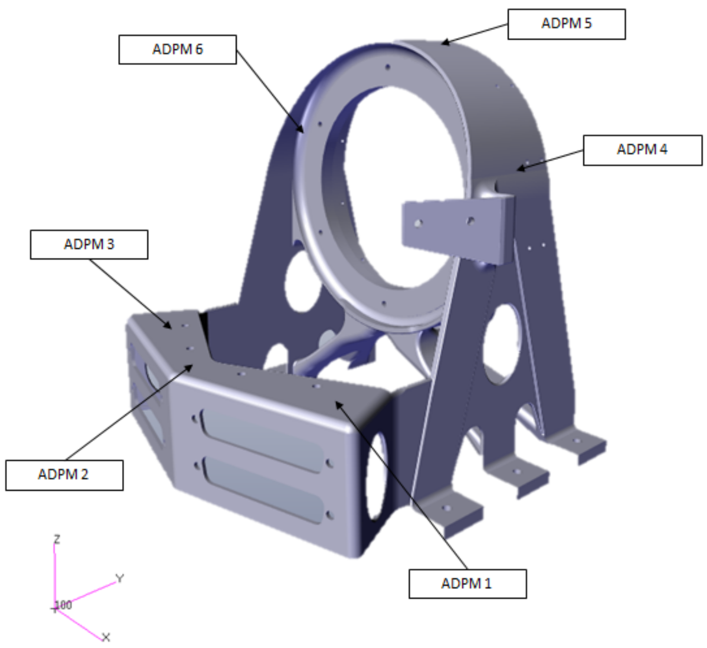

Figure D.3. ADPM output locations.

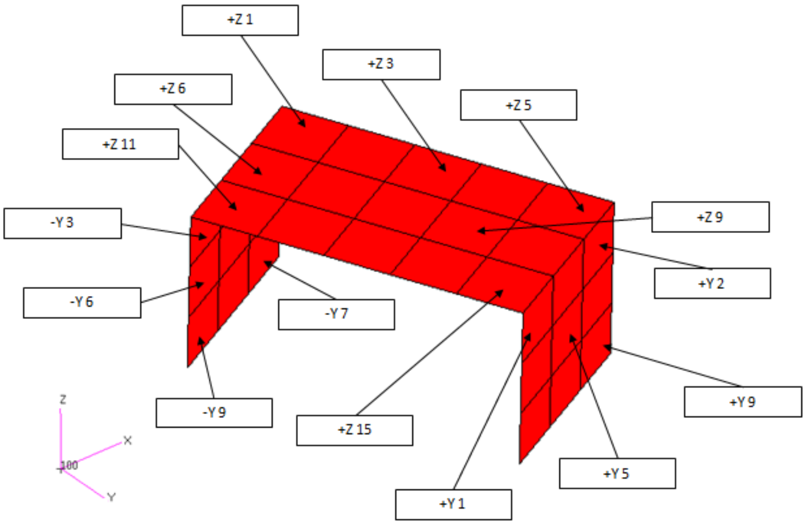

Figure D.4. Composite structure output locations.

6,8	15,3	18,9	18,0	16,2	12,7	15,9	25,7	30,6	33,2	29,1	18,8
10,9	28,3	32,8	30,0	29,6	19,0	23,3	45,4	50,0	55,5	49,1	25,0
13,1	31,7	37,8	36,7	33,6	22,2	26,3	48,9	55,6	58,8	52,7	30,3
13,3	25,7	31,1	28,2	27,4	22,1	24,9	35,5	38,7	43,6	39,6	29,1
15,2	29,4	35,4	31,9	30,6	23,4	24,8	34,2	37,0	41,8	38,2	28,5
18,5	43,8	52,1	50,0	44,6	25,8	26,1	44,5	50,0	52,9	47,9	29,0
18,4	42,5	50,0	44,6	41,9	23,3	23,0	40,4	43,7	48,6	43,6	25,3
13,7	24,8	29,8	28,3	23,8	15,9	15,5	22,4	26,1	27,9	24,6	16,9

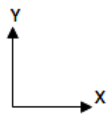

Panel +z, $[T] = °C$

Figure D.5. Temperature values distribution on the nodal breakdown of panel +z.

-2,8	8,7	9,4	-0,6	-2,2	7,4	7,2	-1,3	2,7	13,5	12,7	-0,2
-2,3	10,5	11,5	0,9	0,1	10,1	10,3	-1,2	4,3	16,7	15,8	1,0
-3,7	8,4	3,0	-1,2	-0,4	9,8	9,8	-1,1	4,4	16,7	15,7	1,0
-6,8	1,2	3,2	-3,1	-3,5	6,3	6,4	-1,4	3,0	13,2	12,3	-0,1

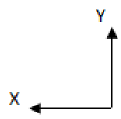

Panel -z, $[T] = °C$

Figure D.6. Temperature values distribution on the nodal breakdown of panel -z.

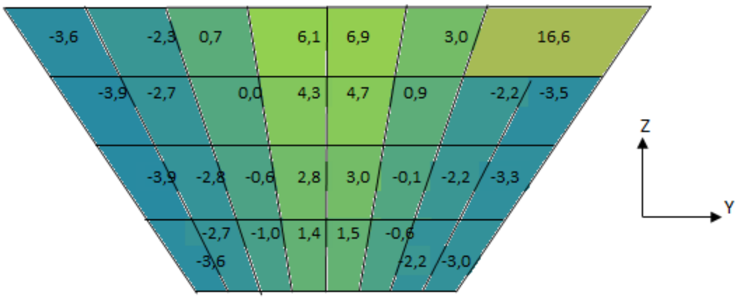

Panel +x, $[T] = °\mathrm{C}$

Figure D.7. Temperature values distribution on the nodal breakdown of panel +x.

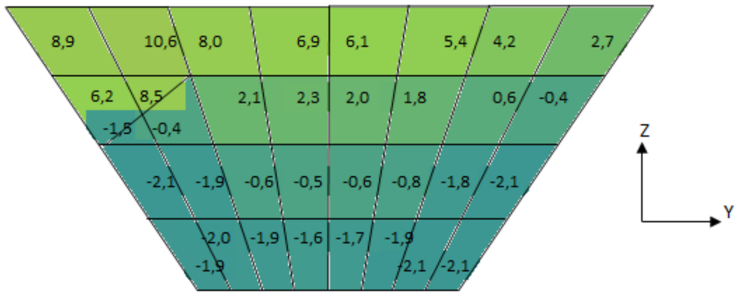

Panel -x, $[T] = °\mathrm{C}$

Figure D.8. Temperature values distribution on the nodal breakdown of panel -x.

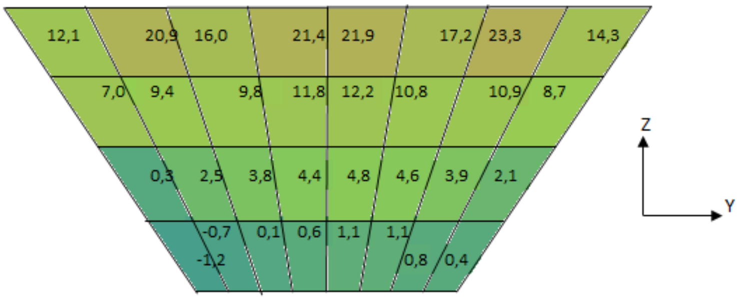

Internal stiffener +x, $[T] = °\mathrm{C}$

Figure D.9. Temperature values distribution on the nodal breakdown of internal panel +x.

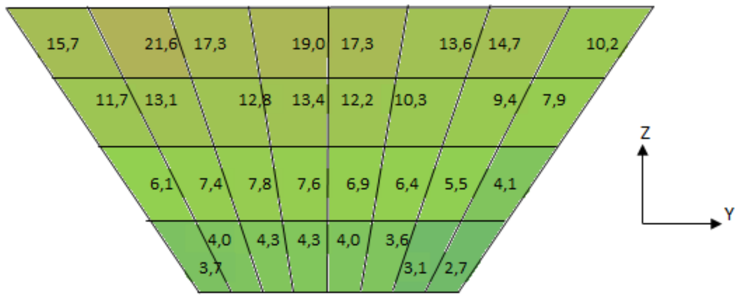

Internal stiffener -x, $[T] = °C$

Figure D.10. Temperature values distribution on the nodal breakdown of internal panel -x.

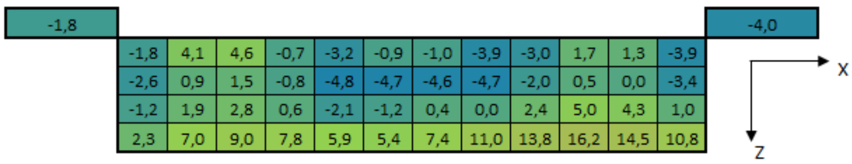

Panel +y, $[T] = °C$

Figure D.11. Temperature values distribution on the nodal breakdown of panel +y.

Panel -y, $[T] = °C$

Figure D.12. Temperature values distribution on the nodal breakdown of panel -y.

Telescope mock-up, [T] = °C		
	Lateral	Top
Cage M2	1,8	0,0

	+X	+Y	-Y
Blades	0,0	-0,5	0,1
Brackets	-5,2	-5,2	-5,2

	Cylinder					
	-30° / +30°	+30° / +90°	+90° / +150°	+150° / +210°	+210° / +270°	+270° / -30°
Crown	-5,0	-5,1	-5,0	-5,0	-5,0	-4,9
Z5	0,0	0,2	0,1	0,3	0,0	0,4
Z4	-7,1	-6,9	-7,1	-6,9	-7,1	-6,7
Z3	0,0	0,1	-0,2	-0,2	0,0	0,1
Z2	-3,8	-4,0	-4,0	-4,2	-4,0	-4,1
Z1	0,0	-0,4	-0,2	-0,6	-0,2	-0,5

Mirror M1	-0,5

Support of M1					
-30° / +30°	+30° / +90°	+90° / +150°	+150° / +210°	+210° / +270°	+270° / -30°
0,0	-2,4	-0,6	-2,6	-0,8	-2,4

Telescope fixation devices		
+X	+Y	-Y
17,6	11,6	10,9

Figure D.13. Temperature values distribution on the nodal breakdown of DSS.

Composite structure, [T] = °C

Panel -X

-0,6	-0,6	-0,5
0,2	0,0	0,3
2,4	1,0	2,5

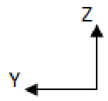

Panel +X

-0,6	-0,7	-0,6
0,4	0,0	0,3
2,9	1,1	2,7

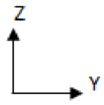

Panel +Z

-0,3	-0,3	-0,2	-0,2	-0,1
-0,1	-0,1	0,0	0,1	0,5
0,5	0,5	0,6	0,6	0,7

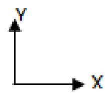

Figure D.14. Temperature values distribution on the nodal breakdown of composite structure.

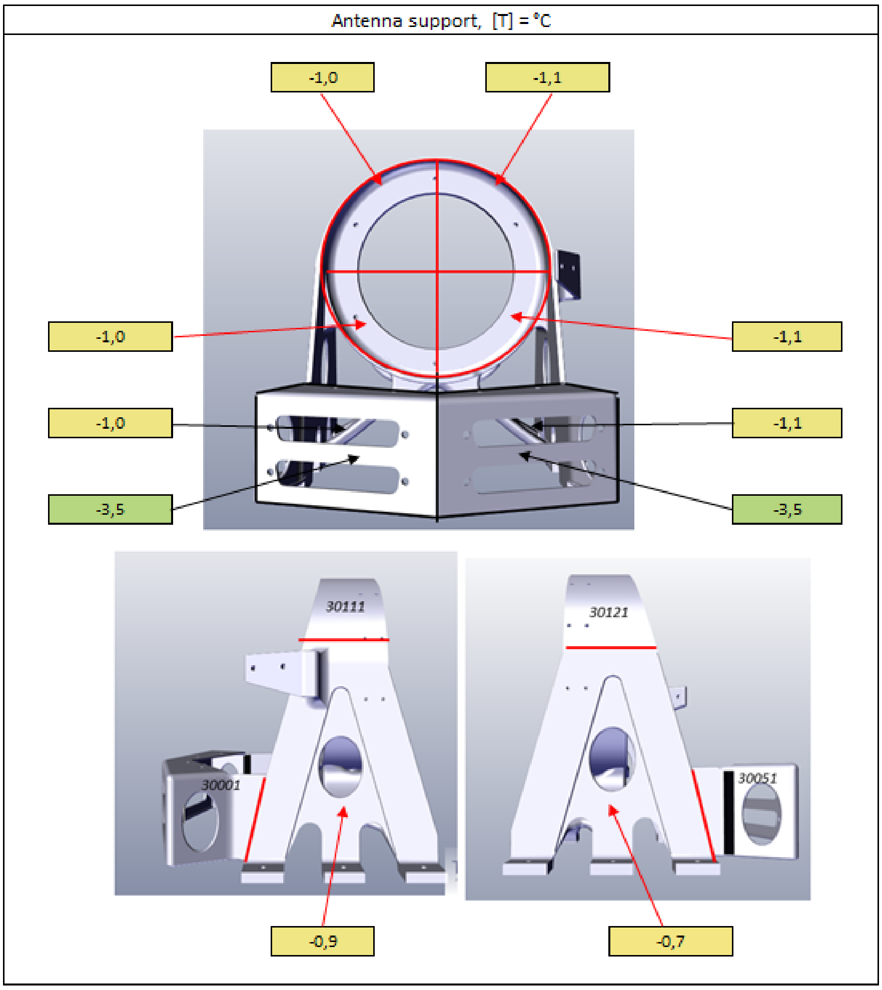

Figure D.15. Temperature values distribution on the nodal breakdown of ADPM.

D.1 Results

Table D.1. Translations and rotations of recovery nodes on panel +z.

Node label	T_x (µm)	T_y (µm)	T_z (µm)	R_x (µrad)	R_y (µrad)	R_z (µrad)
A1	6	75	-270	-1408	-1539	62
A2	-16	112	-44	-1441	-1445	-13
A3	-10	147	131	-1570	-1053	-173
A4	10	180	281	-1398	-665	38
A5	9	164	411	-1299	-490	-36
A6	12	169	498	-1274	-34	-34
A7	-36	206	540	-1307	-308	263
A8	-56	318	585	-1468	-414	519
A9	36	439	551	-1751	259	316
A10	118	524	441	-1815	660	293
A11	224	542	310	-1733	924	-23
A12	286	502	121	-1868	1538	-61
A13	318	473	-109	-2185	1684	71
B1	-37	108	-41	-1052	-1407	-136
B2	-61	132	214	-919	-1195	-179
B3	-38	172	428	-955	-875	12
B4	2	181	603	-989	-672	-30
B5	24	172	725	-1102	-413	-6
B6	30	183	797	-1033	-206	72
B7	3	210	846	-1127	-233	169
B8	-1	304	917	-1151	-206	252
B9	63	376	954	-1310	148	207
B10	166	440	834	-1288	592	198
B11	305	451	692	-1226	833	215
B12	411	430	481	-1154	1166	257
B13	478	413	245	-1073	1301	531
C1	-108	112	156	-486	-1358	-157
C2	-112	100	404	-531	-1185	-76
C3	-71	106	614	-589	-930	-32
C4	-7	111	789	-584	-669	1
C5	47	111	904	-623	-473	-28
C6	58	136	1009	-633	-304	72
C7	34	163	1090	-662	-250	118
C8	31	193	1142	-613	-149	132
C9	94	210	1153	-620	165	312
C10	222	252	1067	-623	565	106
C11	367	267	910	-649	922	70
C12	497	267	685	-629	1262	37

C13	559	273	427	-704	1459	-72
D1	-148	104	252	-387	-1582	-145
D2	-147	87	519	-345	-1237	-116
D3	-88	79	747	-375	-940	-63
D4	-8	79	913	-358	-619	33
D5	45	88	1008	-308	-453	49
D6	74	97	1125	-268	-318	66
D7	66	107	1197	-226	-223	81
D8	80	116	1247	-157	-92	75
D9	137	134	1242	-118	158	59
D10	237	147	1170	-211	499	37
D11	367	151	1035	-227	878	5
D12	486	148	798	-202	1301	-42
D13	542	139	532	-213	1573	-70
E1	-212	68	334	-372	-1309	-235
E2	-194	35	583	-149	-1176	-114
E3	-105	31	814	-28	-948	35
E4	-9	30	971	2	-583	-64
E5	78	26	1070	-21	-355	49
E6	115	29	1141	172	-206	74
E7	96	38	1191	269	-172	56
E8	85	52	1236	231	-110	62
E9	128	51	1240	148	127	40
E10	225	49	1185	175	443	-19
E11	340	49	1056	210	839	-36
E12	465	55	804	212	1313	-77
E13	521	47	533	301	1644	-168
F1	-191	-38	318	708	-1241	295
F2	-164	-84	553	576	-1025	33
F3	-89	-126	729	644	-845	11
F4	15	-137	894	669	-656	50
F5	85	-103	1005	602	-264	72
F6	128	-69	1034	666	-89	118
F7	112	-28	1062	734	-118	48
F8	93	-43	1103	772	-126	-41
F9	135	-81	1109	880	81	-80
F10	211	-101	1069	897	424	-144
F11	303	-89	909	925	995	-175
F12	379	-75	690	996	1221	-160
F13	419	-44	399	1091	1735	-333
G1	-99	-64	75	1560	-1767	-176
G2	-93	-128	320	1289	-1426	-222
G3	-54	-193	495	1195	-907	-173

G4	40	-202	653	1263	-706	137
G5	96	-160	766	1188	-345	197
G6	140	-99	826	964	-28	274
G7	122	-28	841	958	-65	42
G8	103	-68	864	1058	-94	-184
G9	134	-112	831	1388	152	-139
G10	181	-159	717	1636	559	-164
G11	243	-137	570	2124	2428	-412
G12	290	-103	349	1906	2164	-198
G13	328	-84	107	1722	1862	-227
Max.	559	542	1247	2124	2428	531
Min.	-212	-202	-270	-2185	-1767	-412
Range: max − min	771	744	1517	4309	4195	943

Table D.2. Translations and rotations of telescope recovery nodes.

Node label	T_x (µm)	T_y (µm)	T_z (µm)	R_x (µrad)	R_y (µrad)	R_z (µrad)
DSS M1	-49	-319	855	914	-571	87
DSS M2	-266	-666	859	914	-571	91
DSS Bracket +X	-253	-628	961	930	-588	86
DSS Bracket +Y	-259	-648	898	922	-551	87
DSS Bracket -Y	-239	-643	711	894	-560	87
DSS Crown +X+Y	-260	-634	1011	919	-573	88
DSS Crown -X	-246	-650	754	912	-565	86
DSS Crown +X-Y	-241	-628	830	910	-575	85
DSS Cylinder +X	-133	-441	944	912	-567	79
DSS Cylinder -X	-133	-468	760	913	-570	92
DSS Cylinder +Y	-148	-455	992	914	-571	77
DSS Cylinder -Y	-121	-454	723	916	-572	97
Max.	-49	-319	1011	930	-551	97
Min.	-266	-666	711	894	-588	77
Range: max - min	217	347	300	36	37	20

Table D.3. Translations and rotations of composite structure recovery nodes.

Node label	T_x (µm)	T_y (µm)	T_z (µm)	R_x (µrad)	R_y (µrad)	R_z (µrad)
Composite struct. +Z 1	112	148	1216	-242	1	62
Composite struct. +Z 2	105	149	1194	-180	4	59
Composite struct. +Z 3	100	149	1179	-138	7	59
Composite struct. +Z 4	94	149	1168	-96	11	59
Composite struct. +Z 5	88	150	1161	-36	17	56
Composite struct. +Z 6	112	154	1216	-210	-2	59
Composite struct. +Z 7	106	154	1194	-180	3	59
Composite struct. +Z 8	100	155	1179	-140	7	59
Composite struct. +Z 9	95	155	1167	-101	10	60
Composite struct. +Z 10	88	155	1159	-71	14	60
Composite struct. +Z 11	113	159	1216	-253	-5	54
Composite struct. +Z 12	106	160	1193	-186	1	59
Composite struct. +Z 13	101	160	1178	-142	7	59
Composite struct. +Z 14	95	161	1166	-99	9	60
Composite struct. +Z 15	89	161	1158	-36	10	65
Composite struct. -Y 1	116	146	1232	-446	-7	27
Composite struct. -Y 2	116	148	1233	-475	-10	43
Composite struct. -Y 3	116	155	1234	-451	-11	63
Composite struct. -Y 4	116	100	1232	-444	0	29
Composite struct. -Y 5	117	103	1232	-467	-10	32
Composite struct. -Y 6	117	106	1234	-463	-19	35
Composite struct. -Y 7	115	58	1231	-381	47	39
Composite struct. -Y 8	118	60	1231	-454	-10	21
Composite struct. -Y 9	121	59	1234	-371	-96	-3
Composite struct. +Y 1	84	160	1158	155	14	58
Composite struct. +Y 2	84	156	1159	177	17	78
Composite struct. +Y 3	84	147	1161	134	19	94
Composite struct. +Y 4	83	182	1158	163	4	88
Composite struct. +Y 5	83	173	1158	168	17	91
Composite struct. +Y 6	82	165	1161	141	29	94
Composite struct. +Y 7	85	200	1158	58	-102	128
Composite struct. +Y 8	81	188	1157	154	17	105
Composite struct. +Y 9	77	179	1161	44	136	83
Max.	121	200	1234	177	136	128
Min.	77	58	1157	-475	-102	-3
Range: max - min	44	142	77	652	238	131

Table D.4. Translations and rotations of antenna support recovery nodes.

Node label	T_x (µm)	T_y (µm)	T_z (µm)	R_x (µrad)	R_y (µrad)	R_z (µrad)
ADPM 1	-63	310	619	0	0	0
ADPM 2	-28	326	604	0	0	0
ADPM 3	10	315	534	0	0	0
ADPM 4	-107	353	438	0	0	0
ADPM 5	-92	422	376	0	0	0
ADPM 6	-18	364	372	0	0	0
Max.	10	422	619	–	–	–
Min.	-107	310	372	–	–	–
Range: max - min	117	112	247	–	–	–

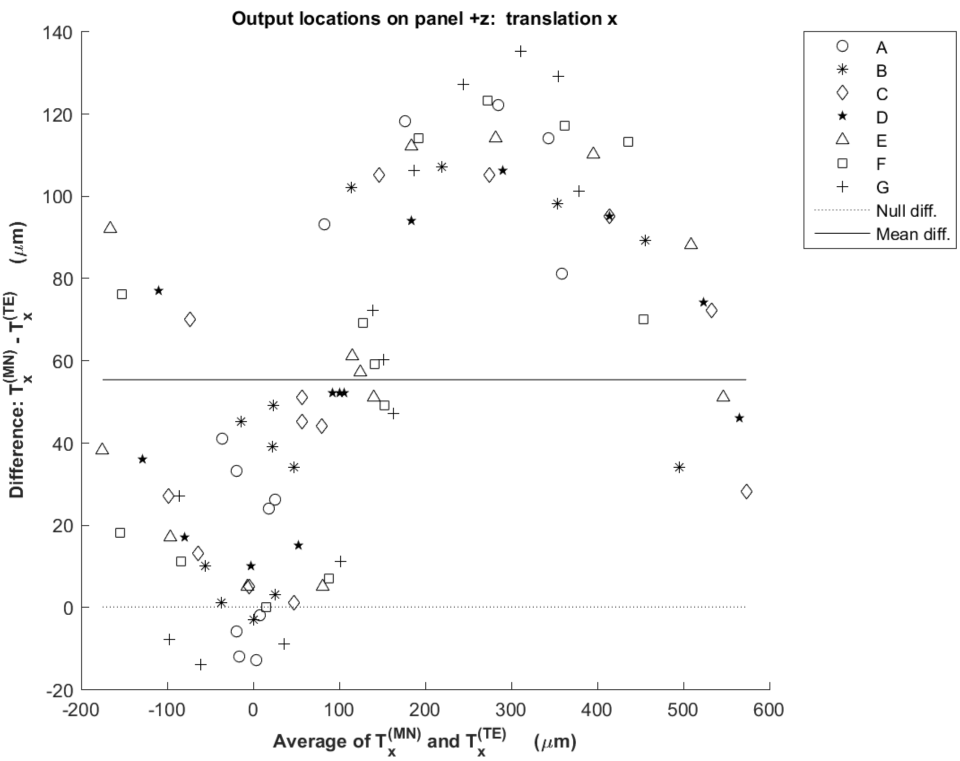

Figure D.16. Comparison between the manual method (superscript MN) and the TEMASE one (superscript TE) for T_x.

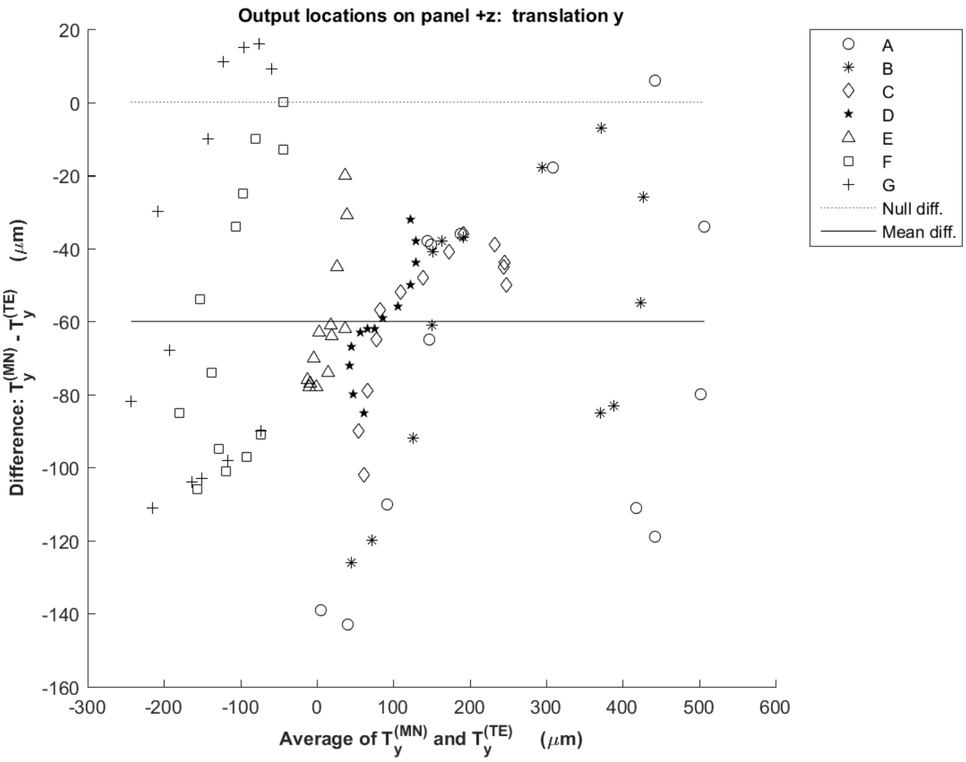

Figure D.17. Comparison between the manual method (superscript MN) and the TEMASE one (superscript TE) for T_y.

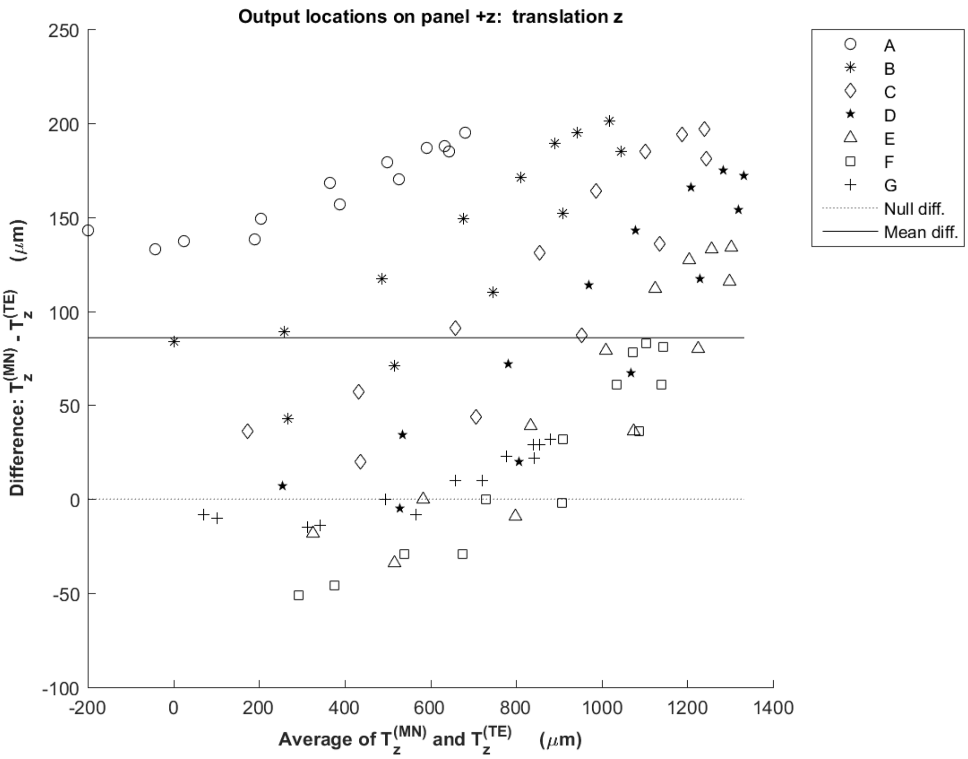

Figure D.18. Comparison between the manual method (superscript MN) and the TEMASE one (superscript TE) for T_z.

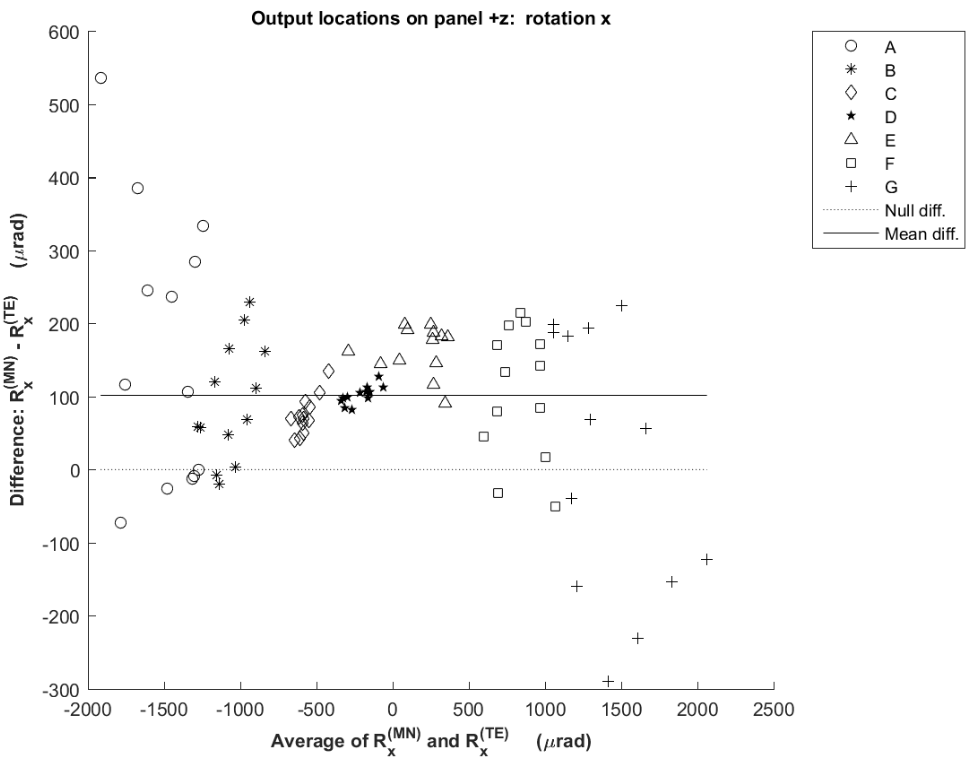

Figure D.19. Comparison between the manual method (superscript *MN*) and the TEMASE one (superscript *TE*) for R_x.

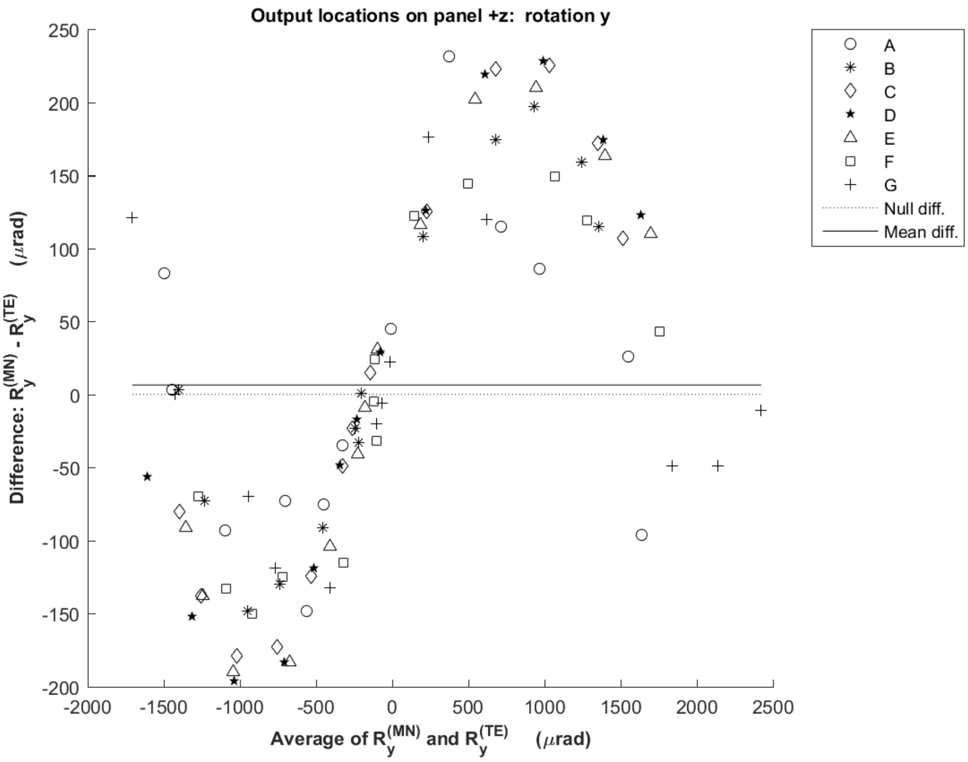

Figure D.20. Comparison between the manual method (superscript MN) and the TEMASE one (superscript TE) for R_y.

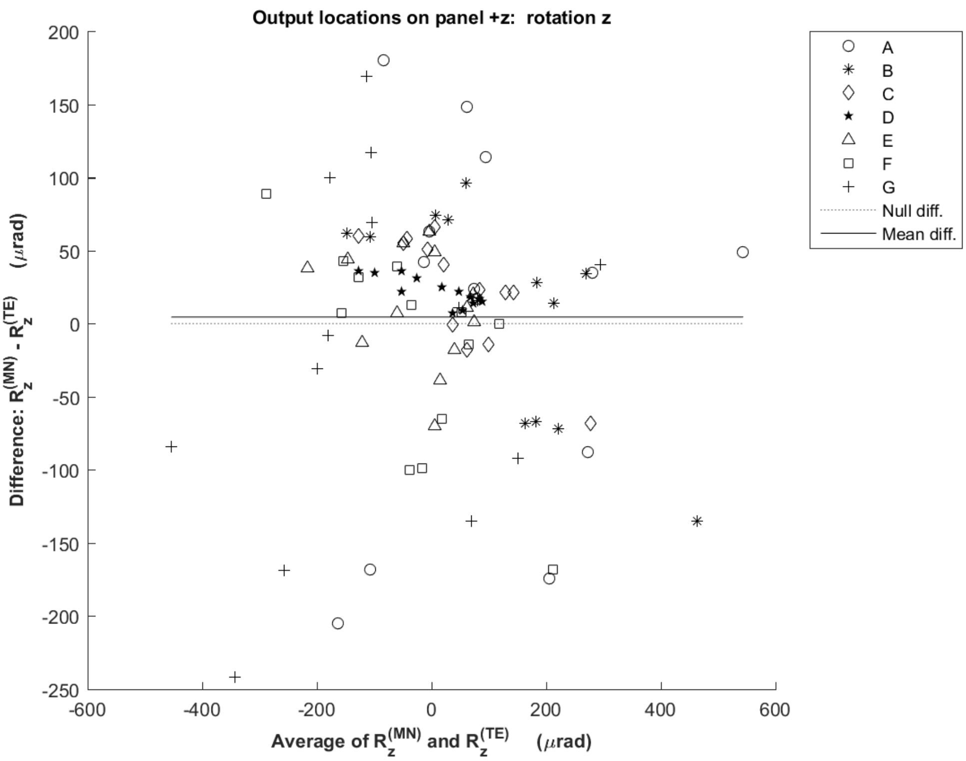

Figure D.21. Comparison between the manual method (superscript *MN*) and the TEMASE one (superscript *TE*) for R_z.

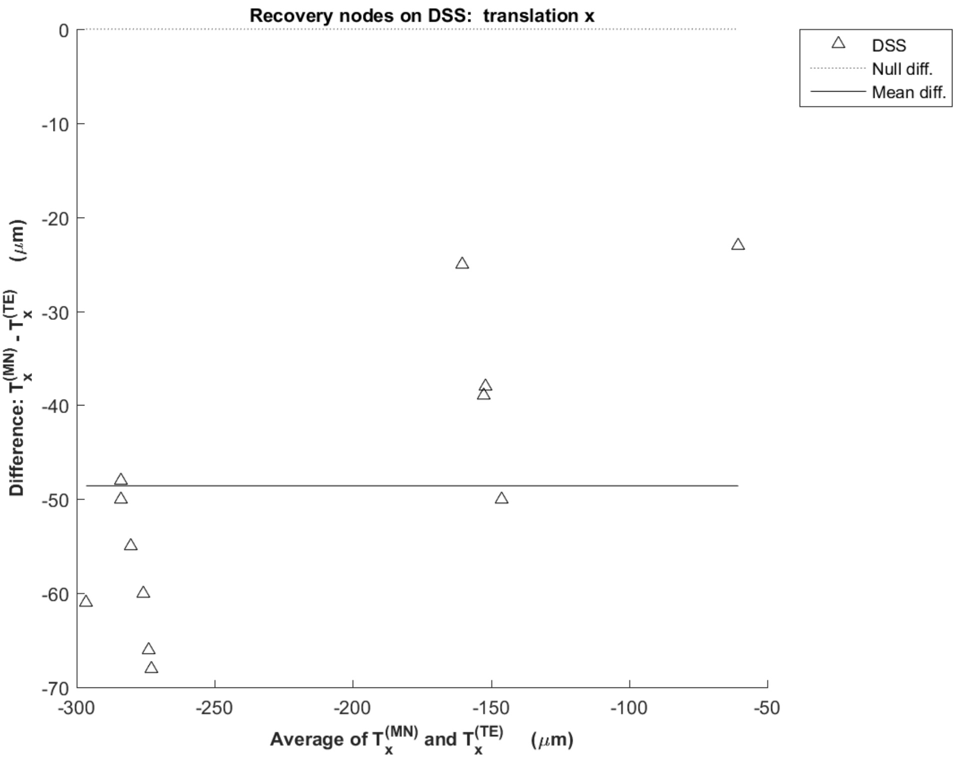

Figure D.22. Comparison between the manual method (superscript MN) and the TEMASE one (superscript TE) for T_x of the telescope.

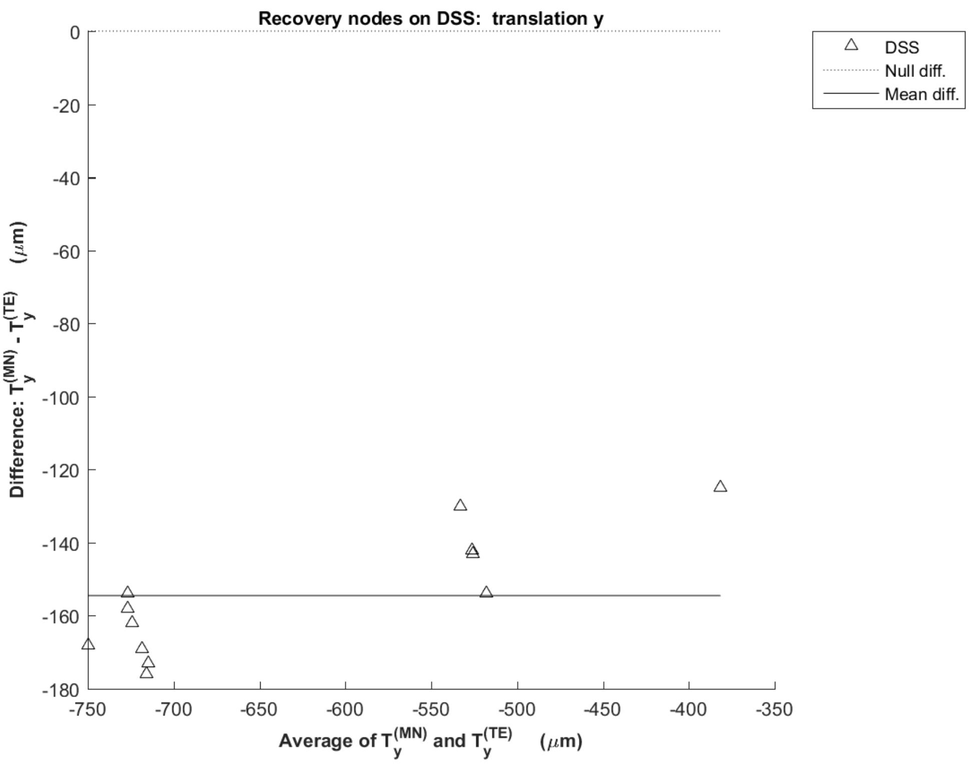

Figure D.23. Comparison between the manual method (superscript MN) and the TEMASE one (superscript TE) for T_y of the telescope.

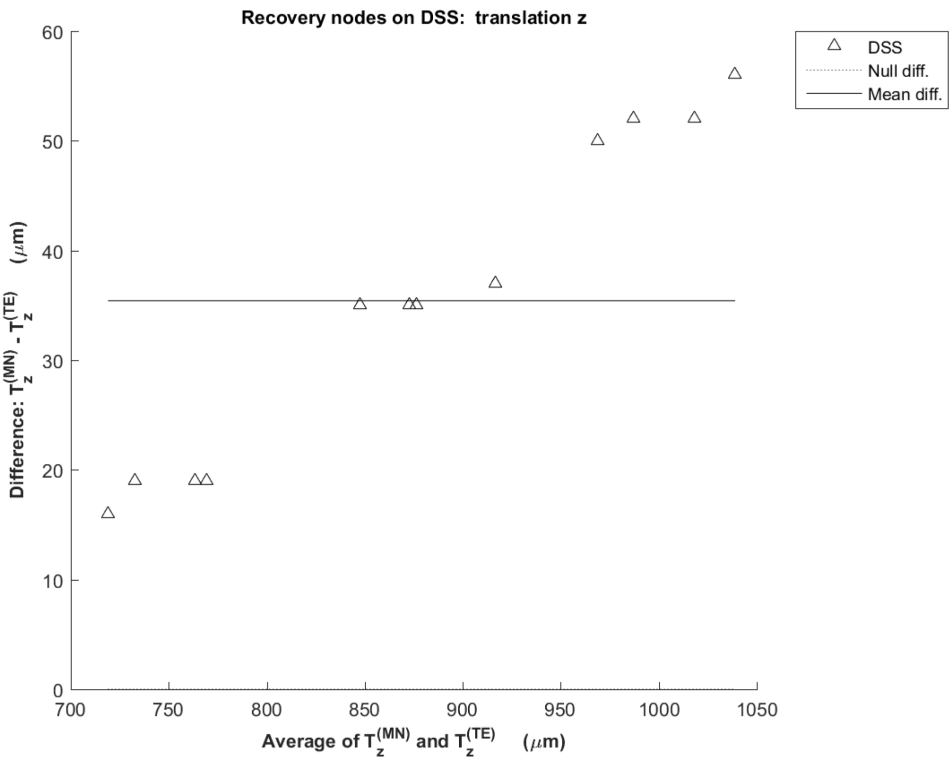

Figure D.24. Comparison between the manual method (superscript MN) and the TEMASE one (superscript TE) for T_z of the telescope.

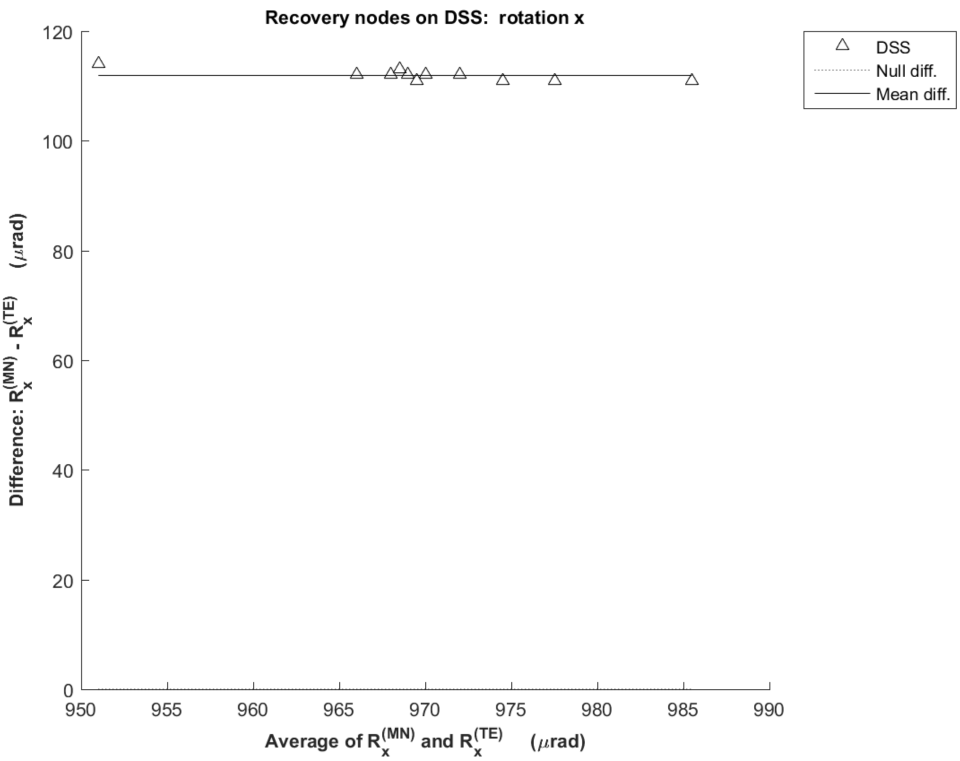

Figure D.25. Comparison between the manual method (superscript *MN*) and the TEMASE one (superscript *TE*) for R_x of the telescope.

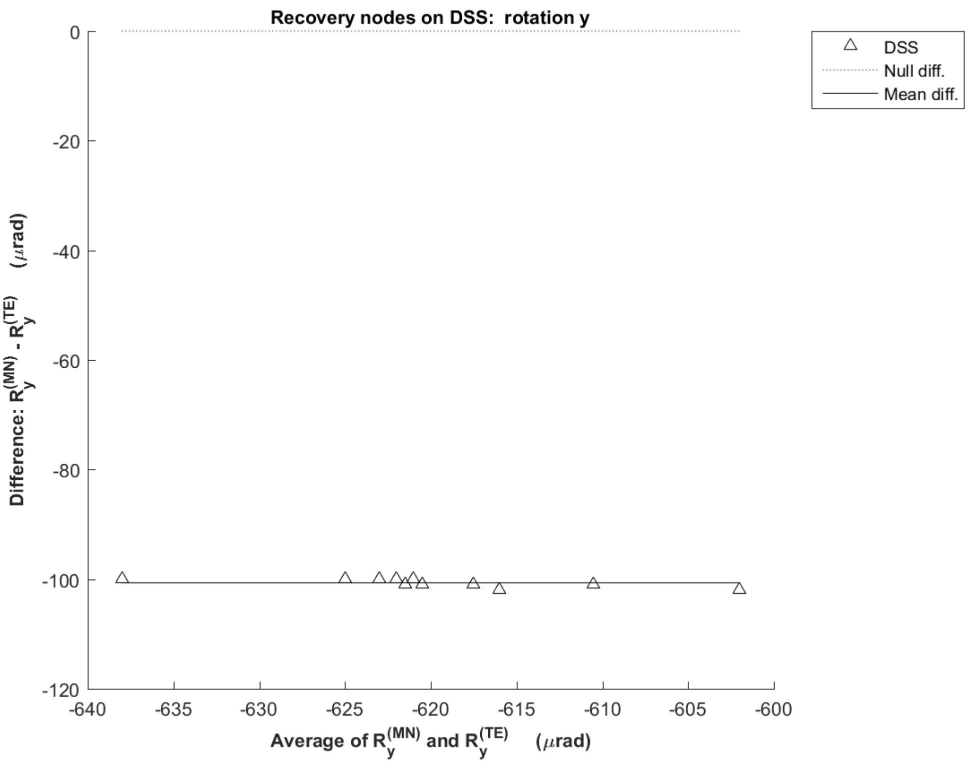

Figure D.26. Comparison between the manual method (superscript MN) and the TEMASE one (superscript TE) for R_y of the telescope.

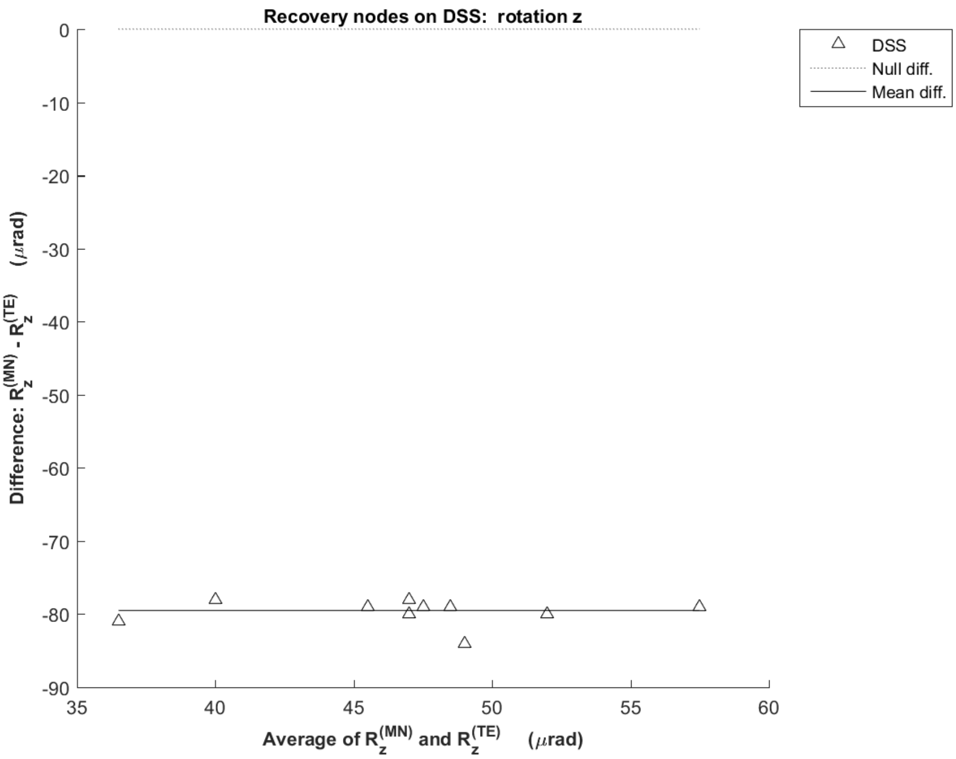

Figure D.27. Comparison between the manual method (superscript MN) and the TEMASE one (superscript TE) for R_z of the telescope.

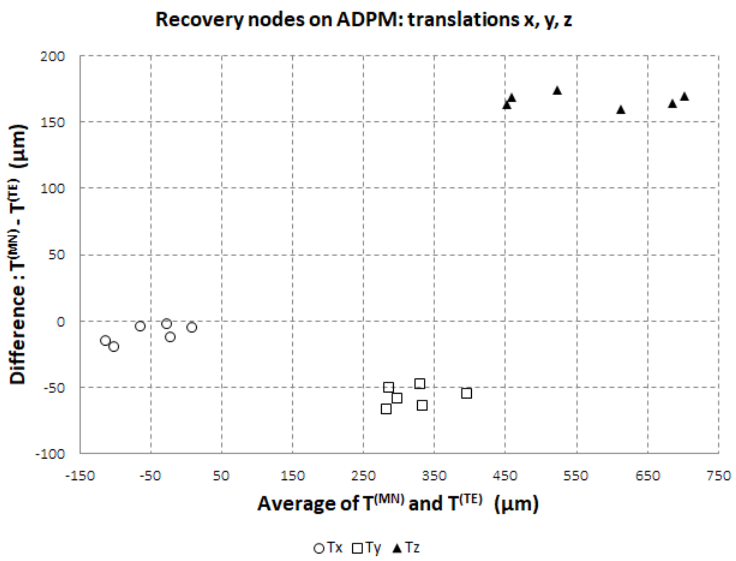

Figure D.28. Comparison between the manual method (superscript *MN*) and the TEMASE one (superscript *TE*) for ADPM support.

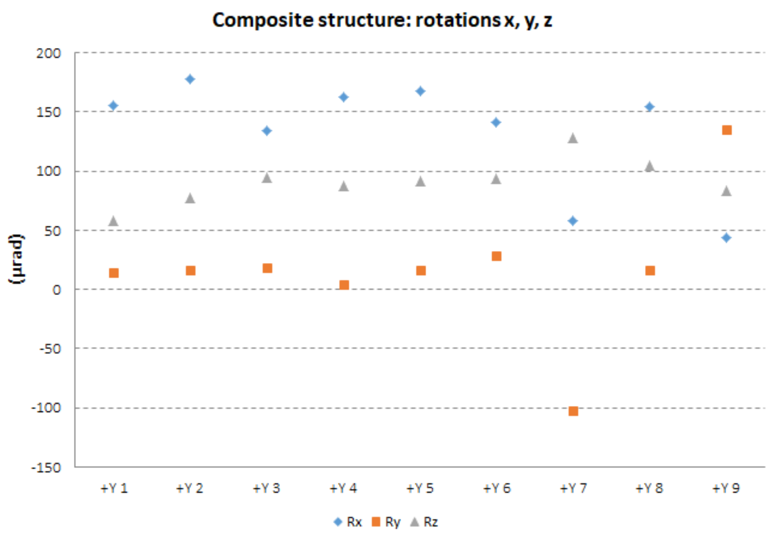

Figure D.29. Rotations on panel +y of the composite structure.

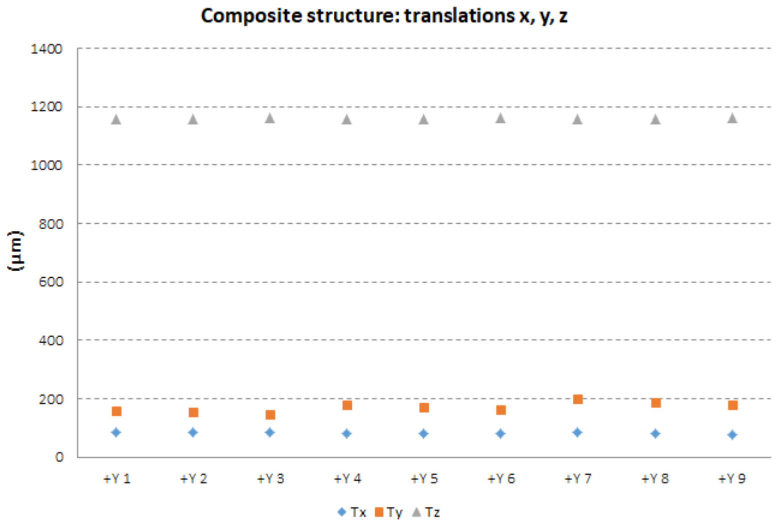

Figure D.30. Translations on panel +y of the composite structure.

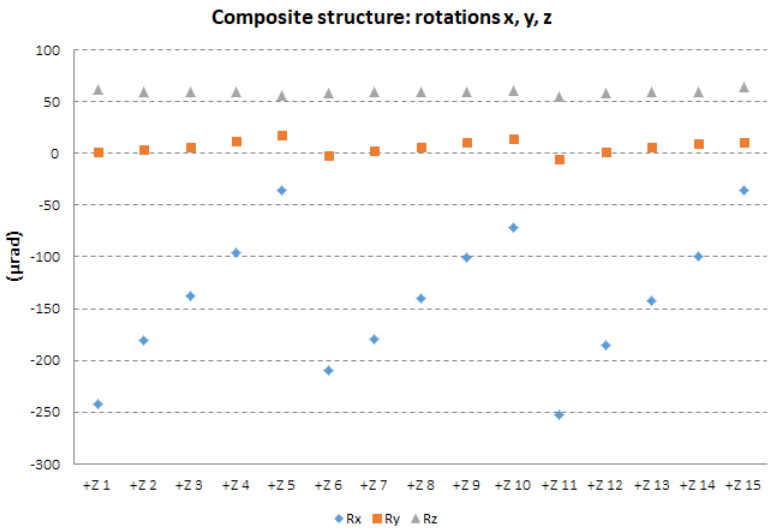

Figure D.31. Rotations on panel +z of the composite structure.

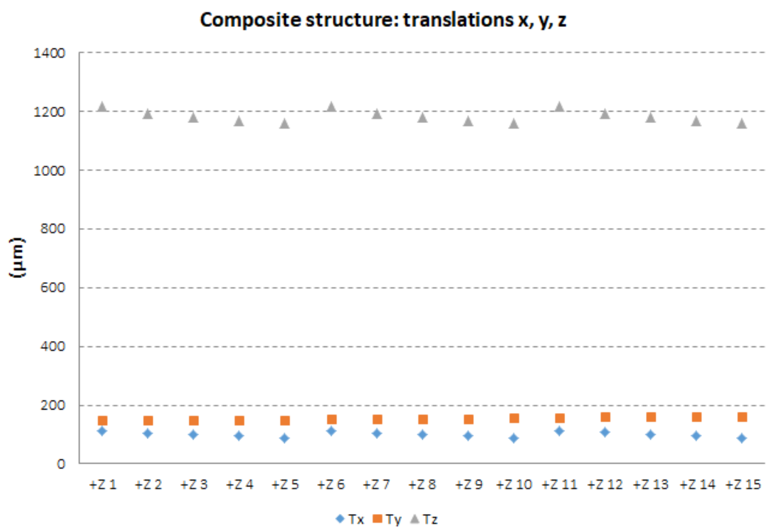

Figure D.32. Translations on panel +z of the composite structure.

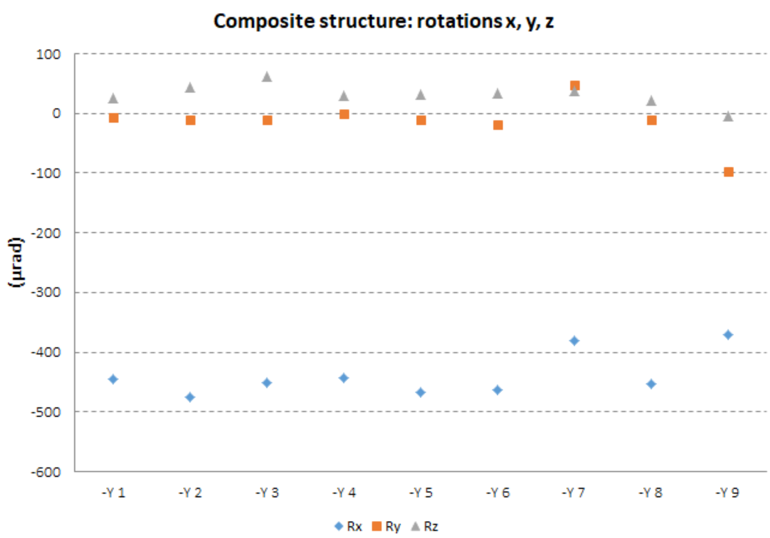

Figure D.33. Rotations on panel -y of the composite structure.

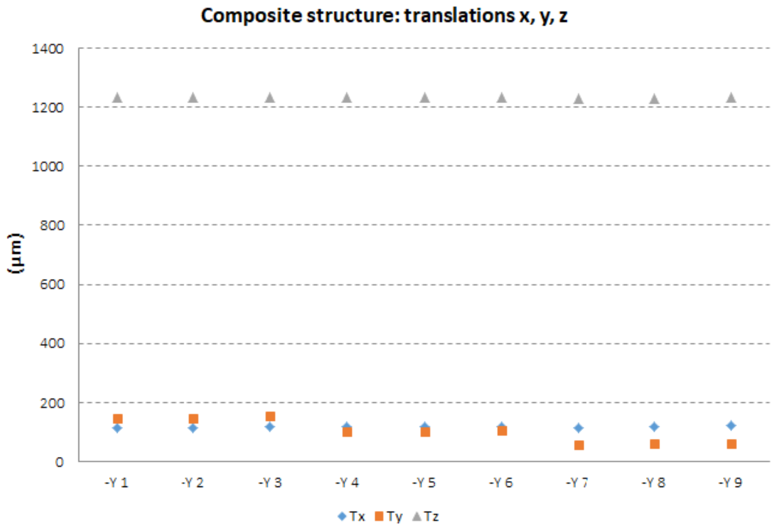

Figure D.34. Translations on panel -y of the composite structure.

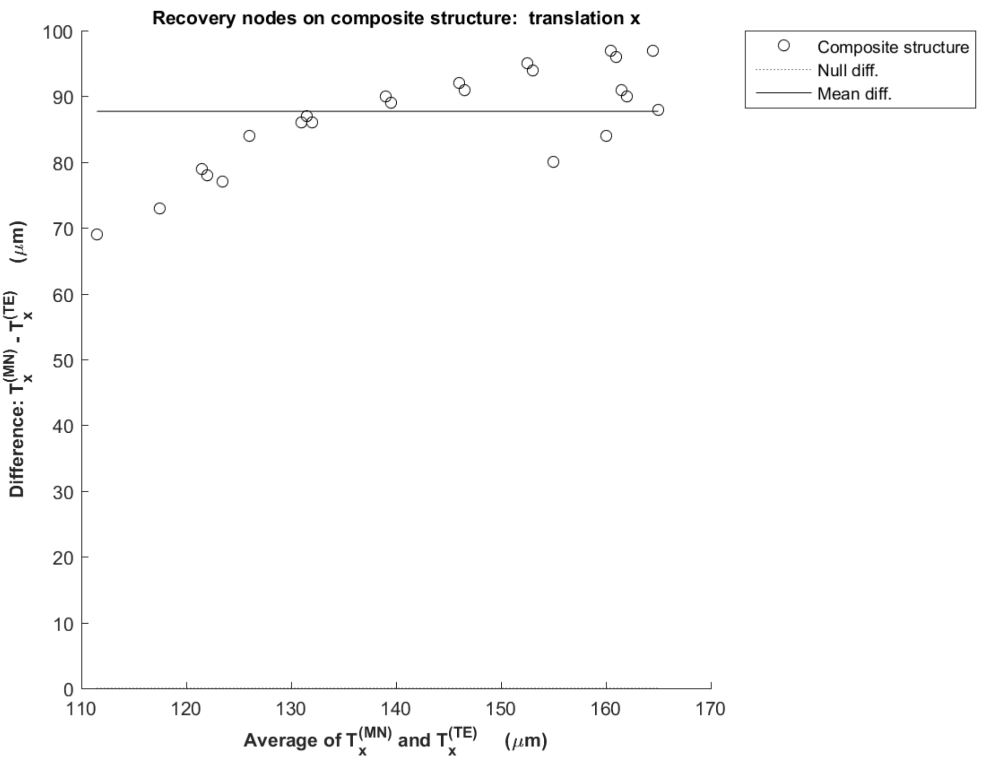

Figure D.35. Comparison between the manual method (superscript MN) and the TEMASE one (superscript TE) for T_x of the composite structure.

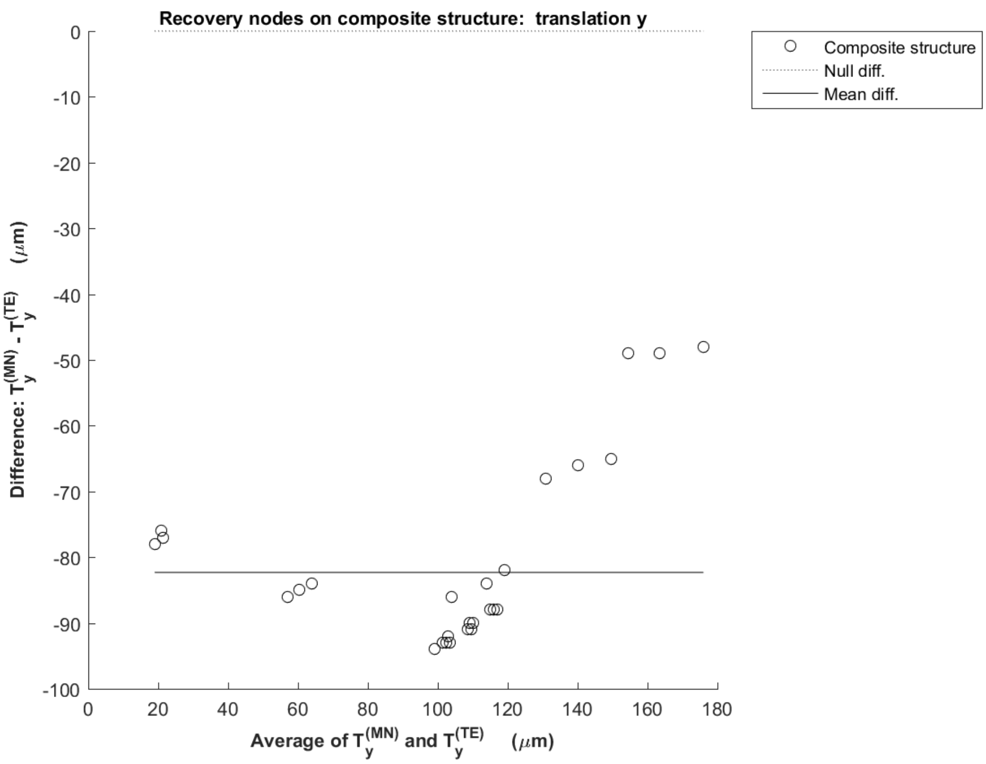

Figure D.36. Comparison between the manual method (superscript *MN*) and the TEMASE one (superscript *TE*) for T_y of the composite structure.

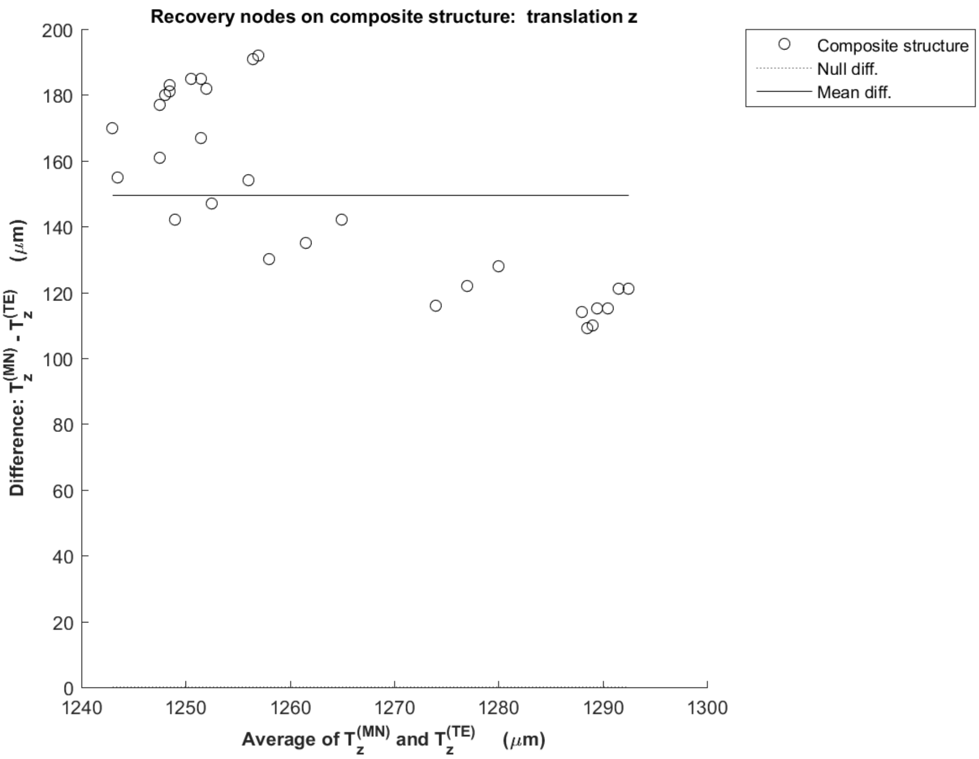

Figure D.37. Comparison between the manual method (superscript *MN*) and the TEMASE one (superscript *TE*) for T_z of the composite structure.

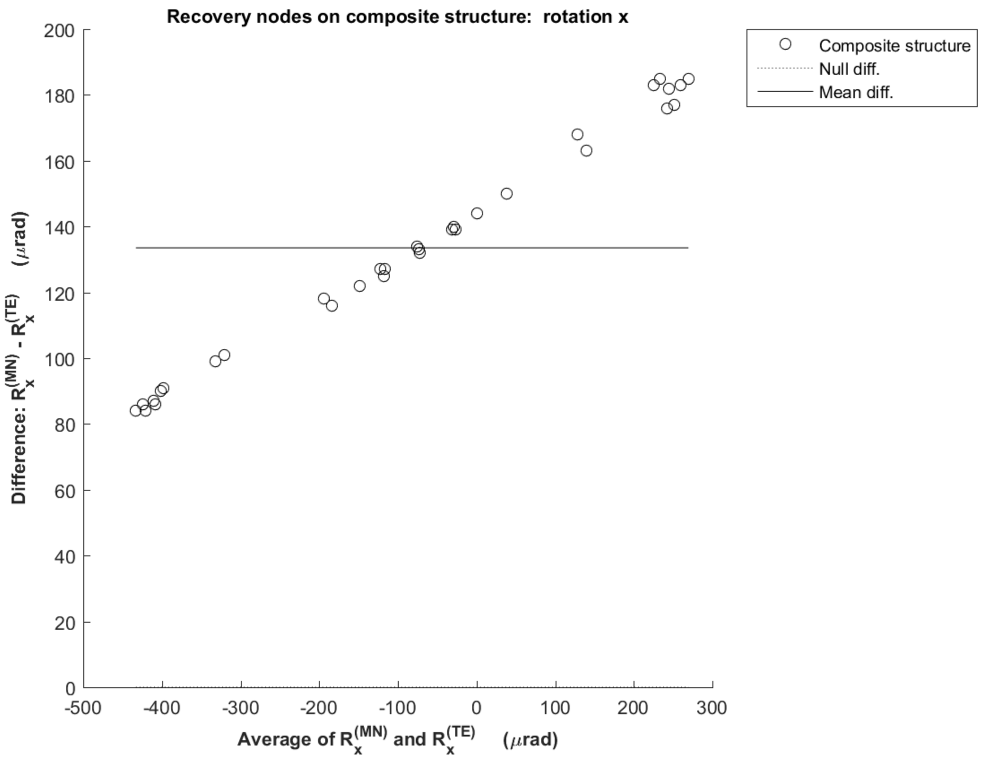

Figure D.38. Comparison between the manual method (superscript *MN*) and the TEMASE one (superscript *TE*) for R_x of the composite structure.

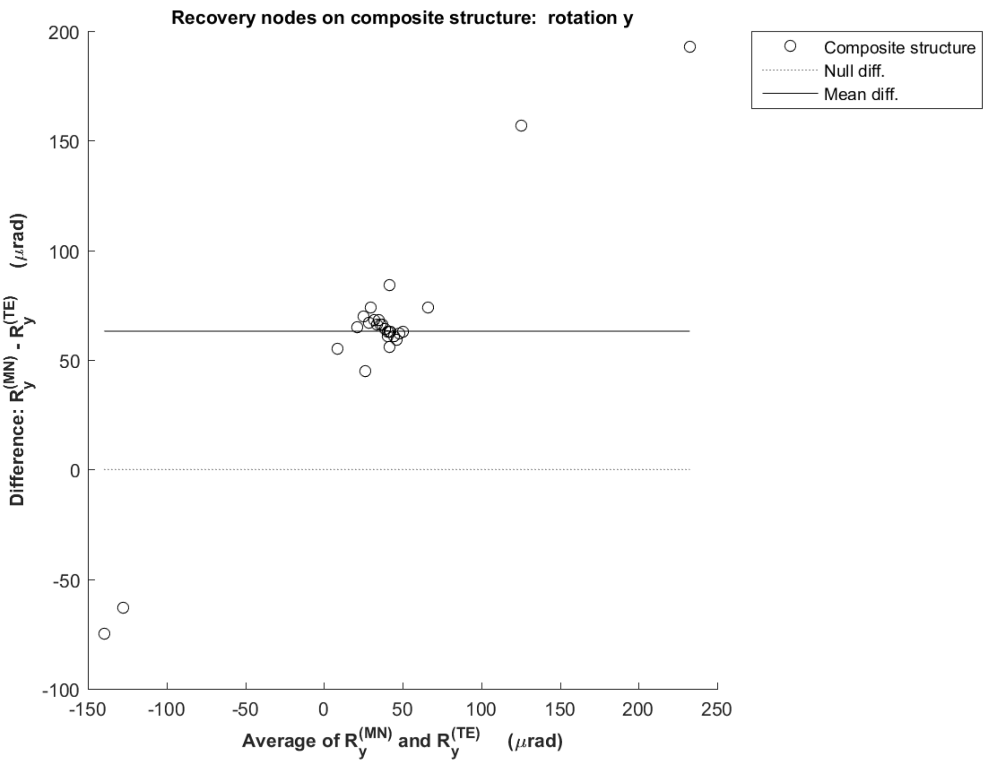

Figure D.39. Comparison between the manual method (superscript *MN*) and the TEMASE one (superscript *TE*) for R_y of the composite structure.

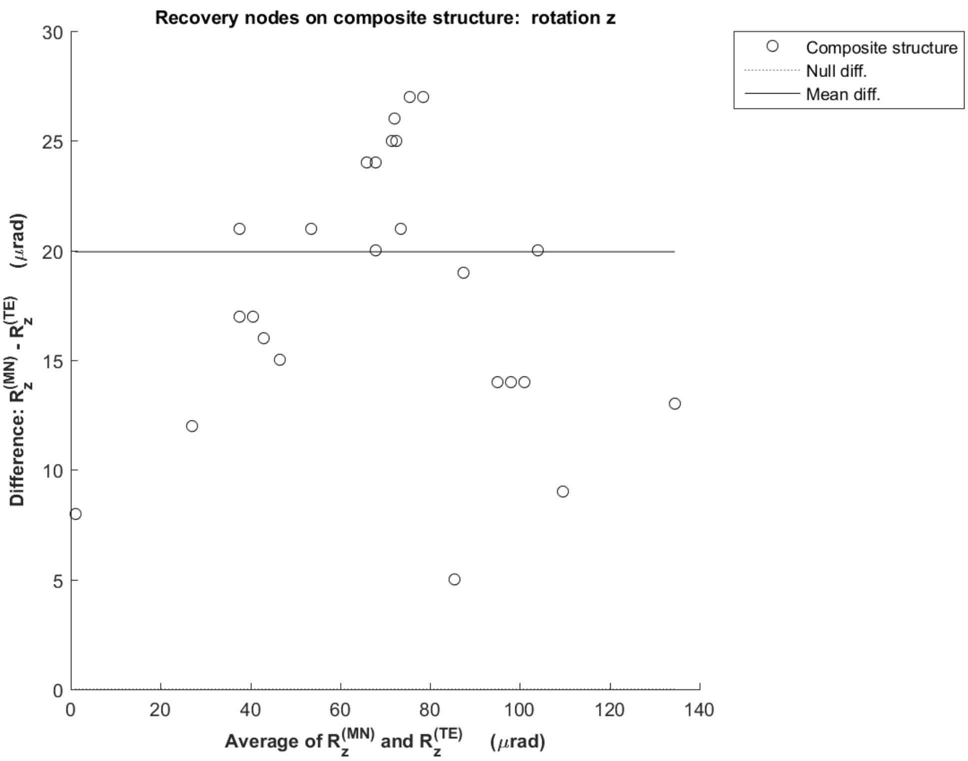

Figure D.40. Comparison between the manual method (superscript *MN*) and the TEMASE one (superscript *TE*) for R_z of the composite structure.